

Center for Gas Turbines and Power
The Pennsylvania State University
University Park, PA 16802

FINAL REPORT ON:

**METHODS OF DESENSITIZING TIP CLEARANCE
EFFECTS IN TURBINES**

J. Tallman, B. Lakshminarayana
October, 2000

Research Sponsored by:

ARMY RESEARCH OFFICE
(Grant No. DAAD 19-99-1-0335, Proposal No. 40297-EG-II, Technical Monitor: Dr. T. Doligalski, P.O. Box 1221; Research Triangle Park, NC 27709-2211)

DISTRIBUTION STATEMENT A

Approved for Public Release
Distribution Unlimited

20010116 092

REPORT DOCUMENTATION PAGE

Form Approved
OMB NO. 0704-0188

Public Reporting burden for this collection of information is estimated to average 1 hour per response, including the time for reviewing instructions, searching existing data sources, gathering and maintaining the data needed, and completing and reviewing the collection of information. Send comment regarding this burden estimates or any other aspect of this collection of information, including suggestions for reducing this burden, to Washington Headquarters Services, Directorate for Information Operations and Reports, 1215 Jefferson Davis Highway, Suite 1204, Arlington, VA 22202-4302, and to the Office of Management and Budget, Paperwork Reduction Project (0704-0188,) Washington, DC 20503.

1. AGENCY USE ONLY (Leave Blank)		2. REPORT DATE October, 2000	3. REPORT TYPE AND DATES COVERED Final Report: 1 Aug 99 - 31 Oct 2000
4. TITLE AND SUBTITLE Methods of Desensitizing Tip Clearance Effects in Turbines		5. FUNDING NUMBERS Grant: DAAD 19-99-1-0335	
6. AUTHOR(S) J. Tallman & B. Lakshminarayana		8. PERFORMING ORGANIZATION REPORT NUMBER PSU CGTP 2000-09	
7. PERFORMING ORGANIZATION NAME(S) AND ADDRESS(ES) Pennsylvania State University 230 Hammond Building University Park, PA 16802		10. SPONSORING / MONITORING AGENCY REPORT NUMBER ARO 40297.1-EG-11	
9. SPONSORING / MONITORING AGENCY NAME(S) AND ADDRESS(ES) U. S. Army Research Office P.O. Box 12211 Research Triangle Park, NC 27709-2211		11. SUPPLEMENTARY NOTES The views, opinions and/or findings contained in this report are those of the author(s) and should not be construed as an official Department of the Army position, policy or decision, unless so designated by other documentation.	
12 a. DISTRIBUTION / AVAILABILITY STATEMENT Approved for public release; distribution unlimited.		12 b. DISTRIBUTION CODE	
13. ABSTRACT (Maximum 200 words) <p>This study is an attempt to reduce the effect of the leakage vortex in axial flow turbines. A 3D Navier-Stokes CFD solver with two equation turbulence modeling was used to compute the flow through an axial flow turbine with modified blade tip designs. The three modified blade tip designs each involved adding a chamfer to the tip of the blade, in an attempt to diffuse the leakage flow through the gap and obstruct the leakage flow with the outer casing's shear layer. A baseline flat tip case and three modified tip cases were simulated and the leakage flow and vortex for each was analyzed in detail. By chamfering the blade tip near the trailing edge of the gap, the leakage flow inside the gap was turned toward the direction of the blade's camber. This turning resulted in a decrease in the size and strength of the leakage vortex and its subsequent losses, while at the same time, did not reduce the blade loading by an appreciable amount.</p>			
14. SUBJECT TERMS Turbines, Computational Fluid Dynamics		15. NUMBER OF PAGES 82	16. PRICE CODE
17. SECURITY CLASSIFICATION OR REPORT UNCLASSIFIED		18. SECURITY CLASSIFICATION ON THIS PAGE UNCLASSIFIED	19. SECURITY CLASSIFICATION OF ABSTRACT UNCLASSIFIED
20. LIMITATION OF ABSTRACT UL			

Standard Form 298 (Rev.2-89)

**Standard Form 190 (MIL-190)
Prescribed by ANSI Std. Z39-18**

298-102

ABSTRACT

This study is an attempt to reduce the effect of the leakage vortex in axial flow turbines. A 3D Navier-Stokes CFD solver with $k-\epsilon$ turbulence modeling was used to compute the flow through an axial flow turbine with modified blade tip designs. The three modified blade tip designs each involved adding a chamfer to the tip of the blade, in an attempt to diffuse the leakage flow through the gap and obstruct the leakage flow with the outer casing's shear layer. A baseline flat tip case and three modified tip cases were simulated and the leakage flow and vortex for each was analyzed in detail. By chamfering the blade tip near the trailing edge of the gap, the leakage flow inside the gap was turned toward the direction of the blade's camber. This turning resulted in a decrease in the size and strength of the leakage vortex and its subsequent losses, while at the same time, did not reduce the blade loading by an appreciable amount.

TABLE OF CONTENTS

ABSTRACT.....	ii
TABLE OF CONTENTS.....	iii
LIST OF FIGURES	v
LIST OF TABLES	viii
NOMENCLATURE	ix
ACKNOWLEDGMENTS	xiii
CHAPTER 1: INTRODUCTION	1
1.1: A Description of the Tip Leakage Flow and its Environment.....	1
1.1.1: Physical Explanation of the Tip Leakage Flow	1
1.1.2: Detriments to Performance	2
1.2: Background.....	4
1.2.1: Past Tip Desensitization Efforts.....	4
1.2.2: Current Understanding	6
1.3: Objectives and Direction of the Research	8
1.3.1: Blade Tip Designs Simulated.....	8
1.3.2: Reasons for Numerical Simulation	11
1.3.3: Choice of Blade Geometry.....	11
1.4: Report Overview	13
CHAPTER 2: NUMERICAL METHOD REVIEW AND VALIDATION	15
2.1: Governing Equations	15
2.1.1: Computational Domain Transform	17

2.1.2: Finite Difference Form.....	19
2.1.3: Pressure Correction Equation.....	23
2.1.4: Boundary Conditions	25
2.2: Grid.....	28
2.2.1: Coordinate System	30
2.3: Code Validation.....	31
CHAPTER 3: RESULTS.....	47
CHAPTER 4: SUMMARY AND CONCLUSIONS.....	83
BIBLIOGRAPHY	85

LIST OF FIGURES

Figure 1.1: Tip Leakage Flow and Vortex Illustration	2
Figure 1.2: Secondary Flows in an Axial Flow Turbine.....	7
Figure 1.3: Chamfered Blade Tip Illustration.....	10
Figure 1.4: Blade Profile and Velocities Used.....	13
Figure 2.1: Control Volume with Grid Notation	19
Figure 2.2(a): Grid (Every Other Gridline Shown)	30
Figure 2.2(b): Embedded Grid near the Leading and Trailing Edges.....	31
Figure 2.3: Pitch Angle near the Casing	35
Part (a): $X = 60\%$ Axial Chord.....	35
Part (b): $X = 80\%$ Axial Chord.....	37
Part (c): $X = 90\%$ Axial Chord.....	39
Figure 2.4: Span Angle near the Casing	41
Part (a): $X = 60\%$ Axial Chord.....	41
Part (b): $X = 80\%$ Axial Chord.....	43
Part (c): $X = 90\%$ Axial Chord.....	45
Part (a): Baseline Case.....	64
Part (b): Leading Edge Chamfer Case.....	64
Figure 3.1: Leakage Vortices for Various Tip Geometry	64
Part (c): Full Chamfer Case	65
Part (d): Trailing Edge Chamfer Case	65
Figure 3.1 (continued): Leakage Vortices for Various Tip Geometry.....	65

Part (a): Baseline Case.....	66
Part (b): Trailing Edge Chamfer Case	66
Figure 3.2: Leakage Flow and Vortex Comparison.....	66
Part (a): Baseline Case.....	67
Part (b): Trailing Edge Chamfer Case	67
Figure 3.3: Velocity and Pressure in the Blade-to-Blade Plane at 1.002% Span	67
Part (a): Baseline Case.....	68
Part (b): Trailing Edge Chamfer Case	68
Figure 3.4: Velocity and Pressure in the Blade-to-Blade Plane at 96% Span	68
Figure 3.5: Non-Dimensional Streamwise Vorticity Contours at 60% Axial Chord	69
Figure 3.6: Non-Dimensional Streamwise Vorticity Contours at 70% Axial Chord	70
Figure 3.7: Non-Dimensional Streamwise Vorticity Contours at 80% Axial Chord	71
Figure 3.8: Non-Dimensional Streamwise Vorticity Contours at 90% Axial Chord	72
Figure 3.9: Streamwise Vorticity Inside the Leakage Vortex at 90% Axial Chord	73
Figure 3.10: Non-Dimensional Streamwise Vorticity Contours at 110% Axial Chord ...	74
Figure 3.11: Streamwise Vorticity Inside the Leakage Vortex at 110% Axial Chord	75
Figure 3.12: Total Pressure / Inlet Total Pressure at 90% Axial Chord	76
Figure 3.13: Total Pressure Inside the Leakage Vortex at 90% Axial Chord.....	77
Figure 3.14: Total Pressure / Inlet Total Pressure at 110% Axial Chord	78
Figure 3.15: Total Pressure Inside the Leakage Vortex at 110% Axial Chord.....	79
Figure 3.16: Passage-Average Loss Coefficient vs. Axial Location	80
Figure 3.17: Static Pressure Coefficient (Cp) on the Blade.....	81

Figure 3.18: Static Pressure Coefficient (C_p) at the Blade Tip and Midspan..... 82

LIST OF TABLES

Table 1.1: Turbine Case Information.....	12
Table 3.1: Blade Loading Force Values	63

NOMENCLATURE

a	Coefficient of differenced momentum or pressure equation
C_p	Coefficient of pressure, $(p_{in} - p) / Q_{in}$
$C_\mu, C_1, C_2, C_3, C_4$	Empirical constants of two-equation turbulence model
E	Coefficient in pressure equation
E_2	Coefficient in pressure equation
f_2, f_ϵ, f_μ	Functions in two-equation turbulence model
G_1	Contravariant velocity in x-direction, $\xi_x u_1 + \xi_y u_2 + \xi_z u_3$
G_2	Contravariant velocity in y-direction, $\eta_x u_1 + \eta_y u_2 + \eta_z u_3$
G_3	Contravariant velocity in z-direction, $\zeta_x u_1 + \zeta_y u_2 + \zeta_z u_3$
J	Jacobian of the coordinate transformation, $x_\xi(y_\eta z_\zeta - y_\zeta z_\eta) + x_\eta(y_\zeta z_\xi - y_\xi z_\zeta) + x_\zeta(y_\xi z_\eta - y_\eta z_\xi)$
k	Turbulent kinetic energy
n	Principle normal direction
p	Static pressure
P_0	Total pressure
Q_{in}	Inlet dynamic pressure
r	Radius
Re	Reynolds Number
S	Source Term
t	Time

T_μ	Turbulence intensity
u, v, w	Mean velocity
u_i	Mean velocity in tensor notation
u', v', w'	Fluctuation velocity
u^*	Friction velocity, $\sqrt{\frac{\text{wall shear stress}}{\rho}}$
$\overline{u'_i u'_j}$	Reynolds stress
V	Total velocity
v_s	Secondary velocity in the blade-to-blade plane
x, y, z	Cartesian coordinates (defined for a cascade in figure 1.2: x, y, z correspond to axial, tangential, and spanwise directions, respectively)
y^+	Non-dimensional turbulence wall function, $\frac{\rho u^* y_w}{\mu}$
y_w	Normal distance from a solid wall
α	Geometrical transformation variable, $\nabla \zeta \bullet \nabla \zeta$
β	Geometrical transformation variable, $\nabla \eta \bullet \nabla \eta$
$\frac{\partial}{\partial ?}$	Partial derivative
δ_{ij}	Delta tensor ($\delta=1$ if $i=j$, else 0)
γ	Geometrical transformation variable, $\nabla \zeta \bullet \nabla \zeta$
Γ	General diffusion coefficient
ϵ	Turbulence dissipation rate
ϵ_2	Coefficient of 2 nd order artificial dissipation for convection- Diffusion equations

ϵ_4	Coefficient of 4 th order artificial dissipation for convection-diffusion equations
ϵ_{pw}	Coefficient of 4 th order artificial dissipation for pressure
λ	Loss coefficient, $(P_{0in} - P_0) / Q_{in}$
ϕ_1	Geometrical transformation variable, $\nabla \xi \bullet \nabla \eta$
ϕ_2	Geometrical transformation variable, $\nabla \xi \bullet \nabla \zeta$
ϕ_3	Geometrical transformation variable, $\nabla \eta \bullet \nabla \zeta$
μ	Molecular viscosity
μ_t	Turbulent eddy viscosity
ν	Kinematic viscosity
ξ, η, ζ	Generalized coordinates (shown in figure 2.1)
ρ	Density
σ_c	Empirical constant of two-equation turbulence model
τ	Tip clearance height
ϕ	General scalar dependent variable
Ω	Angular velocity
ω	Relaxation parameter

Subscripts

B	The $i, j, k-1$ grid point
b	The $i, j, k-1/2$ control volume face
E	The $i+1, j, k$ grid point

e	The $i+1/2, j, k$ control volume face
in	Inlet Quantity
N	The $i, j+1, k$ grid point
n	The $i, j+1/2, k$ control volume face
P	The i, j, k grid point
r	Radial direction
S	The $i, j-1, k$ grid point
s	The $i, j-1/2, k$ control volume face
T	The $i, j, k+1$ grid point
t	The $i, j, k+1/2$ control volume face
W	The $i-1, j, k$ grid point
w	The $i-1/2, j, k$ control volume face
θ	Tangential direction
i	Free index in tensor notation (i=1 for x, i=2 for y, i=3 for z)
j	Dummy index in tensor notation (denotes summation over $j=1, 2, \text{ and } 3$)

Superscripts

—	Ensemble Average
/	Correction, Fluctuating
*	Estimate (also used in u^* = friction velocity)
ϕ	General scalar dependent variable referred to

ACKNOWLEDGMENTS

The research presented in this report was carried out under sponsorship of Army Research Office Grant DAAD 19-99-1-0335, with Dr. T. Doligalski as the grant monitor. This work is continuing under AGTSR program AGTSR 99-01-SR079.

CHAPTER 1: INTRODUCTION

The tip leakage flow is one of the most prevalent and influential features of the flow through turbomachine rotors. Along with its resulting vortex, the leakage flow acts as a source of both unsteadiness and aero thermal loss, and is therefore detrimental to turbomachine performance. Furthermore, the leakage flow is a phenomenon that is difficult to either predict or measure in most turbomachines. The research presented in this report is a computational attempt to reduce the leakage flow and vortex in axial flow turbines through blade tip modification.

1.1: A Description of the Tip Leakage Flow and its Environment

1.1.1: Physical Explanation of the Tip Leakage Flow

The tip leakage vortex is a direct result of the loading on the blade, and can be described two different ways:

Description 1: At the blade tip, there is an open path for fluid to flow from the pressure surface to the suction surface, as well as a pressure gradient to drive the flow. This is known as the tip leakage flow, and is illustrated in figure 1.1. The leakage jet interacts with the main passage flow and rolls up into a tip leakage vortex. The intense mixing of the two streams (leakage flow and main passage flow) causes major viscous losses.

Description 2: As with any cambered airfoil, the velocity difference between the pressure and suction surfaces results in a bounded circulation around the blade, which, according to Kelvin, cannot simply end along with the blade at its tip. At the blade tip, the circulation continues into a vortex, which is bent and dragged behind the moving blade.

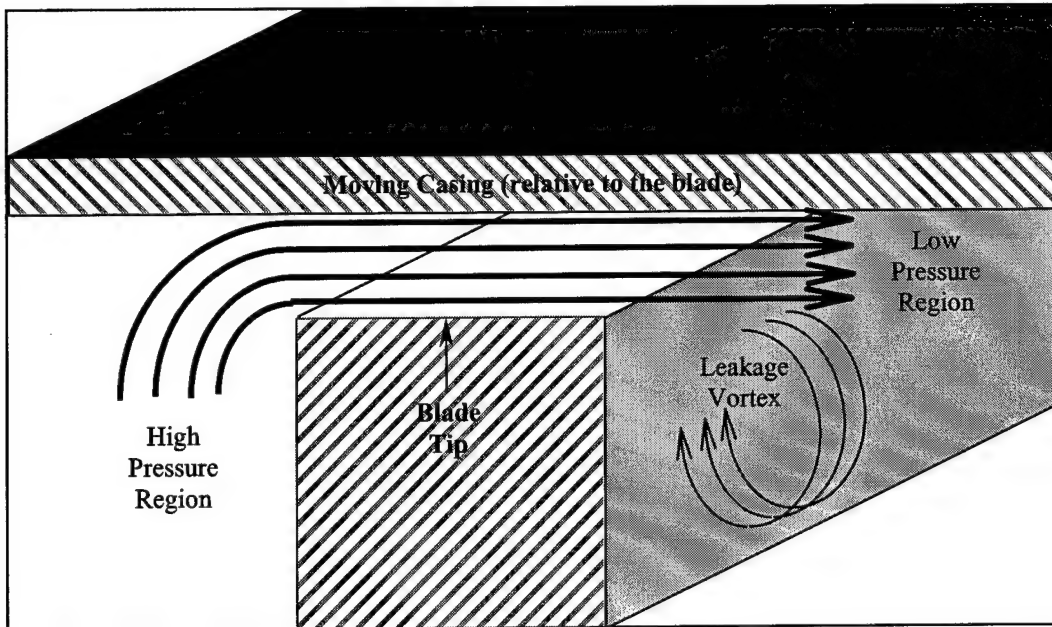


Figure 1.1: Tip Leakage Flow and Vortex Illustration

1.1.2: Detriments to Performance

Tip leakage flows and their resulting vortices are detrimental to turbomachinery performance for multiple reasons:

- 1) *Decay*: The vortex will ultimately decay away, primarily by turbulent dissipation. The energy of the vortex is converted into internal energy and cannot be recovered.
- 2) *Undeturning*: Flow turning is the primary means of transferring mechanical energy in turbomachines. The fluid that is forced over the tip of the blade is not turned to the extent of the machine's design. The result is less blade loading near the tip.
- 3) *Blockage*: The tip leakage vortex acts as an obstruction to the main flow through the blade passage. Therefore, less mass can flow through the machine and less work is done.

For transonic flows through multiple blade rows, this blockage can lead to changes in the inlet flow angle of the blade, as is described by Dietrichs, et al. [1].

4) *Entrainment*: The slower moving leakage vortex and its low pressure core acts to entrain the faster passage flow, thus causing substantial three-dimensionality and deviations from design conditions.

5) *Downstream Unsteadiness*: In any turbomachinery with multiple stages, a certain degree of unsteadiness is always present within the flow. Physical features of a steady flow through a blade row, such as wakes, vortices, and boundary layers, are seen as oscillations in the relative flow by the row immediately downstream. This is due to the relative motion between all adjacent blade rows. The resulting fluctuation in the pressure and velocity fields result in two major performance detriments that are of design concern. First, the unsteady flow field means that blade loading will not be steady, but rather oscillating slightly at the upstream row's passing frequency. Although the magnitude of this fluctuation is small, it is still of concern from a fatigue standpoint. It is most often desirable to design turbomachines as lightweight as possible, yet still able to endure these fatiguing stresses. This is particularly true in military aircraft applications, which tend to call for operation at high loading over long periods of time.

Second, oscillating pressure due to upstream relative motion is the largest cause of noise within turbomachinery. This is particularly true in compressors. Here, the relative motion between the rotor and the casing enhances tip vortices. Also, compressor boundary layers and, thus, wakes, tend to be larger because of the adverse pressure gradients. Both of these effects result in larger pressure oscillations and more noise.

Noise is often of concern to designers as a comfort issue, as well as in situations where public health codes require limits on noise emissions.

6) *Complex Heat Transfer*: For turbomachines that operate at high temperatures, such as aircraft engine turbines, the tip leakage flow increases the complexity of the heat transfer to the blade and outer casing. Although heat transfer aspects are beyond the scope of this study, they are shown here to be a great challenge that high temperature turbine designers must overcome. In such a turbine, the tip leakage vortex rolls up along the suction surface of the blade near to the tip. This acts to entrain hot, freestream fluid in toward the suction surface of the blade. Also, the tip leakage flow will expose the top surface of the blade to high temperatures. Finally the impingement of the leakage vortex acts to break up film cooling flows and bring freestream gas in contact with blade surfaces. This is true for both the blade row responsible for the vortex and the downstream row, where the relative unsteadiness of the situation only enhances the complexity of the mixing.

1.2: Background

The term “Tip Desensitization” has been defined by industry and academia to represent efforts aimed at reducing or eliminating the leakage flow and vortex in axial flow turbines. This section gives an overview of past tip desensitization efforts and explains the current understanding of the physics of the flow field inside the turbine rotor.

1.2.1: Past Tip Desensitization Efforts

Although there have been a number of past studies dealing with tip desensitization, the final results presented tend to be inconclusive. A few suggested

concepts in this area re the tip winglets, tip aerodynamic modification (blade profile change) for reducing leakage, non-uniform tip-gap (adverse pressure gradient) to diffuse the leakage flow structure, normal/angled injection into squealer tip regions, and increased turbulence intensity upstream of the rotor for weakening the tip vortex.

Some of the earlier efforts to reduce the tip clearance effects are summarized below. It should be state here that none of these devices have been tested in the hostile environment of a rotor or with relative motion between the blade and the wall.

1. Some of the early attempts to reduce the tip leakage flow through slots in the blade tip and flow fence were unsuccessful (Lakshminarayana and Horlock, [2]).
2. The pressure side winglet provided improved performance in the simulated flow in a channel (Wadia and Booth, [3]). This contradict the recent investigations in a cascade by Yaras and Sjolander [4], who concluded that the pressure side winglet was least effective and the double sided winglet was most effective.
3. Radiusing and contouring the leakage gap geometry prevented the formation of a separation bubble and decreased the losses (Bindon and Morphis, [5]), but the resulting thin tip section may not be suitable for a high temperature application.
4. The numerical simulation by Chen et al. [6] indicates that the two-squealer tip combined with the jet injection at the correct angle to the leakage flow reduces the losses. They also indicate that the losses are very sensitive to the geometry and location of blowing.

5. Axially non-uniform tip clearance in a compressor improved the losses (Mohan and Guruprasad, [7]). It is not known whether this concept is valid for turbine flow.
6. A recent investigation by Staubach et al. [8] indicates that desensitization can be achieved through proper design of the upstream stator and regulation of the spanwise flow distribution in the rotor blade.
7. A very thorough overview of tip leakage research in turbines, both experimental and computational, can be found in the lecture series by Sjolander [9].

1.2.2: Current Understanding

A comprehensive numerical study by Tallman and Lakshminarayana [10,11] revealed new insight into the physics of the leakage flow, leakage vortex, and additional secondary flows present in these turbines. Some of the major conclusions reached from this study are outlined below, and labeled in Fig. 1.2.

1. For tip clearance heights representative of a real turbine, the leakage vortex (Fig. 1.2 Lab. i) is not caused by a leakage jet shearing across the passage flow, as was previously believed.
2. Most of the leakage flow through the gap region does not roll into the leakage vortex (Fig. 1.2 Lab. ii). Only the fluid that passes through the gap very near to the blade tip ends up with the leakage vortex (Fig. 1.2 Lab. iii). The rest of the leakage flow joins with the passage flow, but still contributes to additional secondary flow effects inside the passage (Fig. 1.2 Lab. iv).

3. Vorticity convection by the leakage flow from the gap and into the passage plays an important roll in the physics of the secondary flow field. Fluid passing through the gap near the blade tip exits the gap with rotation in a direction closely corresponding to the rotation in the leakage vortex.

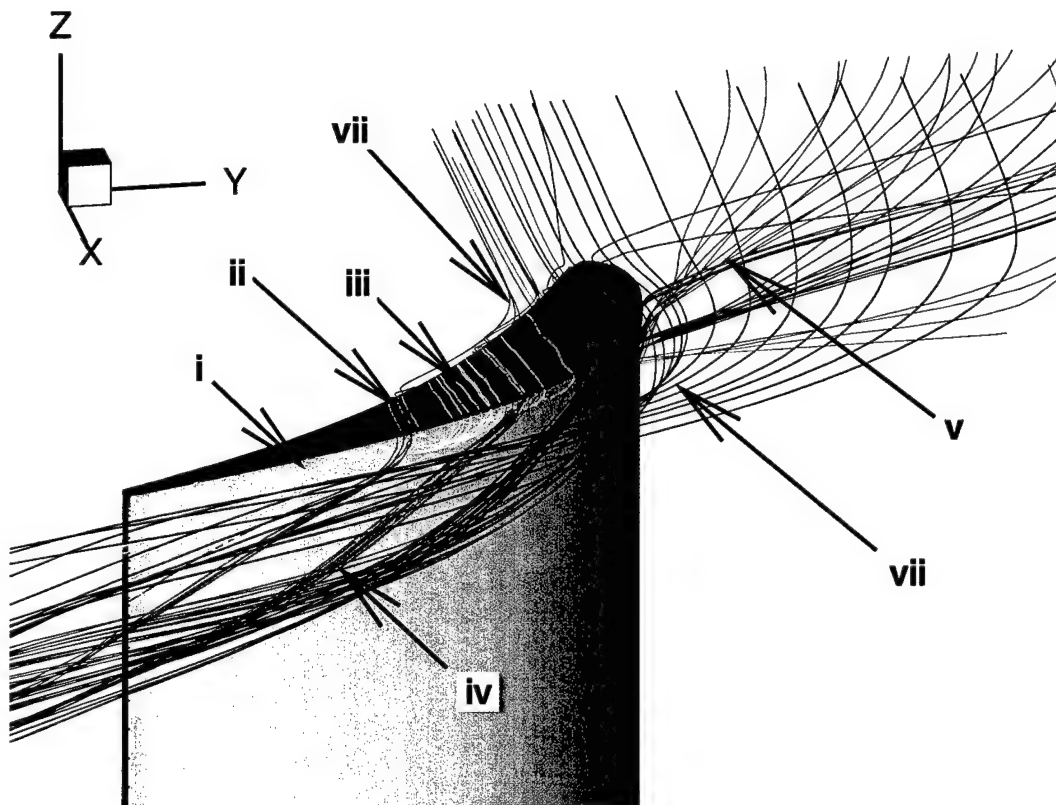


Figure 1.2: Secondary Flows in an Axial Flow Turbine

4. A strong secondary flow toward the suction side of the passage is present near the outer casing in the turbine (Fig. 1.2 Lab. v). This secondary flow resembles a passage vortex near the casing, but is primarily caused by the relative motion of the outer casing with respect to the blade. This secondary flow acts to obstruct

the leakage flow through the gap, particularly near the leading edge of the gap, and acts to reduce the leakage flow and vortex. This secondary flow was given the name “Near-Casing Secondary Flow” by Tallman and Lakshminarayana [10,11], and is also adapted here.

5. Two additional secondary flows were also defined by Tallman and Lakshminarayana [10,11]. The “Blockage Secondary Flow” results as the passage flow is obstructed around the leakage vortex and the near-casing secondary flow (Fig. 1.2 Lab. vi). The “Gap Entrainment Secondary Flow” is caused by the entrainment of the leakage fluid into the gap along the pressure surface side (Fig. 1.2 Lab. vii).

1.3: Objectives and Direction of the Research

The current research being presented here is a continuation of the original Tallman and Lakshminarayana study [10,11]. The objective of the current research is to study the effect of modified blade tip designs on the leakage vortex for axial flow turbines. Computational Fluid Dynamics, or CFD, is used as the tool for study and analysis of the flow field. Ultimately, these modified blade tip designs are aimed at reducing the leakage vortex and its negative effects.

1.3.1: Blade Tip Designs Simulated

Through some creative grid stretching in the spanwise direction, various degrees of tip chamfering were added to the turbine blade geometry simulated in the original study. For clarity, a chamfered blade tip is illustrated in Fig. 1.3. These chamfered blade

tip designs take advantage of the flow physics insight gained in the original Tallman and Lakshminarayana study [10,11], and are aimed at reducing the magnitude of the leakage vortex. Three cases are simulated for comparison with a regular, horizontal tip baseline case. The baseline case is taken from Tallman and Lakshminarayana [11]. The three modified cases and their design reasoning are outlined below.

1. Leading Edge Chamfer: The near-casing secondary flow is seen in Fig. 1.2 to act as an obstruction to the leakage flow. By increasing the gap height on the suction side near the leading edge, the near-casing secondary flow may enter the gap region and further inhibit the leakage flow.
2. Trailing Edge Chamfer: By increasing the gap height on the suction side from the mid-chord to trailing edge of the blade, the increasing flow area in the gap may act as a diffuser. This could reduce the leakage flow's velocity and, thus, its influence on the leakage vortex and secondary flow field outside the gap.
3. Full Chamfer: Both of the first two cases applied together.

In each of the three cases, the tip clearance height along the pressure side of the blade is held at a uniform 1.0% of the blade span (1.86 mm). Therefore, the minimum tip clearance is the same for all of the cases. Also for each of the three cases, the entire blade tip thickness is not chamfered. On the pressure side of the gap region, the tip remains horizontal for approximately 10% of the distance across the gap. This short

horizontal inlet region is illustrated in Fig. 1.3. It is included to avoid sharp corners on the blade tip, which could cause flow separation and would be difficult to cool.

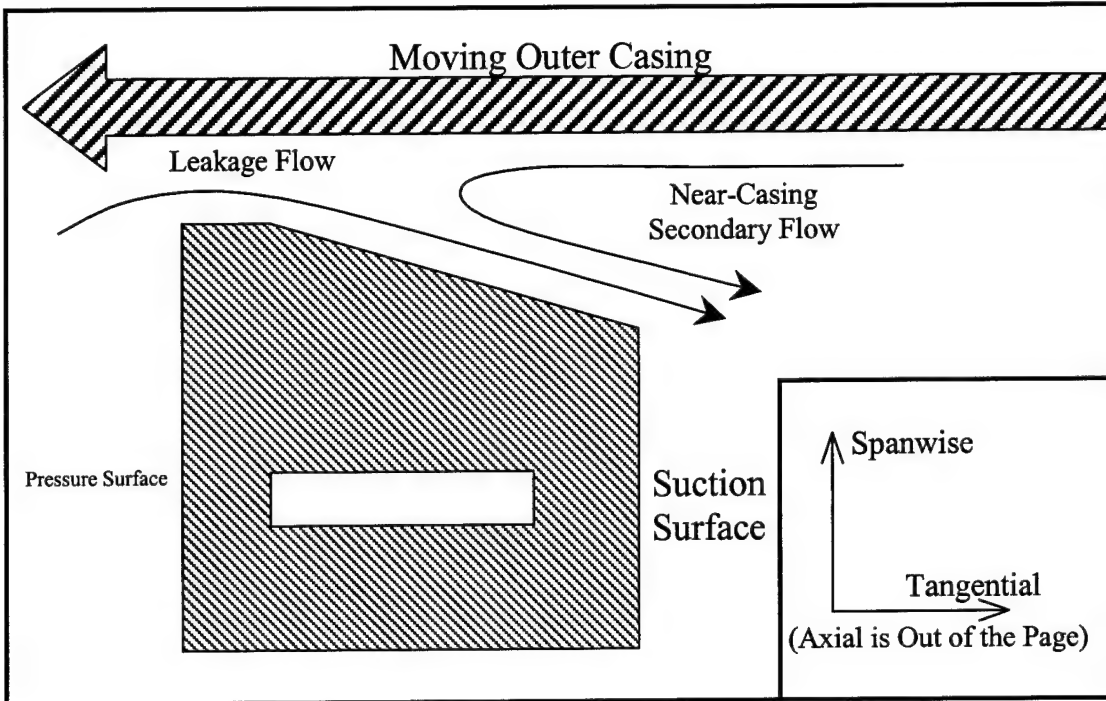


Figure 1.3: Chamfered Blade Tip Illustration

For all three cases, the angle of the chamfer angle is 7.7 degrees from horizontal. This angle corresponds to a suction side clearance height of 4% blade span (7.44 mm) at the blade's thickest location. Note that the clearance height will vary along the suction surface due to the blade's varying thickness, but remains constant (1.86 mm) along the blade's pressure surface. In each of the three cases, the chamfering angle is zero degrees at the inlet and exit of the computational domain. Near the leading edge of the blade, the chamfer angle is linearly increased from zero to 7.7 degrees. Near the trailing edge of the blade, the chamfer angle is linearly decreased back from 7.7 to zero degrees. For the full

chamfer case, the chamfer increase takes place upstream of the blade leading edge and the chamfer decrease takes place downstream of the blade trailing edge. For the leading edge chamfer case, the chamfer increase takes place upstream of the blade leading edge and the chamfer decrease takes place on the blade between 47.4% and 63.4% axial chord. For the trailing edge chamfer case, the chamfer increase takes place between 38.1% and 70.3% axial chord and the chamfer decrease takes place downstream of the blade trailing edge. The three chamfered tips are illustrated in chapter 3 (Fig. 3.1).

1.3.2: Reasons for Numerical Simulation

Computational Fluid Dynamics (CFD) was chosen as the means of investigation for this study. CFD is logically better suited to the study of the fine details of the tip leakage flow and vortex than experimental measurement. Even with present advanced measurement techniques, such as laser Doppler velocimetry, measuring the flow inside the tip clearance gap remains an impossibility. CFD offers a tool for looking at the flow inside areas too small for measurement. Also, CFD is considerably less expensive for testing multiple prototype blades than manufacturing test blades for experiment. The numerical procedure that was used in this study is outlined and validated in chapter 2, and has been previously validated by Basson and Lakshminarayana [13].

1.3.3: Choice of Blade Geometry

A linear turbine cascade blade originally studied by Bindon [5,12] was chosen as the geometry to be used in this study. This blade is shown in Fig. 1.4, and an overview of its geometry is given in Table 1.1. This is the same turbine cascade that was used in the

original Tallman and Lakshminarayana study [10,11]. The cascade's profile does not change in the spanwise direction, isolating the leakage flow and vortex from the effects of sweep, lean, or any other complicated geometrical parameters.

Two modifications have been made to the linear turbine cascade of Bindon [5,12]. First, the tip clearance height is reduced from 2.5% to 1.0% of the blade span. Second, unlike a cascade, the effect of casing relative motion is included in the current simulations, using a wall velocity of 31.0 m/s toward the suction side of the passage. This wall velocity corresponds to a flow coefficient value of 0.45, where the flow coefficient is defined as the inlet axial velocity divided by the moving blade's velocity. These values of tip clearance height and flow coefficient are more typical of a low-pressure turbine.

Table 1.1: Turbine Case Information

Chord Length = Span Length	0.186 m
Pitch Length	0.1323 m
Inlet Camber Angle	0.0°
Exit Camber Angle	68.0°
Tip Gap Height	1.0% Chord
Inlet Flow Velocity	13.82 m/s
Inlet Boundary Layer Thickness	10% Span
Inlet Turbulence Intensity	Approx. 2% Inlet Velocity
Outer Casing Relative Velocity	-31.0 m/s tangential
Working Fluid	Air

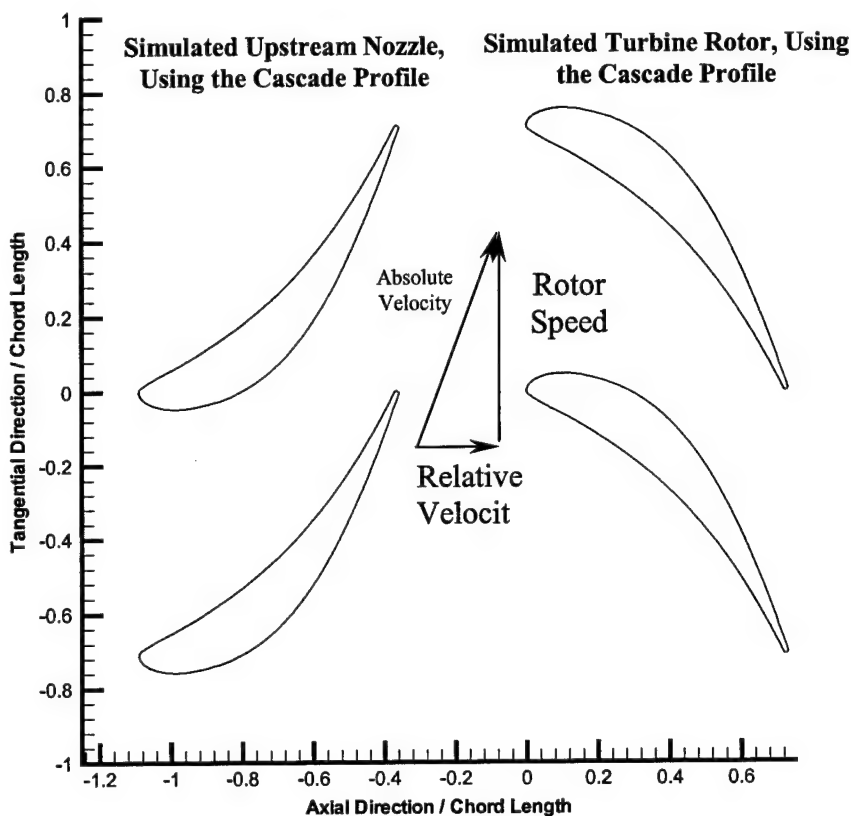


Figure 1.4: Blade Profile and Velocities Used

1.4: Report Overview

Chapter 1 of this report has introduced the leakage vortex concept, its ill effects, our current understanding of the leakage vortex, and the current research program. Chapter 2 presents the numerical method that is used for the four different simulations in this report. In addition, some code validation results from a separate turbine cascade simulation are presented in chapter 2, which show that the numerical method is capable of predicting complicated turbine secondary flows. Chapter 3 presents the simulation results for the three modified blade tips discussed in section 1.3. For each of the three

cases, results are compared directly with those from the baseline, horizontal blade tip case. Chapter 4 presents the conclusions found in this research, as well as ideas for future studies that build on the current research.

Some common terms that are used throughout the report are defined here for clarity. The axial (x), tangential (y), and spanwise (z) directions are referred to throughout this report according to their common definitions. These directions are illustrated in Fig. 1.3. The term “2D Streamwise” is used to refer to the direction of the 2D, inviscid, potential flow through the passage. The term “Camber Direction” is used to refer to the local direction of the blade’s camber line. The term “Secondary Flow” is used generically to represent any flow deviation from the 2D streamwise direction, and should not be confused with the term “Passage Vortex”.

CHAPTER 2: NUMERICAL METHOD REVIEW AND VALIDATION

The full Reynolds averaged Navier-Stokes equations are employed in this research to model the flow through a turbine cascade. The computer code used in this study uses a pressure-correction method for solving conservation equations for mass, momentum, and turbulence quantities. A pressure correction equation is used to correct the pressure field such that the continuity equation is also satisfied. Because the method uses a non-staggered grid, additional artificial dissipation terms are added to these equations to aid in smoothing out errors and to prevent numerical oscillations of the centrally differenced pressure equation.

Chapter 2 is organized as follows: Section 2.1 presents the governing equations in both their standard and discretized forms. The complete derivation of these equations can be found in the thesis written by Basson [14], and a more general text on the method is that of Patankar [15]. Section 2.2 presents the grid that was used and compares the grid to its predecessors. Section 2.3 compares the results of an initial computation with experimental data for validation of the code.

2.1: Governing Equations

The Reynolds averaged equations of mass and momentum conservation are given in equations 2.1 and 2.2, respectively. Standard tensor notation is used for their presentation, where i represents 1, 2, or 3; j represents summation over 1, 2, and 3; and 1, 2, and 3 correspond to the x , y , and z directions, respectively. Steady (in the mean), constant density flow conditions are assumed in their derivations.

$$\frac{\delta u_i}{\delta x_i} = 0 \quad (2.1)$$

$$\frac{\partial u_i}{\partial t} + \frac{\partial u_i u_j}{\partial x_j} = -\frac{1}{\rho} \left[\frac{\partial p}{\partial x_i} - \frac{\partial}{\partial x_j} \left[\mu \left(\frac{\partial u_j}{\partial x_i} + \frac{\partial u_i}{\partial x_j} \right) + \overline{\rho u'_i u'_j} \right] \right] \quad (2.2)$$

Turbulence closure is obtained via a standard k- ε model, where the Reynolds stress term at the end of equation (2.2) is modeled as:

$$\overline{\rho u'_i u'_j} = -\frac{\partial}{\partial x_i} \left[\frac{2}{3} \rho k \delta_{ij} - \mu_t \left(\frac{\partial u_i}{\partial x_j} + \frac{\partial u_j}{\partial x_i} \right) \right] \quad \text{where } \mu_t = \rho C_\mu f_\mu \frac{k^2}{\varepsilon} \quad (2.3)$$

Conservation equations for k and ε therefore must also be solved. The k and ε equations are given in equations (2.4) and (2.5), respectively.

$$\begin{aligned} \frac{\partial \rho k}{\partial t} + \frac{\partial u_i \rho k}{\partial x_i} = & \\ \frac{\partial}{\partial x_i} \left[(\mu + \mu_t) \frac{\partial k}{\partial x_i} \right] + \mu_t \frac{\partial u_i}{\partial x_j} \left(\frac{\partial u_i}{\partial x_j} + \frac{\partial u_j}{\partial x_i} \right) - \rho \varepsilon - \frac{2\mu k}{(y_w)^2} & \end{aligned} \quad (2.4)$$

$$\begin{aligned} \frac{\partial \varepsilon}{\partial t} + \frac{\partial u_j \varepsilon}{\partial x_j} = & \\ \frac{\partial}{\partial x_i} \left[\left(\mu + \frac{\mu_t}{\sigma_\varepsilon} \right) \frac{\partial \varepsilon}{\partial x_i} \right] + C_1 \mu_t \frac{\varepsilon}{k} \frac{\partial u_i}{\partial x_j} \left(\frac{\partial u_i}{\partial x_j} + \frac{\partial u_j}{\partial x_i} \right) - \frac{\rho \varepsilon}{k} (C_2 f_2 \varepsilon - f_\varepsilon) & \end{aligned} \quad (2.5)$$

The near wall damping functions, f_2 , f_μ , and f_ε are from the k- ε model by Chien (1982). The functions and empirical constants used in the model are given below.

$$f_\mu = 1 - e^{-C_3 y^+} \quad f_2 = 1 - \frac{0.4}{0.8} e^{-(k^2/6\nu\varepsilon)^2} \quad f_\varepsilon = \frac{2\nu k e^{-C_4 y^+}}{(y_w)^2}$$

$$C_\mu = 0.09 \quad \sigma_\varepsilon = 1.3 \quad C_1 = 1.35 \quad C_2 = 1.8 \quad C_3 = 0.0115 \quad C_4 = 0.5$$

The continuity, momentum, and turbulence equations can all be represented in the following general convection-diffusion form:

$$\frac{\partial \rho \phi}{\partial t} + \frac{\partial \rho u_j \phi}{\partial x_j} = \frac{\partial}{\partial x_j} \left(\Gamma^\phi \frac{\partial \phi}{\partial x_j} \right) + S_\phi \quad (2.6)$$

Here, ϕ represents 1, u_i , k , or ϵ for equations (2.1), (2.2), (2.4), and (2.5), respectively. Γ_ϕ represents the corresponding diffusion coefficient, which can be laminar or turbulent. S_ϕ is the source term.

2.1.1: Computational Domain Transform

For its solution, equation (2.6) is first transformed from the real domain (x, y, z) to the computational domain (ξ, η, ζ) and then discretized using finite difference approximations. The computational domain is such that all grid spacings are unity and all grid lines are orthogonal. The transform is accomplished using the chain rule of calculus and Kramer's rule of matrix algebra. The general convection-diffusion equation in the computational domain is given in equation (2.7).

$$\begin{aligned} J \frac{\partial \rho \phi}{\partial t} + \frac{\partial}{\partial \xi} (\rho J G_1 \phi) + \frac{\partial}{\partial \eta} (\rho J G_2 \phi) + \frac{\partial}{\partial \zeta} (\rho J G_3 \phi) = \\ \frac{\partial}{\partial \xi} \left[\Gamma^\phi J \left(\alpha \frac{\partial \phi}{\partial \xi} + \theta_1 \frac{\partial \phi}{\partial \eta} + \theta_2 \frac{\partial \phi}{\partial \zeta} \right) \right] + \frac{\partial}{\partial \eta} \left[\Gamma^\phi J \left(\theta_1 \frac{\partial \phi}{\partial \xi} + \beta \frac{\partial \phi}{\partial \eta} + \theta_3 \frac{\partial \phi}{\partial \zeta} \right) \right] \\ + \frac{\partial}{\partial \zeta} \left[\Gamma^\phi J \left(\theta_2 \frac{\partial \phi}{\partial \xi} + \theta_3 \frac{\partial \phi}{\partial \eta} + \gamma \frac{\partial \phi}{\partial \zeta} \right) \right] + JS_\phi \end{aligned} \quad (2.7)$$

The new geometrical terms in equation (2.7) are defined as follows:

$$G_1 = u_j \frac{\partial \xi}{\partial x_j} \quad G_2 = u_j \frac{\partial \eta}{\partial x_j} \quad G_3 = u_j \frac{\partial \zeta}{\partial x_j}$$

$$\alpha = \frac{\partial \xi}{\partial x_j} \frac{\partial \xi}{\partial x_j} \quad \beta = \frac{\partial \eta}{\partial x_j} \frac{\partial \eta}{\partial x_j} \quad \gamma = \frac{\partial \zeta}{\partial x_j} \frac{\partial \zeta}{\partial x_j} \quad \theta_1 = \frac{\partial \xi}{\partial x_j} \frac{\partial \eta}{\partial x_j} \quad \theta_2 = \frac{\partial \xi}{\partial x_j} \frac{\partial \zeta}{\partial x_j} \quad \theta_3 = \frac{\partial \eta}{\partial x_j} \frac{\partial \zeta}{\partial x_j}$$

$$J = \frac{\partial x_1}{\partial \xi} \left(\frac{\partial x_2}{\partial \eta} \frac{\partial x_3}{\partial \zeta} - \frac{\partial x_2}{\partial \zeta} \frac{\partial x_3}{\partial \eta} \right) + \frac{\partial x_1}{\partial \eta} \left(\frac{\partial x_2}{\partial \xi} \frac{\partial x_3}{\partial \zeta} - \frac{\partial x_2}{\partial \zeta} \frac{\partial x_3}{\partial \xi} \right) + \frac{\partial x_1}{\partial \zeta} \left(\frac{\partial x_2}{\partial \xi} \frac{\partial x_3}{\partial \eta} - \frac{\partial x_2}{\partial \eta} \frac{\partial x_3}{\partial \xi} \right)$$

The terms G_1 , G_2 , and G_3 are the contravariant velocities in the ξ , η , and ζ directions, respectively. J is the Jacobian of the coordinate transform, and α , β , γ , θ_1 , θ_2 , and θ_3 are geometric parameters. The new geometrical terms are calculated using finite difference approximations from the grid. All differences in ξ , η , and ζ are unity.

In addition, two artificial terms are added directly to equation (2.7) for the momentum and turbulence equations. In the transformed coordinates, these terms are:

$$\begin{aligned} & \frac{1}{2} \varepsilon_2 \left[\frac{\partial}{\partial \xi} \left(|\rho J G_1| \frac{\partial \phi}{\partial \xi} \right) + \frac{\partial}{\partial \eta} \left(|\rho J G_2| \frac{\partial \phi}{\partial \eta} \right) + \frac{\partial}{\partial \zeta} \left(|\rho J G_3| \frac{\partial \phi}{\partial \zeta} \right) \right] \\ & - \frac{1}{8} \varepsilon_4 \left[\frac{\partial}{\partial \xi} \left(|\rho J G_1| \frac{\partial^3 \phi}{\partial \xi^3} \right) + \frac{\partial}{\partial \eta} \left(|\rho J G_2| \frac{\partial^3 \phi}{\partial \eta^3} \right) + \frac{\partial}{\partial \zeta} \left(|\rho J G_3| \frac{\partial^3 \phi}{\partial \zeta^3} \right) \right] \end{aligned} \quad (2.8)$$

These terms act to artificially diffuse errors out of the solution. The coefficients ε_2 and ε_4 are referred to as the 2nd and 4th order artificial viscosity, respectively, and are specified as input to the code. In any final solution, ε_2 and ε_4 should be set as low as possible to avoid corrupting the solution with these nonphysical diffusion effects.

2.1.2: Finite Difference Form

A control volume around a grid point P is used for the discretization of equation (2.7). Such a control volume is shown in figure 2.1.

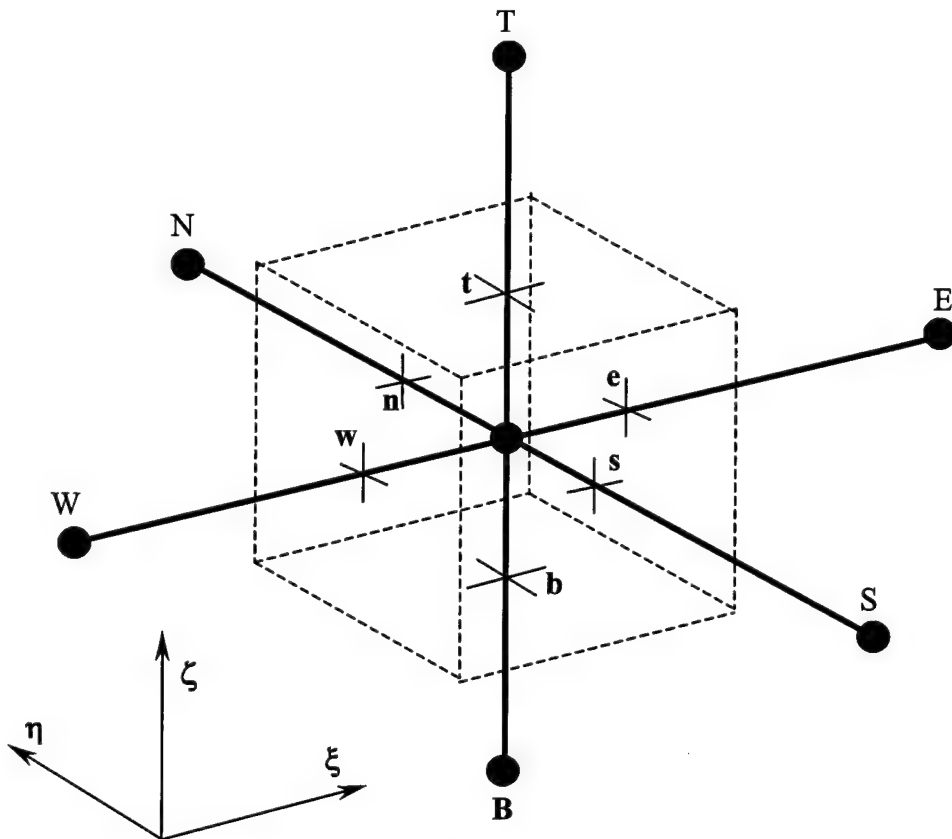


Figure 2.1: Control Volume with Grid Notation

Upper case letters represent grid points in the computational domain (N = north), while lower case letters represent the faces of the control volume. The final form of the discretized general convection-diffusion equation will be as follows:

$$SOURCE = a_p \phi_p + a_E \phi_E + a_W \phi_W + a_N \phi_N + a_S \phi_S + a_T \phi_T + a_B \phi_B$$

The subscripts indicate the grid point location.

For stability reasons, it is beneficial if the above equation can be solved in an implicit manner. The SOURCE term and “a” coefficients are always found explicitly from grid geometry information and current values of ϕ . New values of ϕ are found using a tridiagonal matrix solver in a semi-implicit manner. For example, the terms $a_N\phi_N$, $a_S\phi_S$, $a_T\phi_T$, and $a_B\phi_B$ will be found explicitly and subtracted from the SOURCE term for all grid points along a line of constant ξ . Since ϕ_P is equivalent to ϕ_E for the grid point to the left and ϕ_W for the grid point on the right, including boundary conditions will result in a set of n equations and n unknowns. These equations make up an easily solvable tridiagonal matrix, with n values of ϕ_P as the unknowns. After solving for new values of ϕ_P , the process is repeated along lines of constant η (ϕ_P , ϕ_N , and ϕ_S treated implicitly), and constant ζ (ϕ_P , ϕ_T , and ϕ_B treated implicitly).

2nd order accurate central differencing is used for both convection and real diffusion terms. For example, the convection derivative in the ξ direction is discretized as follows:

$$\frac{\partial}{\partial \xi} [\rho J G_1 \phi] = \frac{(\rho J G_1)_e \phi_e - (\rho J G_1)_w \phi_w}{\Delta \xi} \quad \text{where} \quad \Delta \xi = \Delta \eta = \Delta \zeta = 1 \quad (2.9)$$

The values at the control volume faces come from linear interpolation. For example:

$$\phi_e = \frac{1}{2}(\phi_E + \phi_P) \quad \text{and} \quad \phi_w = \frac{1}{2}(\phi_P + \phi_W)$$

The diffusion terms are modeled similarly, as follows:

$$\begin{aligned} \frac{\partial}{\partial \xi} \left[\Gamma^{\phi} J \left(\alpha \frac{\partial \phi}{\partial \xi} + \theta_1 \frac{\partial \phi}{\partial \eta} + \theta_2 \frac{\partial \phi}{\partial \zeta} \right) \right] &= \left(\Gamma^{\phi} J \alpha \right)_e \left(\frac{\partial \phi}{\partial \xi} \right)_e - \left(\Gamma^{\phi} J \alpha \right)_w \left(\frac{\partial \phi}{\partial \xi} \right)_w \quad (2.10) \\ &+ \left(\Gamma^{\phi} J \theta_1 \right)_e \left(\frac{\partial \phi}{\partial \eta} \right)_e - \left(\Gamma^{\phi} J \theta_1 \right)_w \left(\frac{\partial \phi}{\partial \eta} \right)_w + \left(\Gamma^{\phi} J \theta_2 \right)_e \left(\frac{\partial \phi}{\partial \zeta} \right)_e - \left(\Gamma^{\phi} J \theta_2 \right)_w \left(\frac{\partial \phi}{\partial \zeta} \right)_w \end{aligned}$$

In equation (2.10), derivatives at the control volume faces are central difference approximated. Cross derivative terms are calculated on either side of the face and then averaged. Examples of these approximations are given below.

$$\begin{aligned} \left(\frac{\partial \phi}{\partial \xi} \right)_e &= \frac{(\phi_E - \phi_P)}{\Delta \xi} & \left(\frac{\partial \phi}{\partial \xi} \right)_w &= \frac{(\phi_P - \phi_W)}{\Delta \xi} \\ \left(\frac{\partial \phi}{\partial \eta} \right)_e &= \frac{1}{2(\Delta \eta)} \left(\frac{(\phi_N - \phi_S)}{2(\Delta \eta)} + \frac{(\phi_{NE} - \phi_{SE})}{2(\Delta \eta)} \right) \\ \left(\frac{\partial \phi}{\partial \eta} \right)_w &= \frac{1}{2(\Delta \eta)} \left(\frac{(\phi_N - \phi_S)}{2(\Delta \eta)} + \frac{(\phi_{NW} - \phi_{SW})}{2(\Delta \eta)} \right) \end{aligned}$$

It can be seen here that the modeling of cross derivative diffusion terms will require additional grid points other than the ones shown in figure 2.1. In order to solve the final equations with a tridiagonal matrix solver, these points will need to be treated explicitly.

The 2nd order artificial diffusion term is modeled in the same manner as the real diffusion terms. The 4th order artificial term is calculated by the central difference approximation of two 3rd order artificial derivatives, as is shown in equation 2.11.

$$\begin{aligned}
 \left(\frac{\partial^3 \phi}{\partial \xi^3} \right)_e &= -\phi_w + 3\phi_p - 3\phi_e + \phi_{ee} \quad \text{and} \quad \left(\frac{\partial^3 \phi}{\partial \xi^3} \right)_w = -\phi_{ww} + 3\phi_w - 3\phi_p + \phi_e \\
 \frac{\partial}{\partial \xi} \left[\left| \rho J G_1 \right| \left(\frac{\partial^3 \phi}{\partial \xi^3} \right) \right] &= \left[\left| \rho J G_1 \right| \left(\frac{\partial^3 \phi}{\partial \xi^3} \right) \right]_e - \left[\left| \rho J G_1 \right| \left(\frac{\partial^3 \phi}{\partial \xi^3} \right) \right]_w \\
 &= \left| \rho J G_1 \right|_e \left(-\phi_w + 3\phi_p - 3\phi_e + \phi_{ee} \right) - \left| \rho J G_1 \right|_w \left(-\phi_{ww} + 3\phi_w - 3\phi_p + \phi_e \right)
 \end{aligned} \tag{2.11}$$

No cross derivatives are present in the artificial terms. The third order derivative approximations in equation (2.11) can be written as:

$$(2.12) \left(\frac{\partial^3 \phi}{\partial \xi^3} \right)_e = -\phi_w + 3\phi_p - 3\phi_e + \phi_{ee} = (-\phi_w - \phi_p + \phi_e + \phi_{ee}) - 4(-\phi_p + \phi_e)$$

Again, the use of a tridiagonal solution technique requires that the terms in the first brackets on the right side of equation (2.12) must be treated explicitly.

The final discretized form of the general convection-diffusion equation is presented in equation (2.13). S_ϕ is the source term for the particular equation being solved: either the pressure term in the momentum equations or the production and dissipation terms in the turbulence equations. These terms are first transformed to the computational domain by the method described in section 2.1.1, and then discretized using central differencing. Their treatment is always explicit.

$$a_p \phi_p = a_E \phi_E + a_W \phi_W + a_N \phi_N + a_S \phi_S + a_T \phi_T + a_B \phi_B + S_\phi^* \quad (2.13)$$

where

$$a_E = -\frac{1}{2}(\rho J G_1)_e + (\Gamma^\phi J \alpha)_e + \frac{1}{2}(\varepsilon_2 + \varepsilon_4)|(\rho J G_1)_e|$$

$$a_W = \frac{1}{2}(\rho J G_1)_w + (\Gamma^\phi J \alpha)_w + \frac{1}{2}(\varepsilon_2 + \varepsilon_4)|(\rho J G_1)_w|$$

$$a_N = -\frac{1}{2}(\rho J G_2)_n + (\Gamma^\phi J \beta)_n + \frac{1}{2}(\varepsilon_2 + \varepsilon_4)|(\rho J G_2)_n|$$

$$a_S = \frac{1}{2}(\rho J G_2)_s + (\Gamma^\phi J \beta)_s + \frac{1}{2}(\varepsilon_2 + \varepsilon_4)|(\rho J G_2)_s|$$

$$a_T = -\frac{1}{2}(\rho J G_3)_t + (\Gamma^\phi J \gamma)_t + \frac{1}{2}(\varepsilon_2 + \varepsilon_4)|(\rho J G_3)_t|$$

$$a_B = \frac{1}{2}(\rho J G_3)_b + (\Gamma^\phi J \gamma)_b + \frac{1}{2}(\varepsilon_2 + \varepsilon_4)|(\rho J G_3)_b|$$

$$a_p = a_E + a_W + a_N + a_S + a_T + a_B + [(\rho J G_1)_e - (\rho J G_1)_w + (\rho J G_2)_n - (\rho J G_2)_s + (\rho J G_3)_t - (\rho J G_3)_b]$$

$$S_\phi^* = JS_\phi + [Cross\ Derivative\ Terms] + [Explicit\ Artificial\ Viscosity\ Terms]$$

2.1.3: Pressure Correction Equation

The continuity equation does not lend itself well to solution techniques in conjunction with the momentum. The reason for this is the lack of a pressure term in the continuity equation. An alternative approach is to solve a pressure or pressure correction equation derived directly from the discretized continuity and momentum equations. This is the essence of the Semi-Implicit Method for Pressure Linked Equations (SIMPLE) scheme developed by Patankar [15].

The pressure correction equation can be derived as follows: First, the discretized momentum equations are substituted into the discretized continuity equation, resulting in an expression for pressure in terms of velocity at any of the grid points. Then, the exact pressure in this equation is replaced by the sum of the current guessed pressure value, p^* , and a pressure correction value p' . If the current velocity and pressure values satisfy the momentum equations, then these equations, using p^* and not p , can be subtracted from the pressure correction equation. The final pressure correction equation is given in equation (2.14).

$$\begin{aligned}
 a_p p'_p = & [a_{ew}]_e p'_E + [a_{ew}]_w p'_W + [a_{ns}]_n p'_N + [a_{ns}]_s p'_S + [a_{tb}]_t p'_T + [a_{tb}]_b p'_B \\
 & - [\rho JG_1^*]_e + [\rho JG_1^*]_w - [\rho JG_2^*]_n + [\rho JG_2^*]_s - [\rho JG_3^*]_t + [\rho JG_3^*]_b \\
 & - [\rho J\hat{G}_1']_e + [\rho J\hat{G}_1']_w - [\rho J\hat{G}_2']_n + [\rho J\hat{G}_2']_s - [\rho J\hat{G}_3']_t + [\rho J\hat{G}_3']_b \\
 & + \left[E_2 J \left(\theta_1 \frac{\partial p'}{\partial \eta} + \theta_2 \frac{\partial p'}{\partial \zeta} \right) \right]_e - \left[E_2 J \left(\theta_1 \frac{\partial p'}{\partial \eta} + \theta_2 \frac{\partial p'}{\partial \zeta} \right) \right]_w \\
 & + \left[E_2 J \left(\theta_1 \frac{\partial p'}{\partial \xi} + \theta_3 \frac{\partial p'}{\partial \zeta} \right) \right]_n - \left[E_2 J \left(\theta_1 \frac{\partial p'}{\partial \xi} + \theta_3 \frac{\partial p'}{\partial \zeta} \right) \right]_s \\
 & + \left[E_2 J \left(\theta_2 \frac{\partial p'}{\partial \xi} + \theta_3 \frac{\partial p'}{\partial \eta} \right) \right]_t - \left[E_2 J \left(\theta_2 \frac{\partial p'}{\partial \xi} + \theta_3 \frac{\partial p'}{\partial \eta} \right) \right]_b
 \end{aligned} \tag{2.14}$$

where

$$E = \frac{1}{a_p - \sum_{nb} a_{nb}}, \quad nb = E, W, N, S, T, B \quad \text{and} \quad a = \text{coef. from (2.13)}$$

$$a_{ew} = \rho E J^2 \alpha \quad a_{ns} = \rho E J^2 \beta \quad a_{tb} = \rho E J^2 \gamma \quad E_2 = \rho E J$$

$$\hat{u}_p = E \left[\sum_{nb} a_{nb} (u_{nb} - u_p) + S_u \right]$$

$$\hat{v}_p = E \left[\sum_{nb} a_{nb} (v_{nb} - v_p) + S_v \right]$$

$$\hat{w}_p = E \left[\sum_{nb} a_{nb} (w_{nb} - w_p) + S_w \right]$$

$$u_i = \text{correct} = u_i^* + u_i' = \text{current} + \text{correction} \quad (i=1,2,3)$$

$$\hat{u}_i = \text{correct} = \hat{u}_i^* + \hat{u}_i' = \text{current} + \text{correction} \quad (i=1,2,3)$$

$$G_1^* = u_j^* \frac{\partial \xi}{\partial x_j} \quad G_2^* = u_j^* \frac{\partial \eta}{\partial x_j} \quad G_3^* = u_j^* \frac{\partial \zeta}{\partial x_j}$$

$$\hat{G}_1' = \hat{u}_j' \frac{\partial \xi}{\partial x_j} \quad \hat{G}_2' = \hat{u}_j' \frac{\partial \eta}{\partial x_j} \quad \hat{G}_3' = \hat{u}_j' \frac{\partial \zeta}{\partial x_j}$$

In addition, a 4th order artificial dissipation similar to that in equation (2.8) is included in the pressure correction equation. This is necessary because the central differencing in the pressure correction equation leads to an odd-even decoupling effect, which is described in detail in the text by Patankar [15]. The coefficient ϵ_{pw} is specified directly and should be chosen as small as possible. The additional term is shown in equation (2.15), and its discretization is similar to that of the 4th order artificial term in the general convection-diffusion equation.

$$\frac{1}{4} \epsilon_{pw} \left[\frac{\partial}{\partial \xi} \left(a_{ew} \frac{\partial^3 p}{\partial \xi^3} \right) + \frac{\partial}{\partial \eta} \left(a_{ns} \frac{\partial^3 p}{\partial \eta^3} \right) + \frac{\partial}{\partial \zeta} \left(a_{tb} \frac{\partial^3 p}{\partial \zeta^3} \right) \right] \quad (2.15)$$

2.1.4: Boundary Conditions

There are four types of boundaries to the computation region. The boundary conditions that were implemented on these four types of boundaries are explained below.

Inlet:

Inlet velocity and turbulence profiles are read directly into the code. For this thesis, the origin of these profiles is dependent upon the case being run. For the code validation case in chapter two, the boundary layer thickness and freestream turbulence intensity were chosen to agree with the experimental results being compared with. These values were approximately 10% of the chord length for the boundary layer thickness and 2% of the inlet velocity for turbulence intensity. The inlet turbulence length scale was unknown from the experiment and chosen as approximately 10% of the chord length. For the boundary layer profile, the commercial CFD code Fluent was used to compute a 2D flat plate boundary layer with the same freestream conditions as are given above. The profile at the proper thickness was then used for the inlet conditions. For the boundary layer computation, a full Reynolds stress turbulence model was used, which was most likely calibrated using experimental flat plate boundary layer measurement data.

The Fluent-calculated inlet profile was also used for the reduced clearance case presented in chapter 3. In the cases in chapter 4, a more realistic inlet profile was used. This second profile was computed in the manner explained in section 1.3.

Pressure is assumed to be unchanging in the flow direction at the inlet. Therefore, the inlet should be located far enough upstream of the blades to ensure that this assumption is valid. For this study, the inlet was placed 0.6 chord lengths upstream of the blade leading edge.

Exit:

All convection and diffusion terms for velocities and turbulence quantities are computed directly at the exit plane with no direct enforcement of a boundary condition. Static pressure at the exit is directly specified as zero. To ensure that this assumption is valid, the exit plane must be chosen far downstream of any blading. For this study, the exit plane is located approximately two chord lengths downstream of the blade trailing edge.

Solid Surfaces:

Setting velocities and the turbulent kinetic energy to zero on all solid boundaries enforces the no-slip condition. The exception to this is at the outer casing, where the velocity in the tangential direction is set to a constant, in order to simulate endwall relative motion in the planar geometry. For relative endwall motion in an annular geometry, two Cartesian velocity components must be specified, with their values depending on the angular location on the wall. The near-wall damping terms of Chien also require that the dissipation rate, ε , be set to zero on all solid boundaries.

Wall pressure is determined by setting the pressure gradient normal to the surface equal to zero. In order to ensure the validity of this assumption, as well as that of the turbulence model, the first grid point out from each solid boundary is placed at a y^+ distance of order one.

Periodic Boundaries:

Outside of extreme operating conditions, the flow through a turbomachinery blade row is periodic, that is, the flow at any location in the blade row is identical to the flow at a point N blade spacings away in the tangential direction, where N is some integer. This simplifies turbomachinery computations considerably, since the flow only needs to be solved for across one blade spacing. The periodic definition stated above is enforced numerically for all boundary points that are not solid, inlet, or exit. Annular geometry requires that cylindrical velocities be made equivalent and not Cartesian velocities.

2.2: Grid

The CFD code used in this thesis was specifically written for H type grids with additional grid points embedded into the tip gap. This type of grid is common in turbomachinery computation where the use of a multiblock grid is not possible. One problem that is common with embedded H type grids is the excessive number of grid points present within a small location upstream and downstream of the leading and trailing edges, respectively. Additional problems are grid skewness and large aspect ratios in the gap near the leading and trailing edges.

The embedded H grid used in this study is shown in figures 2.1(a) and 2.1(b). The embedded region has been widened considerably, alleviating the over-clustering around the periodic line. The new grid also allows for more efficient clustering of grid points along the blade surfaces, for better resolution of the boundary layer. Finally, grid clustering near the leading and trailing edges of the blade was incorporated in order to improve the average grid cell aspect ratio in those regions.

The biggest drawback to the modified grid came in its generation. An H grid developing code written by Basson [14] was modified substantially and then used to generate the region labeled “inner” in figure 2.1(a). This code uses a combination of algebraic and elliptic methods, in conjunction with the Minimal Residual Method, for generating smooth grids. The Embedded region, labeled as such, was developed using mostly algebraic techniques. Grid stretching in the ξ direction for this region was accomplished using a ratio method, which matches the ratios of distances between grid points along lines of constant ξ to a corresponding ratio at the inner region’s north or south boundary. Polynomial splines were used in this region in order to match the slopes between the inner and embedded regions, ensuring a smooth transition between grid cells in the η direction. Certain grid points near the intersection of the blade leading or trailing edge and the two regions were smoothed on an individual basis.

Because there is no variation of the blade profile in the spanwise direction, the baseline case 3D grid is created by simply stacking up the 2D grid in figure 2.1. The distribution in the spanwise direction was created by primarily algebraic methods. Spacing near the hub, casing, and tip were chosen small enough to give an approximate y^+ value in single digits. Grid points were heavily clustered near the tip, with 28 spanwise grid points in the gap and 60 spanwise grid points within six gap heights of the tip. A total of 103 and 161 grid points were used in the spanwise and axial directions, respectively. In the tangential direction, 50 and 26 grid points were used across the inner and embedded regions, respectively. Additional, non-uniform grid stretching in the spanwise direction was used to create the three chamfered grids used in this study.

2.2.1: Coordinate System

The Cartesian coordinate system used throughout the thesis is shown in figure 2.1. Coordinates X, Y, and Z correspond to the axial, tangential, and spanwise directions, respectively. In addition, two more directions are referred to throughout the thesis. The “2D Streamwise” direction refers to the direction of the 2D, inviscid, potential flow through the passage. The “Principle Normal” direction refers to the direction normal to the 2D streamwise direction in the blade-to-blade plane and towards the pressure surface. The generic term “Secondary Flow” refers to total flow in the principle normal and spanwise direction, and is thus the deviation of the flow from its 2D designed course.

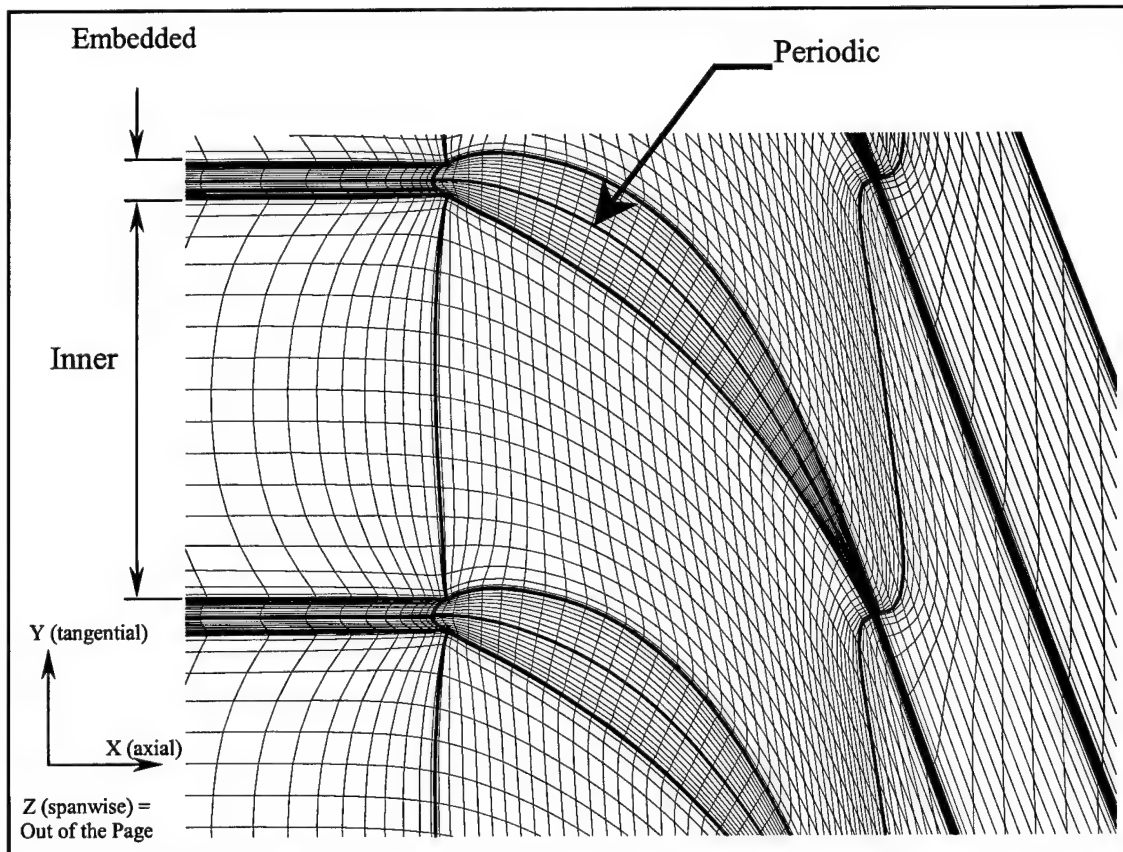


Figure 2.2(a): Grid (Every Other Gridline Shown)

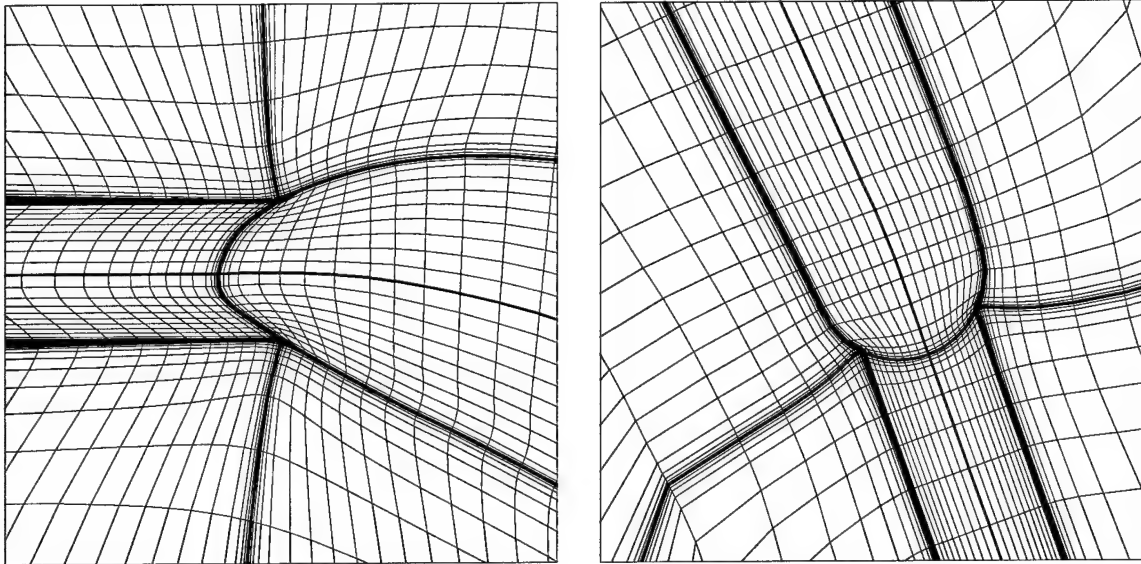


Figure 2.2(b): Embedded Grid near the Leading and Trailing Edges

2.3: Code Validation

In order to validate the CFD code, and as a baseline reference, the flow through the turbine cascade described in table 1.1 was computed and compared with experimental data due to Bindon [5,12]. Basson [14] and Engrebretsen [16] have carried out similar computations with the same code. Both studies yielded results similar to those found in this study. Overall, the solution method using k-e turbulence closure is able to resolve the size, magnitude, and location of the tip leakage flow.

The pitchwise flow angle is defined as the angle between the total flow in the blade-to-blade plane and the axial direction, and is positive if the flow has a velocity component in the positive tangential direction. The spanwise flow angle is defined as the angle between the total velocity in three dimensions and the blade-to-blade plane, and is

positive if the flow has a velocity component in the positive spanwise direction.

Figure 2.3 compares the computed and measured pitchwise flow angles. Figure 2.4 shows the same comparison for the spanwise flow angle. Both figures are presented in three parts: parts a, b, and c correspond to axial locations of 60, 80, and 90 percent of the axial distance downstream of the blade leading edge, respectively. For each part, the variation of the angle in the spanwise direction is shown at eight different pitch locations ranging from pressure to suction surfaces. The term “Percent Pitch” is used to refer to the percentage of the distance in the tangential direction from the pressure surface to the suction surface.

At 60% chord, the magnitude of the leakage vortex location is found to be slightly closer to the blade than in the measured case. Figure 2.3(a) shows the pitchwise flow angles to be in good agreement except at the 80 and 90 percent pitch locations. These locations exhibit the same trends, but to a lesser extent for the numerical solution. In figure 2.4(a), the same trends are seen for the spanwise flow angle. Furthermore, at 60, 70, and 80 percent pitch locations, the computed spanwise flow angle at one pitch location appears to be predicted in better agreement with the experimental data at a pitch location further from the suction surface. This indicates that the code is predicting the vortex slightly closer to the blade than is observed experimentally. The computed pitchwise flow angle distributions at 80 and 90 percent pitch show a smaller leakage jet velocity and this, too, indicates a vortex located closer to the blade.

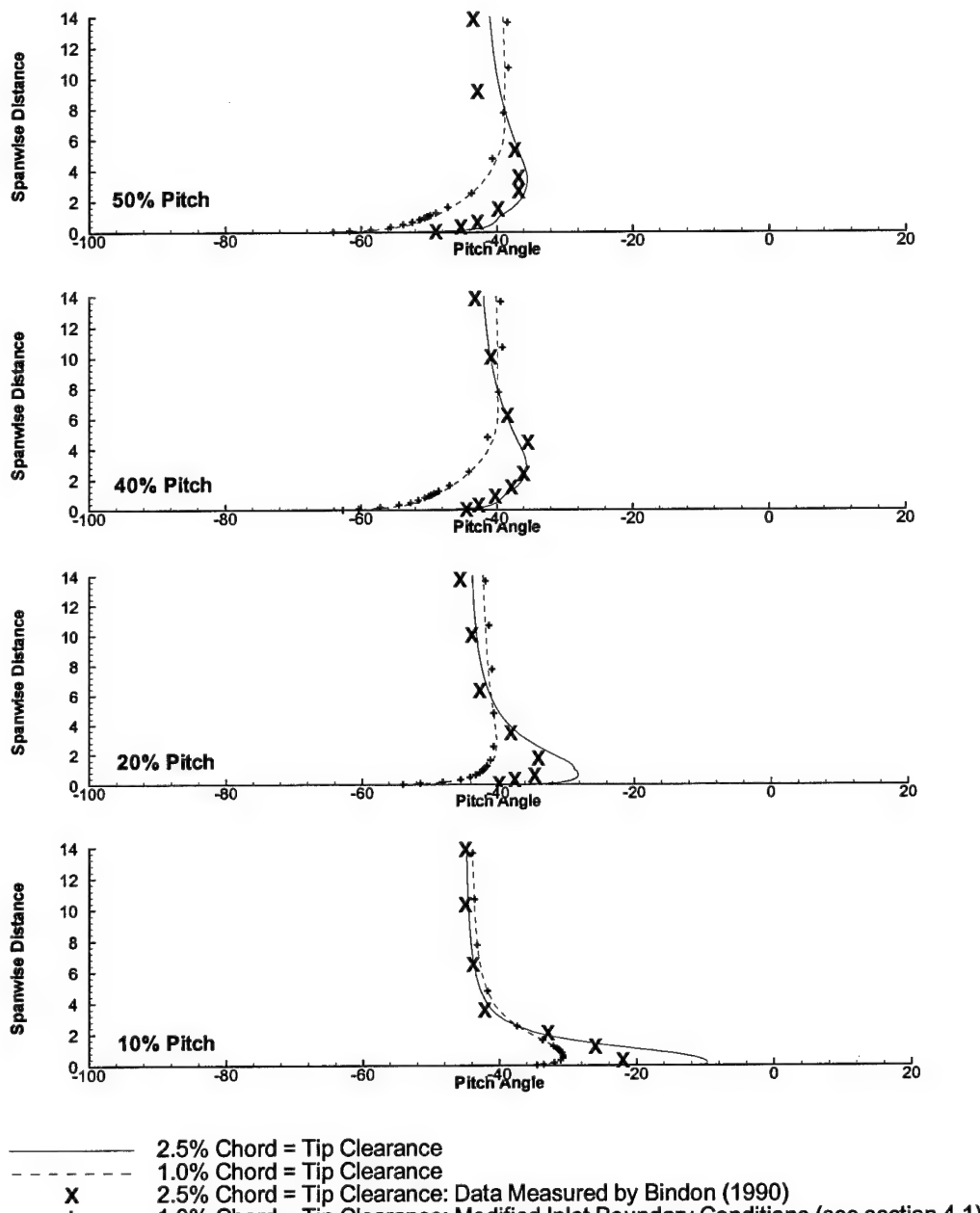
Figures 2.3(b) and 2.4(b) show the measured and predicted pitchwise and spanwise flow angles, respectively, at an axial location of 80% chord from the leading

edge. The spanwise flow angle distributions show that the vortex placement is still nearer to the suction surface for the computed flow than in the measured flow. At 60% pitch, the measured leakage flow has begun to wrap around back toward the suction surface, while the predicted case does not exhibit this trend until about 70% pitch. At 80% pitch, figure 2.4(b) shows the measured vortex to be on its upward return while the predicted vortex is still penetrating toward the hub. Figure 2.3(b) shows the same trends. At 70% pitch, the measured leakage velocity is quite prevalent, while the predicted case still shows signs of the passage vortex, with a pitchwise flow angle less than the value far from the casing. For the region of the passage closer to the pressure surface, the flow is well predicted. This is also the case with the flow adjacent to the suction surface (90% pitch).

The flow angles at 90% chord downstream of the leading edge are presented in part (c) of figures 2.3 and 2.4, and the trends are very much the same as at 80% chord. The predicted vortex is still slightly closer to the suction surface than the measured vortex. This is most noticeable at 60% pitch for the pitchwise flow angle and at 70% pitch for the spanwise flow angle. Both measured and predicted angles begin to show the absence of the passage vortex, as it is beginning to be pulled underneath the leakage vortex.

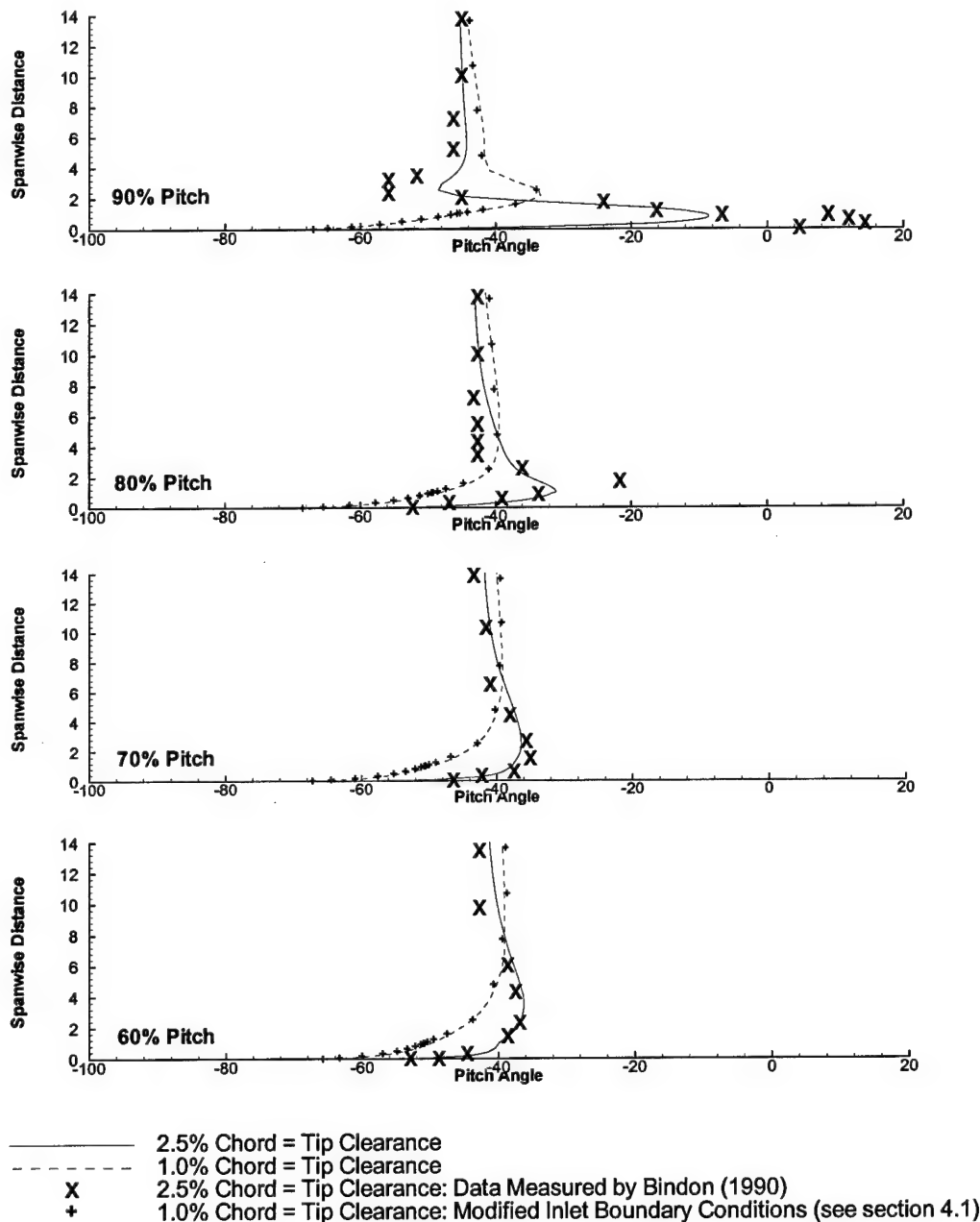
Overall, figures 2.3 and 2.4 show that the CFD code being used is capable of predicting the fine details of the complex flow phenomenon in turbomachinery. The use of an isotropic turbulence model in the prediction could be accountable for the slight discrepancy in the location of the vortex for the predicted and measured flows. Also,

there is some uncertainty by the author as to whether the experimental data was taken at pitch locations defined by the distance from blade to blade or from suction surface to pressure surface. If the former case were true, then this would place the experimental vortex closer to the suction surface and in better agreement with the predicted case. Overall, the code does a quality job of predicting complex 3D flow features and should lend itself well to the simulations presented in this study.



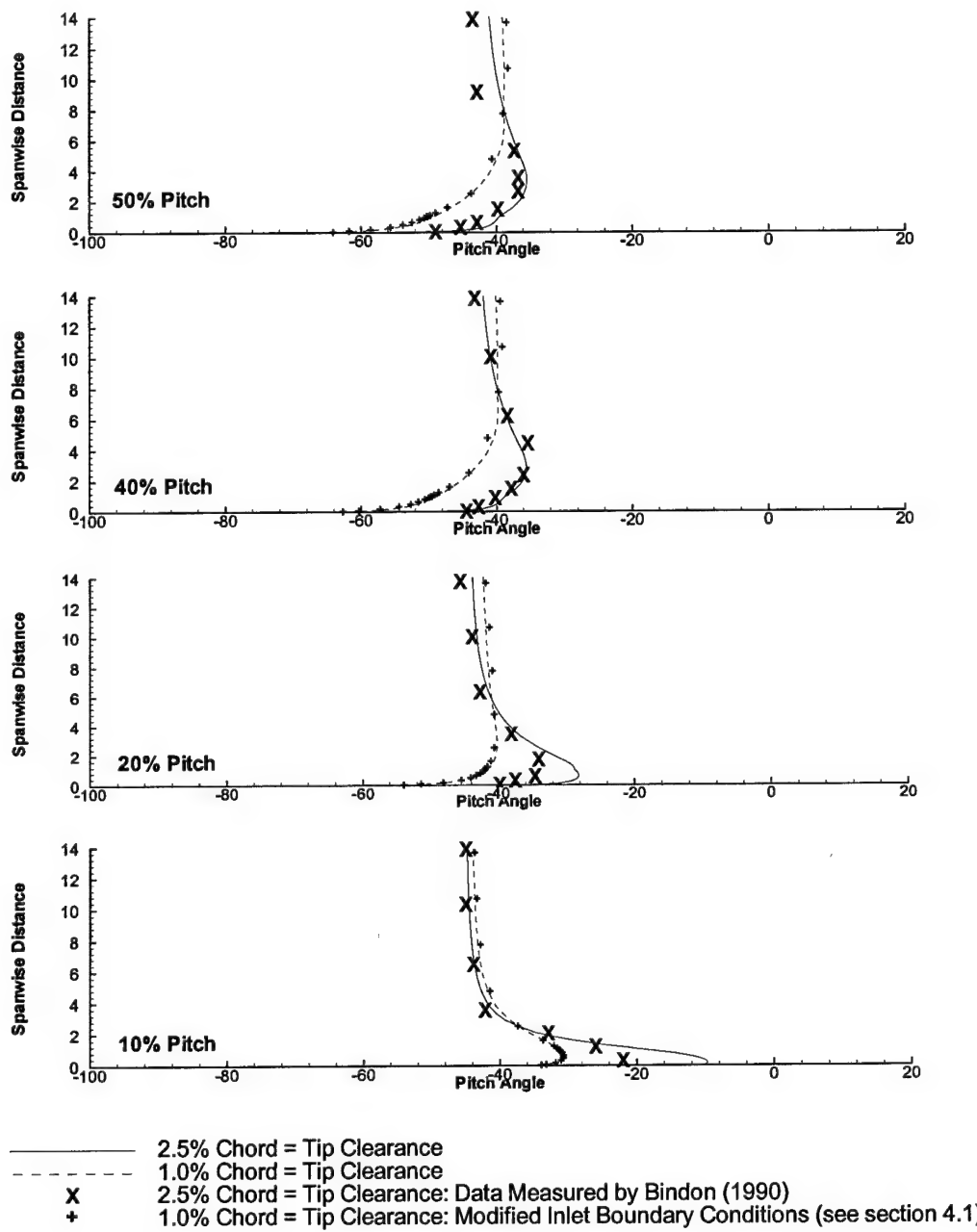
- (1) positive pitch angle is toward the pressure surface.
- (2) Spanwise Distance = spanwise distance from casing/clearance height
- (3) percent pitch is the percent of the distance from pressure surface to suction surface.

Figure 2.3: Pitch Angle near the Casing
Part (a): X = 60% Axial Chord



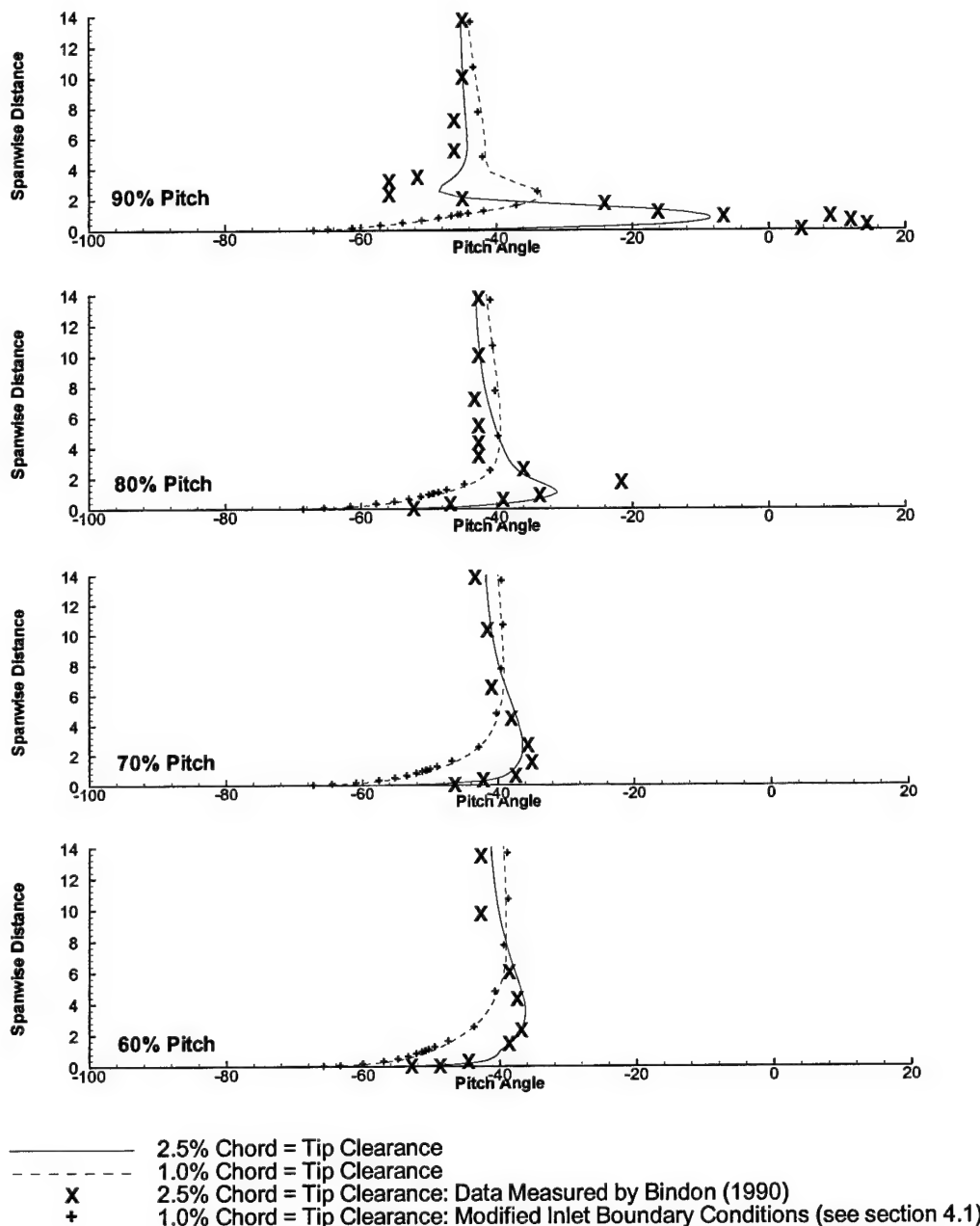
- (1) positive pitch angle is toward the pressure surface.
- (2) Spanwise Distance = spanwise distance from casing/clearance height
- (3) percent pitch is the percent of the distance from pressure surface to suction surface.

Figure 2.3 (continued): Pitch Angle near the Casing
Part (a): X = 60% Axial Chord



- (1) positive pitch angle is toward the pressure surface.
- (2) Spanwise Distance = spanwise distance from casing/clearance height
- (3) percent pitch is the percent of the distance from pressure surface to suction surface.

Figure 2.3: Pitch Angle near the Casing
Part (b): X = 80% Axial Chord



- (1) positive pitch angle is toward the pressure surface.
- (2) Spanwise Distance = spanwise distance from casing/clearance height
- (3) percent pitch is the percent of the distance from pressure surface to suction surface.

Figure 2.3 (continued): Pitch Angle near the Casing
Part (b): X = 80% Axial Chord

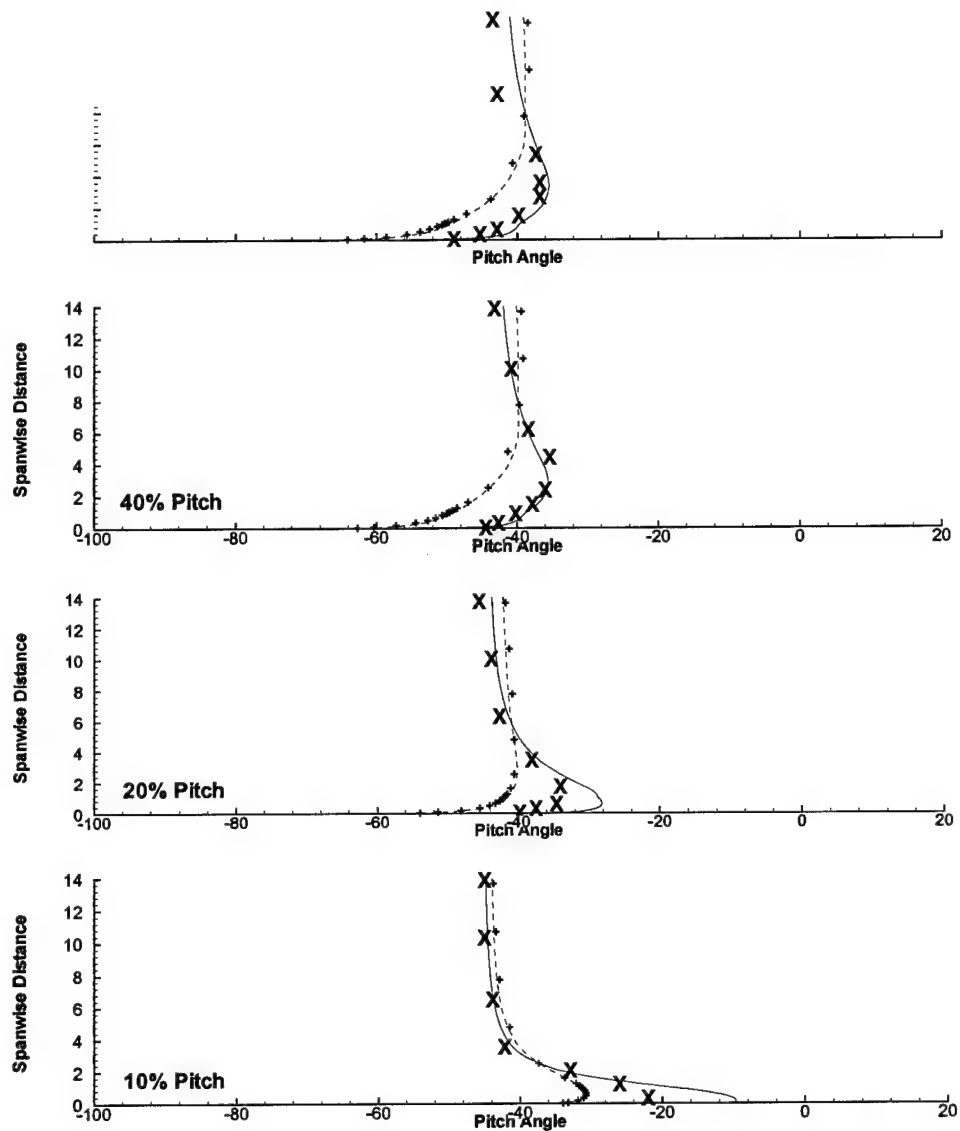
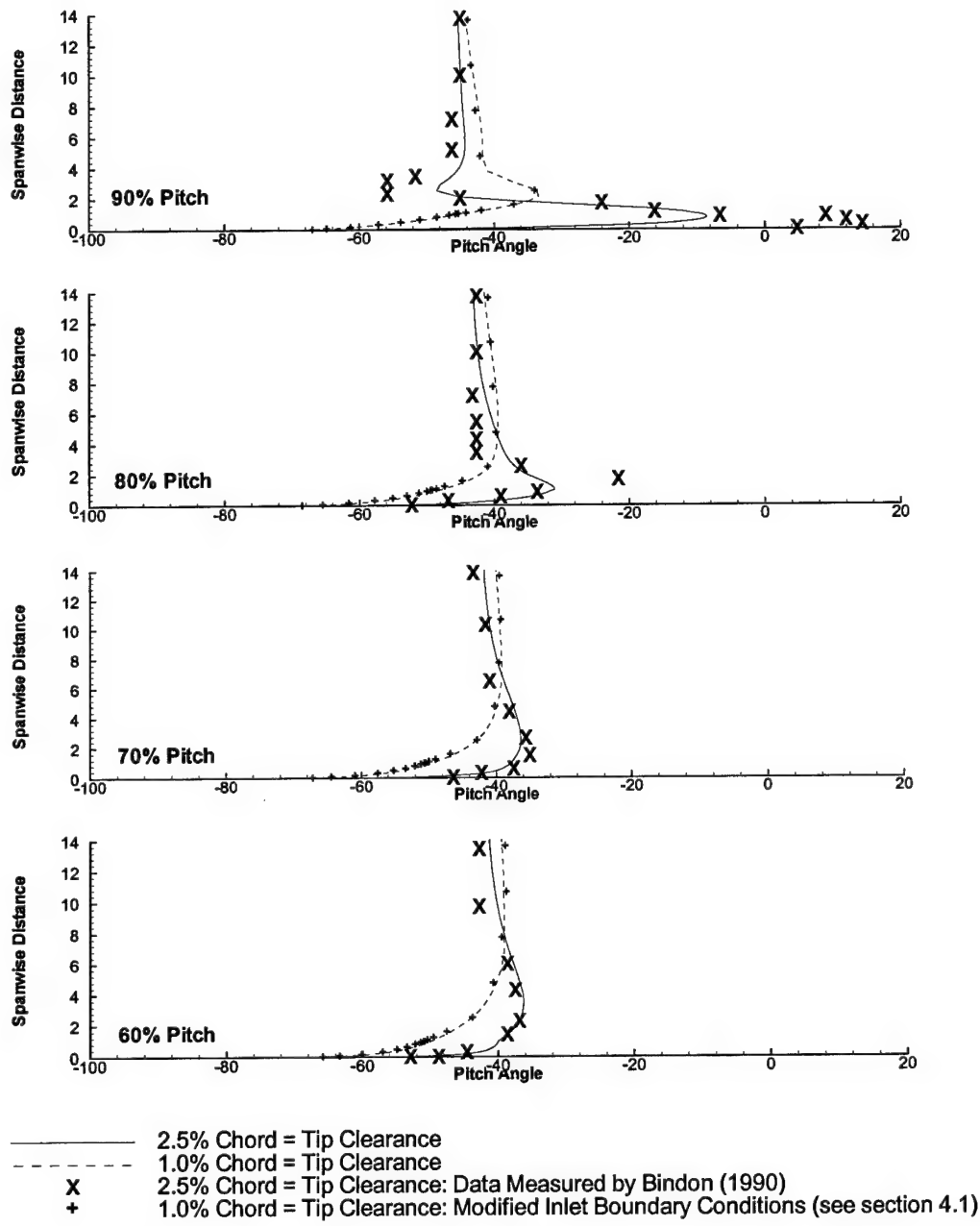


Figure 2.3: Pitch Angle near the Outer Casing
Part (c): X = 90% Axial Chord



- (1) positive pitch angle is toward the pressure surface.
- (2) Spanwise Distance = spanwise distance from casing/clearance height
- (3) percent pitch is the percent of the distance from pressure surface to suction surface.

Figure 2.3 (continued): Pitch Angle near the Casing
Part (c): X = 90% Axial Chord

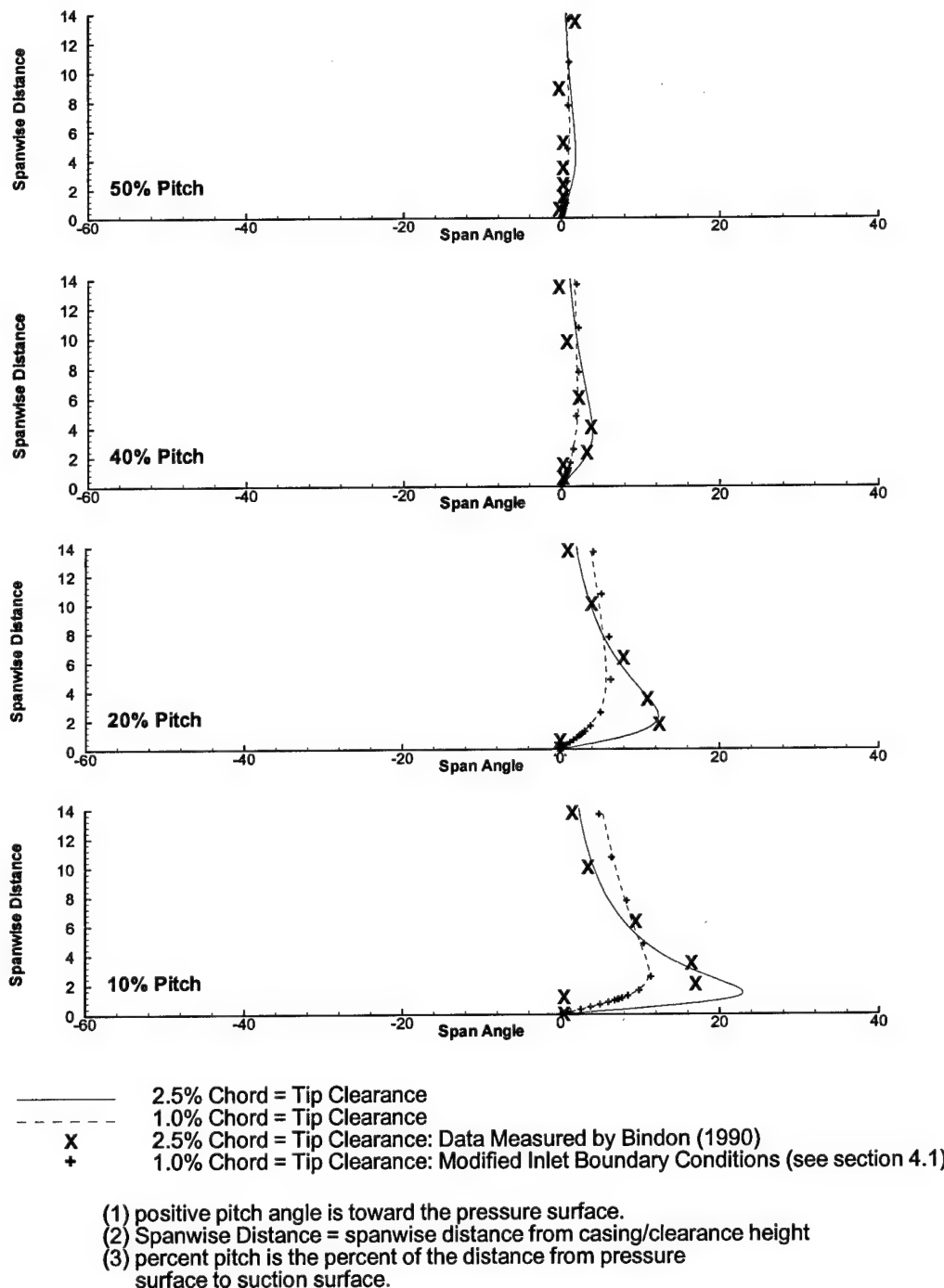
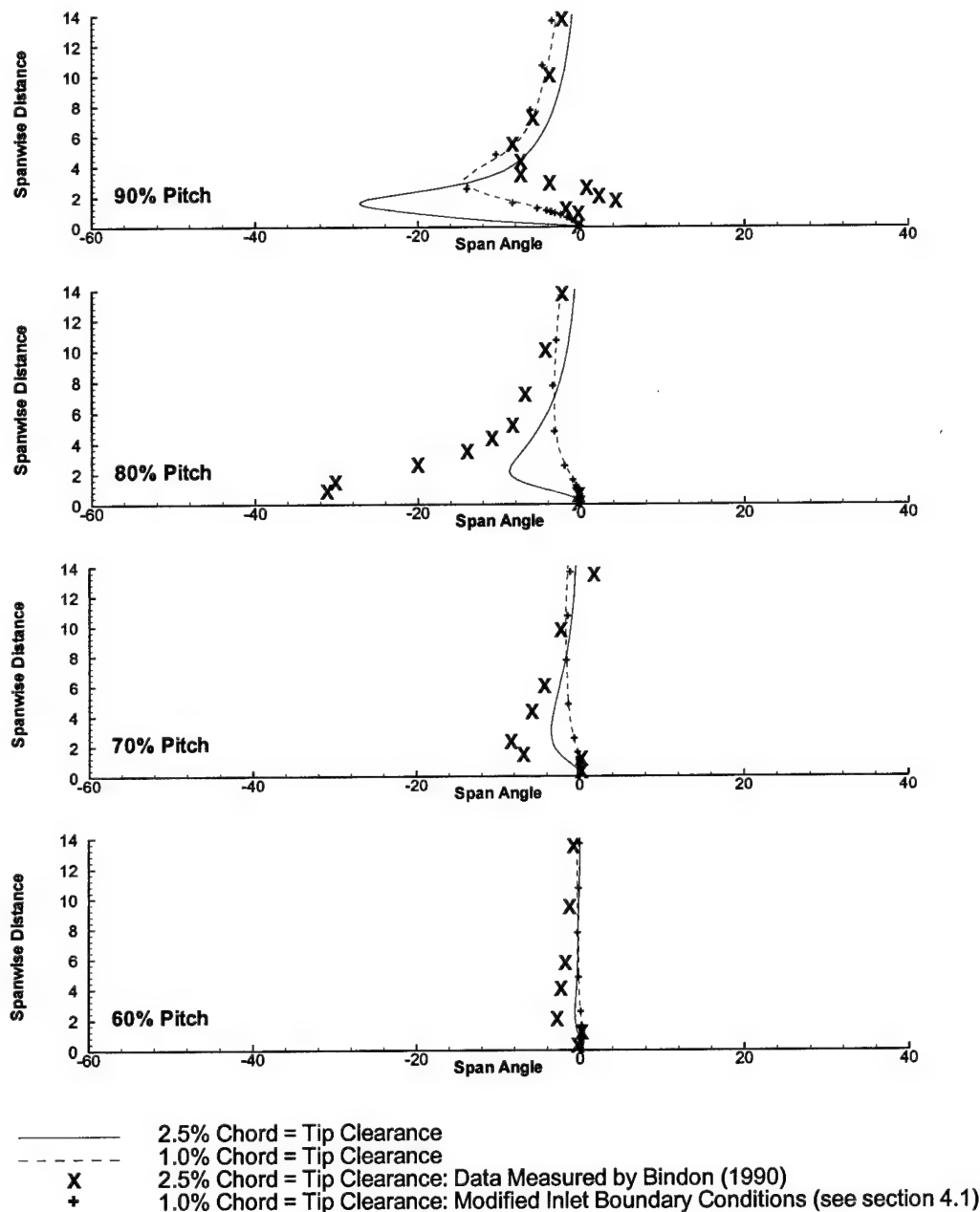
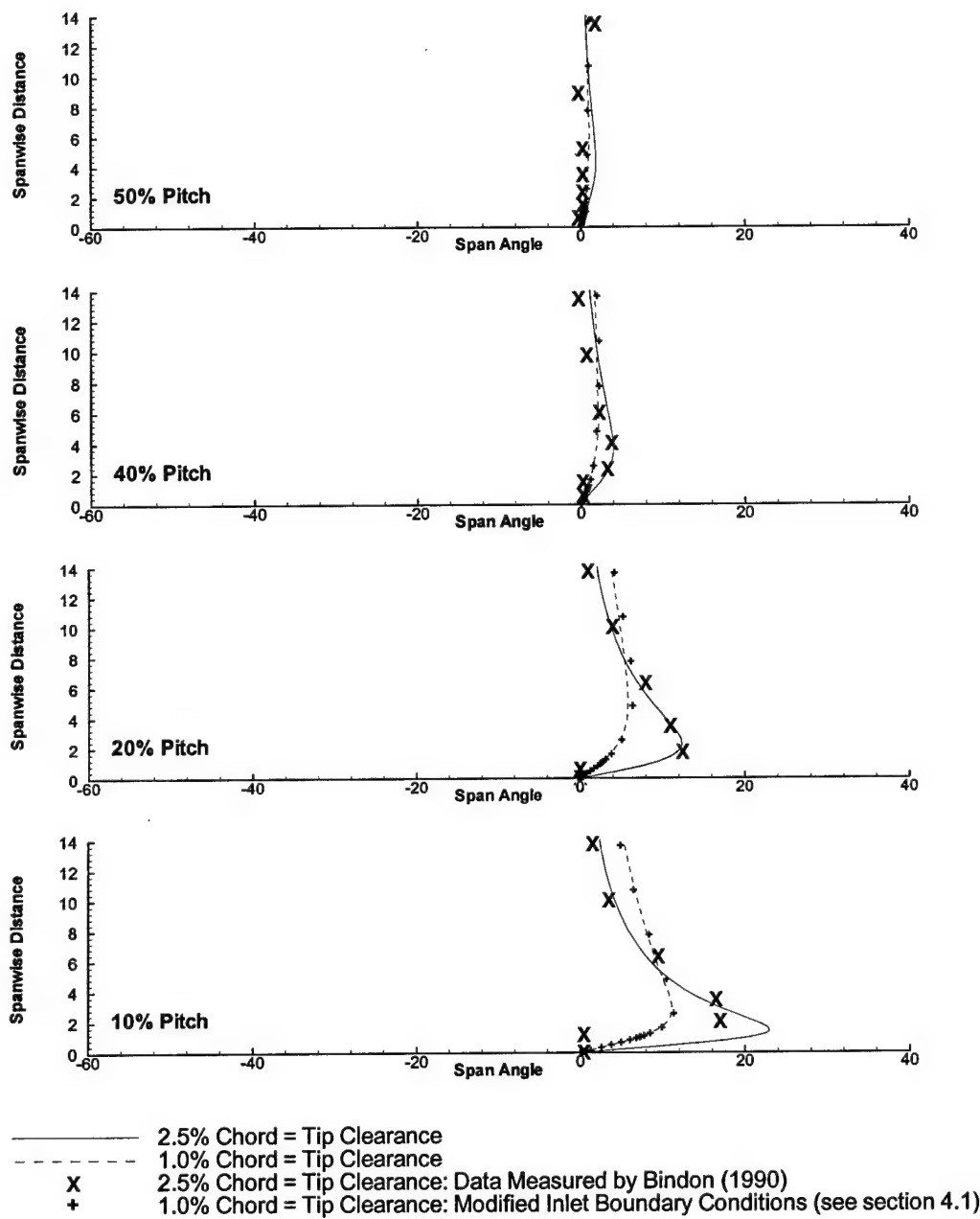


Figure 2.4: Span Angle near the Casing
Part (a): X = 60% Axial Chord



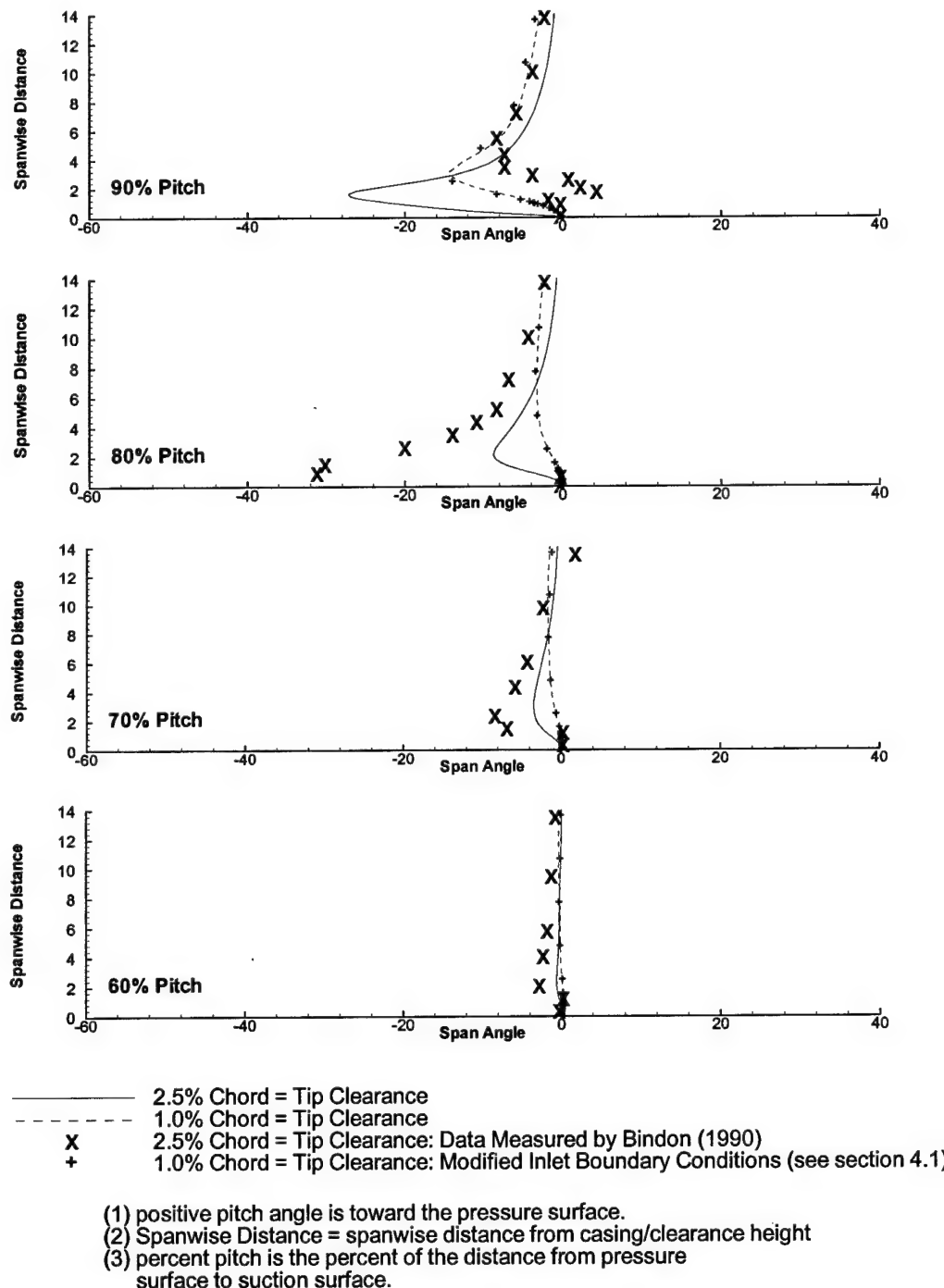
- (1) positive pitch angle is toward the pressure surface.
- (2) Spanwise Distance = spanwise distance from casing/clearance height
- (3) percent pitch is the percent of the distance from pressure surface to suction surface.

Figure 2.4 (continued): Span Angle near the Casing
Part (a): X = 60% Axial Chord



- (1) positive pitch angle is toward the pressure surface.
- (2) Spanwise Distance = spanwise distance from casing/clearance height
- (3) percent pitch is the percent of the distance from pressure surface to suction surface.

Figure 2.4: Span Angle near the Casing
Part (b): X = 80% Axial Chord



**Figure 2.4 (continued): Span Angle near the Casing
Part (b): X = 80% Axial Chord**

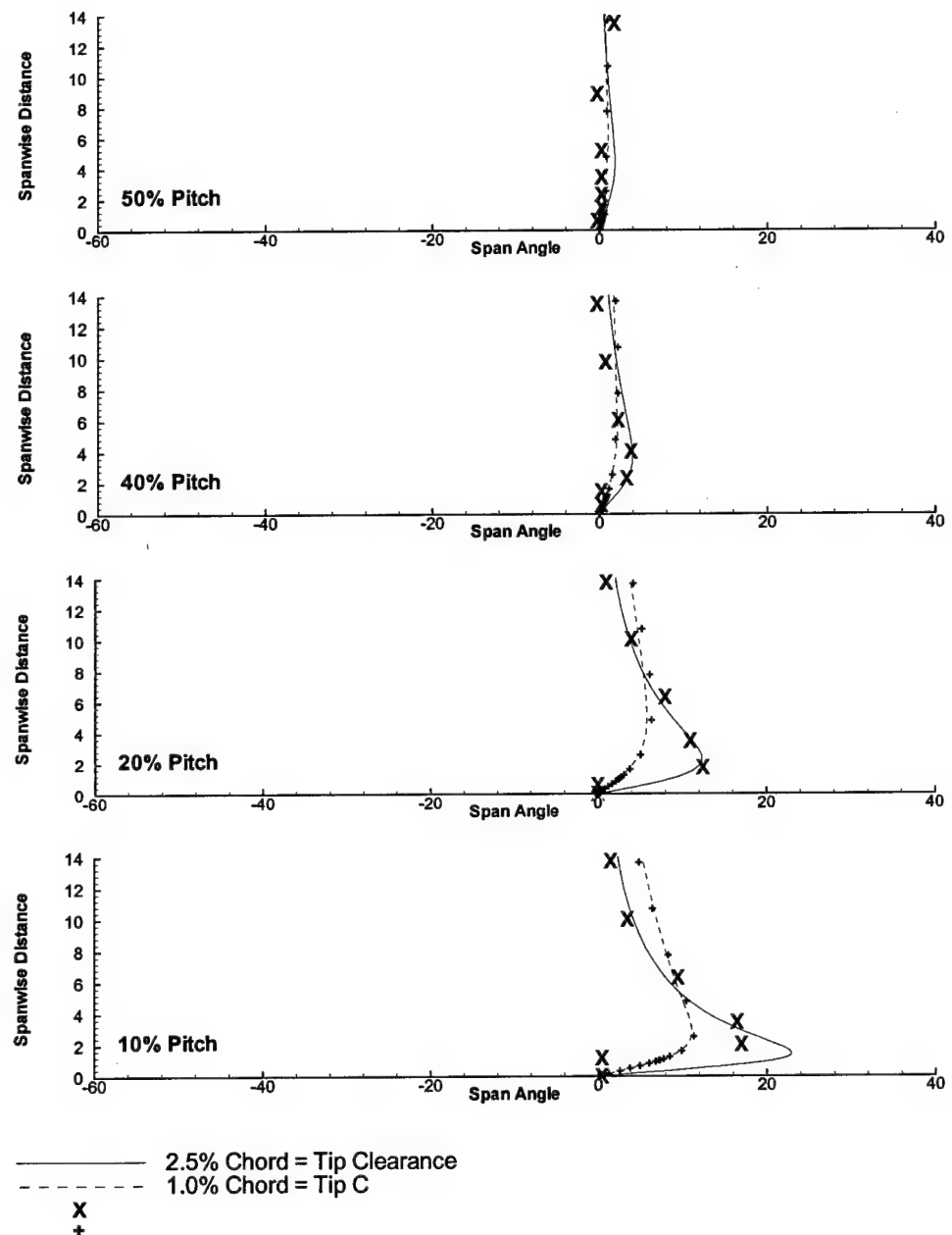
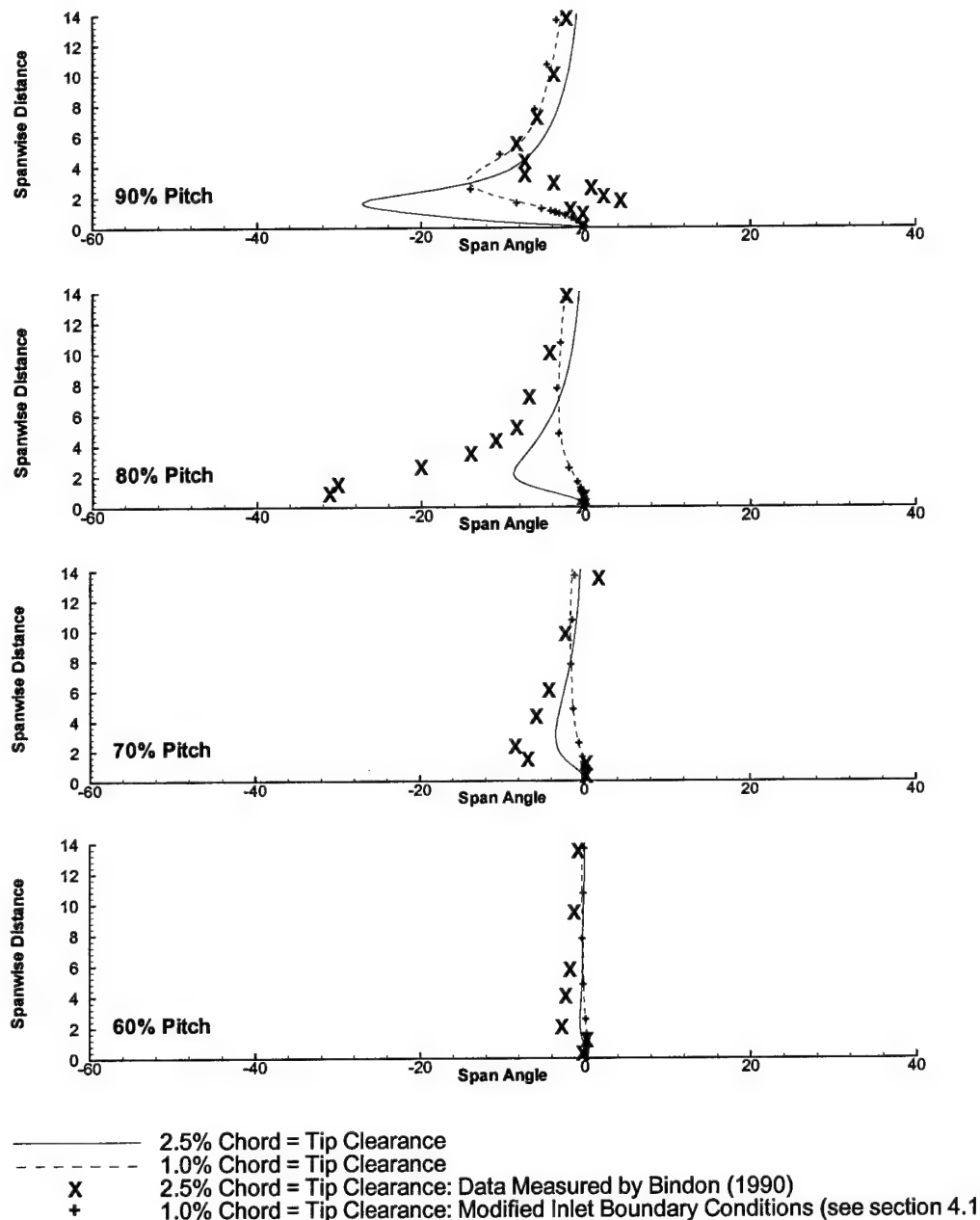


Figure 2.4: Span Angle near the Casing
Part (c): X = 90% Axial Chord



- (1) positive pitch angle is toward the pressure surface.
- (2) Spanwise Distance = spanwise distance from casing/clearance height
- (3) percent pitch is the percent of the distance from pressure surface to suction surface.

Figure 2.4 (continued): Span Angle near the Casing
Part (c): X = 90% Axial Chord

CHAPTER 3: RESULTS

A baseline flat tip case and the three modified tip cases described in chapter 1 were simulated using the numerical procedure outlined in chapter 2. In this chapter, the four computed flow fields are analyzed in detail and compared with one another.

As a means of qualitatively determining the effect of the modified blade tip geometries on the leakage vortex, particle traces through the gap and leakage vortex were produced. Figure 3.1 shows the leakage vortices for the baseline, leading edge chamfered, full chamfered and trailing edge chamfered cases. The colors in Fig. 3.1 are added to show similar regions of the flow field, but should not be considered to correspond exactly between the various parts of Fig. 3.1.

Figure 3.1(a) shows the leakage vortex for the baseline case, which is also pictured in Fig. 1.2. The leakage vortex develops along the suction side corner of the blade, beginning at about 40% axial chord. All of the fluid inside the leakage vortex passes through the gap region with very close proximity to the blade tip: roughly within 10% of the gap height. For comparison, the yellow fluid pathlines in Fig. 3.1(a) pass through the gap further removed from the blade tip, and thus, do not roll into the leakage vortex. As was discussed in the Background section, this indicates that the rotation of the leakage flow due to its shearing on the blade tip is the driving mechanism for the formation of the leakage vortex. The direction of this rotation is opposite of the blade's camber direction, and therefore negative.

The black fluid pathlines in Fig. 3.1(a) are slightly more puzzling. These pathlines also pass thorough the gap very near to the blade tip, yet indicate an opposite (positive) rotation once inside the passage. The same positive rotation region is shown in

Fig. 1.2 Lab. iv. In the precursor study to this one, Tallman and Lakshminarayana [10,11] discussed how the positive vorticity of the near-casing secondary flow (Fig. 1.2, Lab. v) is carried into the region below the leakage vortex, where it manifests itself as a mildly rotational region of the passage flow (Fig. 1.2, Lab. iv). To refer to this region as a “passage vortex” is incorrect, however, since the mechanisms responsible are entirely different and the rotation rate is considerably less than that of a true vortex, such as the leakage vortex. In comparing Figs. 1.2 and 3.1(a), it appears that the black fluid pathlines in Fig. 3.1(a) are being carried along with the near-casing secondary flow as it is scraped below the leakage vortex.

Figure 3.1(b) shows fluid pathlines that describe the flow for the leading edge chamfered case. The black and blue fluid pathlines illustrate the near-casing secondary flow. As was the design intention, this fluid is now carried into the gap’s leading edge region. Comparing Figs. 3.1(a) and 3.1(b) show that this does, indeed, act to turn the leakage flow more toward the camber direction. Unfortunately, the leakage flow has still found a way to roll-up. As has been discussed, the leakage flow in close proximity to the blade tip is responsible for causing the leakage vortex. Figure 3.1(b) shows that for the leading edge chamfer case, the red fluid pathlines, while turned more toward the camber direction, still travel towards the suction side edge of the blade underneath the obstructing near-casing secondary flow. Upon reaching the suction side edge, this fluid will still roll into a leakage vortex.

For the leading edge chamfer case, Fig. 3.1(b) shows that the spanwise location of the suction side blade edge will vary with location. The spanwise location of the suction

side blade edge decreases from the leading edge to about 40% axial chord, then rises dramatically back to its uniform downstream value. This dramatic rise leads to an enhancement of the leakage vortex, as Fig. 3.1(b) shows. The red fluid pathlines in Fig. 3.1(b) exit the gap region at successively increasing spanwise locations. Therefore, each subsequent red fluid pathline will wrap itself around the leakage vortex at an increasing radius, leading to the larger size of the leakage vortex. Alternatively, for the baseline case (Fig. 3.1(a)), the rolling up fluid pathlines tend to helix themselves around each other at a more constant radius. The larger leakage vortex for the leading edge chamfer case will lead to an increase in mixing and losses inside the passage.

A similar situation can be seen in Fig. 3.1(c) for the full chamfer case. Black and blue fluid pathlines indicate the obstructing near-casing secondary flow inside the gap, while red and yellow fluid pathlines show the leakage flow passing underneath. In the full chamfer case, the increase in spanwise location of the suction side edge is spread out more gradually across the entire length of the blade. Therefore, the “fluid stacking” effect seen in the leading edge chamfer case is less severe, but still present. Once again, the leakage vortex size and mixing is enhanced from that of the baseline case in Fig. 3.1(a).

The flow through the trailing edge chamfer case is shown in Fig. 3.1(d). Beyond 30% axial chord, the size of the leakage vortex is noticeably smaller for the trailing edge chamfer case. The reason for this size reduction of the leakage vortex can be seen in the red fluid pathlines of Fig. 3.1(d). These fluid pathlines are the ones that pass through the gap near to the blade tip and are responsible for causing the leakage vortex. Figure 3.1(d)

shows that from the start of the chamfered region to the blade trailing edge, the red fluid pathlines have been turned considerably towards the camber line's direction. The red fluid pathlines in Fig. 3.1(d) are still sheared across the tip of the blade and are, thus, still rotational. However, the direction of this rotation is no longer well aligned with the direction of the leakage vortex's rotation. Therefore, between 40% and 70% axial chord, the initial leakage vortex has a more difficult time starting out. Further downstream, however, the suction side edge of the blade is increasing in its spanwise location, as it did in the leading edge and full chamfer cases. Therefore, the leakage vortex increases in size through the final 30% of the passage.

Because only the trailing edge chamfer case shows a reduction in the leakage vortex, the remainder of this report will focus on comparison between the baseline and trailing edge chamfer cases. A comparison of the flow in the gap region for these two cases is given in Fig. 3.2. Once again, fluid pathlines are used to illustrate the flow qualitatively. Figure 3.2 clearly shows the turning of the leakage flow towards the camber direction that results from the blade tip modification. The red fluid pathlines in the trailing edge chamfer case (Fig. 3.2(b)) are at an angle of approximately 45 degrees from the camber direction, while in the baseline case (Fig. 3.2(a)), they are almost normal to the camber direction. In the upstream half of the gap, however, the two leakage flows are very similar. The turning of the leakage flow near the blade tip in the trailing edge chamfer case is of great significance in attempts to reduce the leakage vortex, since a leakage flow aligned with the camber direction cannot cause a leakage vortex. Also, the red and yellow fluid pathlines in Fig. 3.2(a) show that the leakage flow in the trailing

edge chamfer case is highly three-dimensional. The yellow fluid pathlines in Fig. 3.2(b) are only slightly further removed from the blade tip than the red fluid pathlines.

In both parts of Fig. 3.2, the black fluid pathlines illustrate the near-casing secondary flow. These fluid pathlines are released from the same starting point for both the baseline case and the trailing edge chamfer case. In the baseline case, some near-casing secondary flow enters the gap region near the leading edge of the blade, but this fluid is forced back out of the gap by the leakage flow only slightly further downstream from where it entered. In the trailing edge chamfer case, Fig. 3.2(b) shows that the near-casing secondary flow entering the gap near the leading edge is able to continue inside the gap longer, with a direction more similar to the blade's camber. This is due to the increased flow area available in the downstream half of the gap. In addition, near-casing secondary flow is able to enter the gap region further downstream in the trailing edge chamfer case than in the baseline case.

The increased quantity of near-casing secondary flow and increased longevity of said flow inside the gap region are responsible for the turning of the leakage flow toward the camber direction. The near-casing secondary flow that enters the gap acts as an obstruction to the leakage flow. The leakage flow then has two ways that it can circumnavigate the obstruction. First, the leakage flow can force its way underneath the obstruction, such as what is seen in the leading edge region of Fig. 3.2(b). Second, the leakage flow can turn toward the camber direction and pass around the obstruction further downstream. Figure 3.2(b) indicates that the leakage flow utilizes both of these options in the trailing edge chamfer case. The turning of the yellow and red leakage flow

pathlines indicates the latter option, while the crossing of the black and yellow fluid pathlines indicates the former.

Figure 3.3 shows both the velocity and pressure field in the blade-to-blade plane at a spanwise location of 100.2% of the blade height. This location is 20% of the distance from the top of the blade to the outer casing. Once again, a direct comparison between the baseline and trailing edge chamfer cases is made. Pressure is displayed as pressure coefficient (C_p) contours, where the pressure coefficient is defined as the difference between the local and inlet static pressure values, non-dimensionalized by the inlet dynamic pressure. A line has been added to Fig. 3.3(b) to indicate the location where the trailing edge chamfering begins. The same line has been added to Fig. 3.3(a) as a reference.

For the baseline case, Fig. 3.3(a) shows that the velocity and pressure fields inside the gap are well aligned with each other. Velocity vectors point in a direction of decreasing pressure, and that direction is fairly uniform throughout the gap region. The leakage flow exits the gap in a direction fairly normal to the suction surface of the blade. Therefore, the vorticity of the leakage flow near the blade tip will be similar to the direction of the leakage vortex's rotation. For the trailing edge chamfer case, Fig. 3.3(b) shows velocity vectors from the leakage flow and near-casing secondary flow turning on each other at the suction side of the gap. The leakage flow velocity vectors turn toward the camber direction, as was seen in Figs. 3.1(d) and 3.2(b). Caution should be taken when following the velocity vectors through the gap in Fig. 3.3(b), however, since Figs. 3.1(d) and 3.2(b) showed an important spanwise component to the flow.

The original reasoning behind the trailing edge chamfer design was that the increased area made available to the leakage flow would act to diffuse the flow and reduce the leakage velocity. The fluid pathlines in Figs. 3.1(d) and 3.2(b), however, indicate that the flow inside the chamfered gap is considerably more complex than that through a simple 1D diffuser. A pressure rise in the direction of the leakage flow is seen in the trailing edge region of Fig. 3.3(b), which would indicate that the leakage flow is being decelerated. Comparison with Fig. 3.3(a) indicates that the leakage flow is indeed losing momentum in the direction corresponding to the leakage flow in the baseline case. The leakage flow does not decelerate, however, and instead turns toward the trailing edge, where lower pressure values exist. Therefore, the turning of the leakage flow toward the camber direction in the trailing edge chamfer case is due to two mechanisms: 1) the obstruction of the leakage flow by the near-casing secondary flow and 2) the pressure rise across the chamfered gap due to its diffusing effect. With these two mechanisms, the pressure rise in the latter mechanism may be entirely due to the former mechanism and not a diffuser effect at all. Throughout Fig. 3.3(b), the velocity and pressure fields appear to be well coupled together. That is, velocity vectors tend in direction toward lower C_p values.

The difference in the direction of the red and yellow fluid pathlines of Fig. 3.2(b) can also be explained by considering the pressure field inside the gap. Figures similar to Fig. 3.3(b) (not shown) indicate that the pressure distribution in the blade-to-blade plane does not change significantly inside the gap with spanwise location. Therefore, the increased turning of the red fluid pathlines in Fig. 3.2(b) is similar to a passage vortex

effect. The flow in the gap establishes a pressure gradient to support the turning of the leakage flow toward the camber direction. At locations closer to the blade tip, the fluid is slower moving and, thus, requires less centripetal acceleration than the pressure gradient is providing. Therefore, the fluid is overturned, just as a boundary layer in a curved duct becomes overturned. This overturning of the leakage flow near the blade tip is beneficial, since this fluid is exactly the fluid that forms the leakage vortex.

Figure 3.4 is similar to Fig. 3.3, only at a spanwise location of 98% blade span. The darkest blue contour indicates the core of the leakage vortex in both parts. This core is noticeably smaller in the trailing edge chamfer case. Furthermore, the beginning of the core has moved toward the trailing edge of the blade with the trailing edge chamfer case. The inception of the leakage vortex has been delayed with the modified blade tip. Immediately adjacent to the leakage vortex core, the trailing edge chamfer case shows reduced pressure values, which closer resemble the pressure contours at the blade's mid-span location (not shown). This indicates improved turbine performance near the tip for the trailing edge chamfer case. Upstream and throughout the remainder of the passage, the flow fields are similar for the two cases.

Figures 3.5 through 3.8 and Fig. 3.10 show secondary vorticity contours in the tangential-spanwise plane near the leakage vortex at various axial locations. Vorticity shown is in the 2D-streamwise direction, and is non-dimensionalized using the blade span and inlet velocity. Figure 3.5 is situated at 60% axial chord. Both parts of Fig. 3.5 indicate that vorticity is being convected out of the gap region, with negative vorticity coming from near the tip and positive vorticity coming from near the outer casing. The

negative vorticity region inside the gap is noticeably larger in the trailing edge chamfer case. This is related to the three dimensionality of the leakage flow in the downstream half of the trailing edge chamfer case, illustrated by the yellow and red fluid pathlines in Fig. 3.2(b). These pathlines show that tangential velocity decreases with proximity to the blade tip, resulting in the increased levels of negative vorticity inside the gap for the trailing edge chamfer case.

In Fig. 3.5, the region of negative vorticity is associated with the flow in and around the leakage vortex in both cases. Above and to the right of this region is a complicated region of positive vorticity, associated with the near-casing secondary flow. Above the leakage vortex, the region of greatest positive vorticity is associated with the turning of the near-casing secondary flow away from the gap. This turning was illustrated by the black fluid pathlines in Fig. 3.2. With the trailing edge chamfer case, the turning of the near-casing secondary flow takes place closer to the gap, where it further inhibits the leakage flow. The region of slightly less positive vorticity to the right of the leakage vortex is composed of near-casing secondary flow and leakage flow from near the casing that have exited the suction side of the gap further upstream. Because of the casing's relative motion, both of these types of fluid will be positively rotational, and that rotation later appears inside the passage as the region aforementioned.

Figures 3.6 through 3.8 are identical to Fig. 3.5, only at axial locations of 70%, 80%, and 90% axial chord, respectively. All of the trends discussed in Fig. 3.5 are also present in Figs. 3.6 through 3.8. Together, the four figures illustrate the development of the secondary flow field in the downstream half of the passage. The four figures show

that the growth of the region of negative vorticity associated with the leakage vortex is less severe in the trailing edge chamfer case. By 90% axial chord, the size of this region in the trailing edge chamfer case is approximately half of its value in the baseline case. This agrees with the illustrations of the leakage vortex that were shown in Figs. 3.1 and 3.2. Additionally, the region of positive vorticity below and to the right of the leakage vortex shows reduced values for the trailing edge case in all of Figs. 3.5 through 3.8, indicating improved flow performance inside the passage.

Secondary velocity vectors are shown along with the vorticity contours in Fig. 3.8. At first glance, the velocity vectors inside the gap appear reduced in velocity magnitude for the trailing edge case. However, care must be taken in analyzing 2D velocity vectors, as a third component is neglected. Instead, close analysis of Fig. 3.2(b) indicates that the flow inside the gap is not decelerated, but rather turned toward the camber direction. This turning was seen in Figs. 3.1 and 3.2. Leakage vortex roll-up is much more clearly observable in the velocity vectors for the baseline case. The baseline case in Fig. 3.8 shows a stronger flow toward the outer casing on the left side of the leakage vortex. The shearing of this secondary flow by the blade's suction surface results in the region of positive vorticity to the left of the leakage vortex. The shearing results in increased profile losses and is, thus, undesirable. This secondary flow is considerably reduced for the trailing edge chamfer case. Therefore, the trailing edge chamfer case once again shows improved performance over the baseline case. Additionally, Fig. 3.9 shows the actual secondary vorticity values inside the leakage vortex of Fig. 3.8. Figure

3.9 shows quantitatively that the secondary vorticity magnitude at the core of the vortex has reduced for the trailing edge chamfer case.

Figure 3.10 shows one final plot of the vorticity field: this time downstream of the trailing edge at 110% axial chord. This figure clearly indicates that the effect of the trailing edge chamfer is to reduce the strength of the leakage vortex. Downstream of the passage, the contours of negative vorticity associated with the leakage vortex are reduced in both size and magnitude with the trailing edge chamfer case. This will result in reduced downstream losses associated with the decay of the leakage vortex, as well as reduced relative unsteadiness in subsequent blade rows. Additionally, the reduction of the leakage vortex's vorticity seen in Fig. 3.10 could be partially due to increased turbulence production inside the gap, although analysis of the turbulence field could not confirm or deny this possibility. Figure 3.11 shows the secondary vorticity values inside the center of the leakage vortices of Fig. 3.10. Figure 3.11 once again shows that the size and strength of the leakage vortex is reduced with trailing edge chamfering.

Figures 3.12 and 3.13 show contours of total pressure in the tangential-spanwise plane. In these two figures, total pressure is normalized by the inlet passage-averaged total pressure plus an additional work component. The work component is the additional total pressure made available to the flow via the work done on the flow by the relatively moving outer casing. This work term increases with axial location, but does not exceed more than 3% of the inlet total pressure.

Figure 3.12 shows total pressure contours at 90% axial chord. Initially, Fig. 3.12 appears to contradict the findings presented earlier. The region of lowest total pressure is

situated around the leakage vortex. This region is larger in the trailing edge chamfer case, despite the case's smaller leakage vortex. To explain this feature, the total pressure throughout the flow needs to be analyzed in greater detail. Figure 3.12 shows higher losses inside the gap for the trailing edge chamfer case. A closer analysis of the total pressure field shows that this trend is consistent throughout the chamfered region of the gap. Figures showing this trend are not presented, but evidence of the trend is present in Fig. 3.2. In Fig. 3.2(b), the red and yellow fluid pathlines exhibit shearing across one another, which will lead to viscous dissipation of energy and losses. The largest total loss contours in Fig. 3.12 are therefore not associated entirely with the leakage vortex, but with the leakage vortex and the high loss fluid convected out of the gap along pathlines such as the yellow ones in Fig. 3.1(d). Figure 3.12 shows that the losses away from the leakage vortex, associated with the blade's boundary layer, are comparable for the two cases. Therefore, at 90% axial chord, the trailing edge chamfer case does not show an improvement in losses, despite the smaller leakage vortex. Additionally, Fig. 3.13 shows total pressure values inside the leakage vortices shown in Fig. 3.12. For the trailing edge chamfer case, Fig. 3.13 shows decreased losses associated with the core of the leakage vortex and increased losses in the region adjacent to the leakage vortex.

Figure 3.14 shows total pressure contours at 110% axial chord. In both cases, the contour of lowest total pressure is associated directly with the decaying leakage vortex, as the leakage flow is no longer present downstream of the blade. The losses associated with the decaying leakage vortex are smaller in the trailing edge chamfer case, as the blue contours show. While the region of reduced total pressure in Fig. 3.14 occupies a

similarly sized area for both cases, total pressure values appear slightly higher in the trailing edge chamfer case. This agrees with the reduced overall secondary flow activity in the trailing edge chamfer case, which was observed in previous figures. In the trailing edge chamfer case, increased losses have taken place inside the gap further upstream, and the resulting reduced total pressure values are more evenly spread out at 110% axial chord. In the baseline case, losses are being produced at 110% axial chord to a greater extent, due to the more prevalent leakage vortex and surrounding secondary flows. Figure 3.15 shows the total pressure values inside the leakage vortices in Fig. 3.14. For the trailing edge chamfer case, losses are again reduced inside the leakage vortex core and increased in the region surrounding the leakage vortex.

Figure 3.16 shows the passage-averaged loss coefficient values versus axial location for the four cases shown in Fig. 3.1. The passage-averaged loss coefficient is defined as the difference between the inlet and local total pressure values, mass averaged over the tangential-spanwise plane. This total pressure difference is then non-dimensionalized by the inlet dynamic pressure. Please also note that the value of the inlet total pressure is increased slightly with axial location, in order to account for the work done on the fluid by the moving outer casing in the relative frame of reference.

The leading edge chamfer and full chamfer cases exhibit higher losses throughout the blade row. This is to be expected, as both cases showed a larger leakage vortex than the baseline case. For the baseline and trailing edge chamfer cases, the loss coefficient values inside the blade row are of negligible difference. A difference in loss coefficient of 0.01 corresponds to a difference in passage averaged total pressure of about 1 pascal,

which is less than the numerical accuracy of the solution and passage-averaging integration. Therefore, it appears that with the trailing edge chamfer modification, the increase in losses inside the gap region offset the decrease in losses due to decreased secondary flow activity inside the passage.

Downstream of the blade, the trailing edge chamfer case exhibits lower losses than the baseline case. The decrease in losses is due to the smaller size of the leakage vortex. Losses associated with the tip leakage vortex are due to the mixing of the leakage vortex and viscous dissipation. Downstream of the blade row, the leakage vortex is no longer being supplied with energy from the leakage flow and will eventually decay away. The smaller vortex in the trailing edge chamfer case decays more rapidly and with less integrated loss of energy than the larger leakage vortex in the baseline case.

The full chamfer case also exhibits reduced passage-averaged losses downstream of the blade row, although the difference in loss coefficient values between the full chamfer and trailing edge chamfer cases is once again smaller than the numerical accuracy of the calculating procedure. The full chamfer case should show increased losses downstream of the blade row due to the increased size of the leakage vortex. Therefore, the reduction in downstream losses for the full chamfer case is likely due to a reduction in the losses away from the leakage vortex. A comparison of the black fluid pathlines in Figs. 3.1(a) and 3.1(c) supports this conclusion, as there is less fluid rotation exhibited in these pathlines for the full chamfer case. Still, passage-averaged losses are not the only criteria for judging the performance of the blade. A smaller leakage vortex will result in less unsteadiness within a subsequent downstream stator. This will lead to a

reduction in unsteady blade loading and noise downstream. Therefore, the trailing edge chamfer case is still advantageous over the full chamfer case.

One further criterion for judging turbine blade performance is the loading on the blade. By reducing the turning of the blade to zero at the tip, the leakage vortex is eliminated, but so is the work being done on the blade by the flow. Therefore, caution has to be taken with techniques that reduce the leakage vortex.

Figure 3.17 shows contours of static pressure coefficient on the blade surface for the two cases. Static pressure coefficient (C_p) was defined earlier in the text, in reference to Figs. 3.3 and 3.4. While the pressure surface of the blade is not shown in Fig. 3.17, the pressure distribution on that surface is almost identical for the two cases. The C_p distribution on the blade tip is very similar to the C_p distribution inside the gap in Fig. 3.3, indicating that pressure does not change dramatically in the spanwise direction within the gap. The contour of lowest C_p values situated along the suction side/blade tip corner is associated with the leakage vortex in both cases. This contour is smaller in size and delayed in its origin, agreeing with the illustrations of the two leakage vortices in Fig. 3.1. Away from the leakage vortex, the C_p distribution on the suction surface is similar for the two cases, indicating similar blade loading.

Figure 3.18 shows the C_p distribution on the blade at the tip for the baseline and trailing edge chamfer case. Additionally, the mid-span C_p distribution is also shown. Before 30% axial chord, the two blade tip C_p distributions are very similar. This is expected, since chamfering does not begin until further downstream. On the suction side of the blade, the C_p distribution for the trailing edge chamfer case closer resembles the

distribution at the mid-span. The sudden jump in the trailing edge chamfer case's C_p distribution on the suction surface at 45% axial chord is associated with the start of the blade chamfer. The minimum C_p value on the suction surface blade tip is of similar value for the two cases. On the pressure surface, C_p values are reduced from the mid-span values for both cases, indicating the unloading of the blade tip from the entrainment of the leakage flow into the gap. With the trailing edge chamfering, this unloading increases slightly (reduced C_p) through the upstream 50% axial chord and decreases slightly (increased C_p) through the downstream 50% axial chord. In general, the pressure drop across the blade tip is smaller in the trailing edge chamfer case.

The integrated forces acting on the blade are shown in Table 3.1 for the four cases being considered. Force values are reported as the ratio of a particular case's value to the baseline case's value, as well as a percent change from the baseline case. The tangential force component provides torque to the rotor and, thus, power output from the turbine. The power supplied to the turbine blade is simply the blade loading in the tangential direction times the blade's velocity (31.0 m/s in this case). This means that the percentage change in blade loading is equivalent to the percentage change in power to the blade. The tangential blade loading for the trailing edge chamfer case is reduced from the baseline case by 1.03%. While this number is quite small, the additive effect over multiple blades in a rotor could be non-negligible. The axial component of the blade loading is primarily due to the pressure drop through the turbine and does not contribute to the torque applied to the turbine's axis. For the trailing edge chamfer case, this component is reduced by 1.71% from the baseline case's value. Depending on the

design, a small cost in blade loading may be an acceptable trade-off for improved noise, unsteadiness, durability, and downstream performance that comes with a reduced leakage vortex.

Table 3.1: Blade Loading Force Values

Total Force / Baseline Total Force	Baseline Case	Leading Edge Chamfer Case	Full Chamfer Case	Trailing Edge Chamfer Case
Tangential Component	1.0 (10.8798 N)	1.0003 (0.03%)	0.9807 (-1.93%)	0.9897 (-1.03%)
Axial Component	1.0 (12.6225 N)	0.9985 (-0.15%)	0.9725 (-2.75%)	0.9829 (-1.71%)

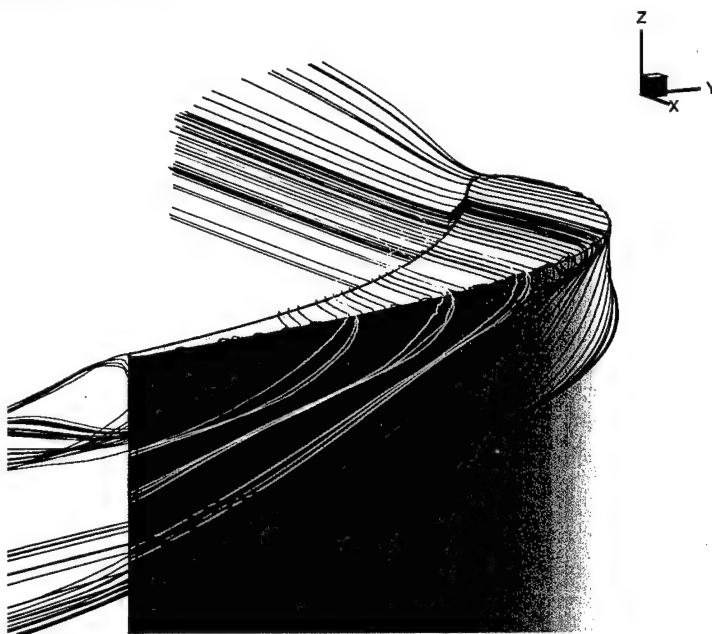
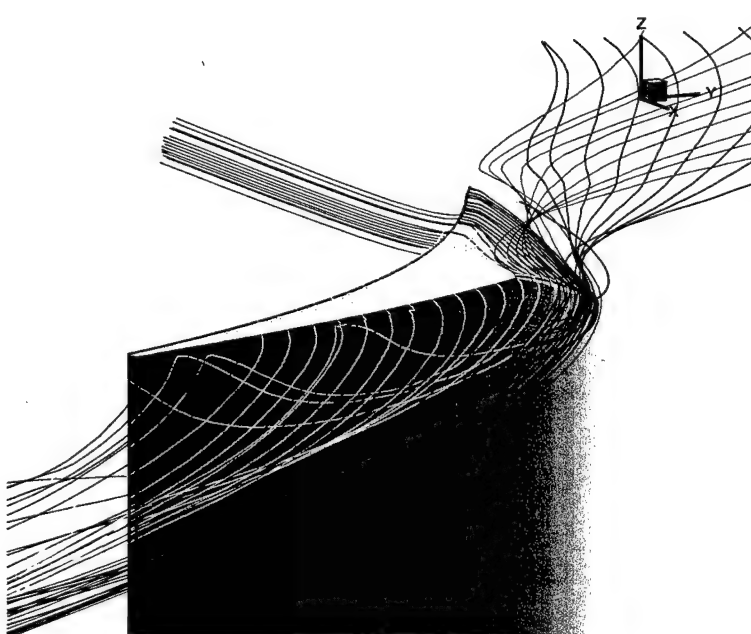
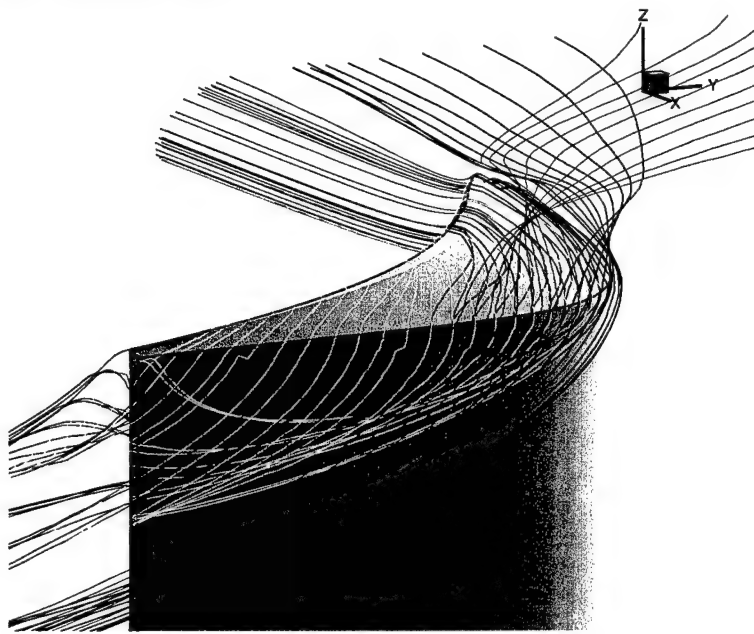
Part (a): Baseline Case**Part (b): Leading Edge Chamfer Case**

Figure 3.1: Leakage Vortices for Various Tip Geometry

Part (c): Full Chamfer Case



Part (d): Trailing Edge Chamfer Case

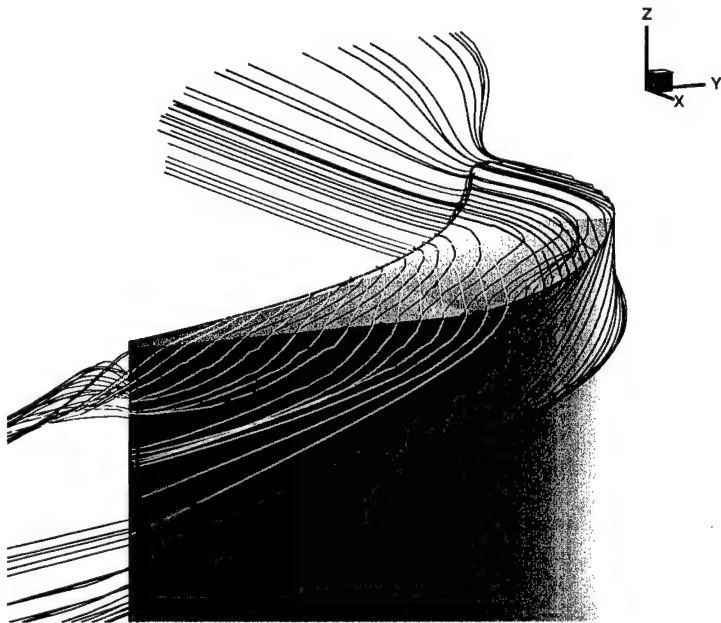
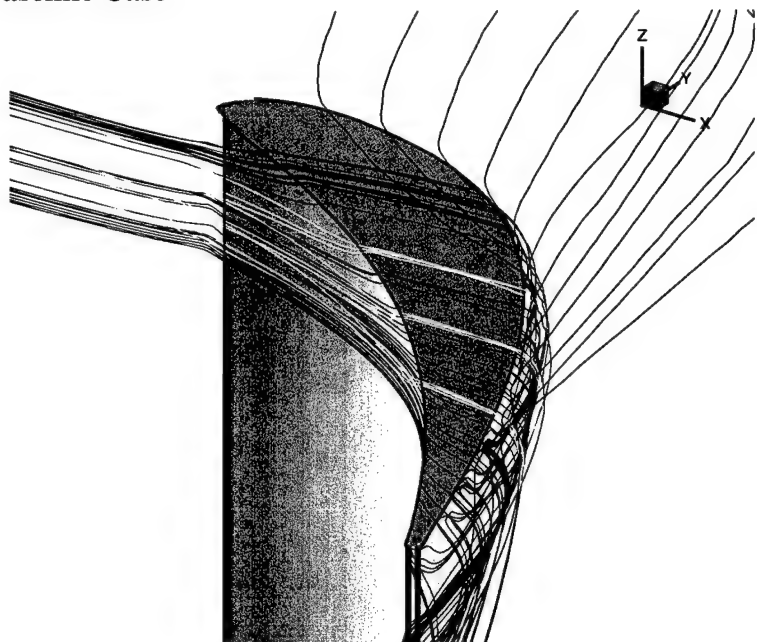


Figure 3.1 (continued): Leakage Vortices for Various Tip Geometry

Part (a): Baseline Case



Part (b): Trailing Edge Chamfer Case

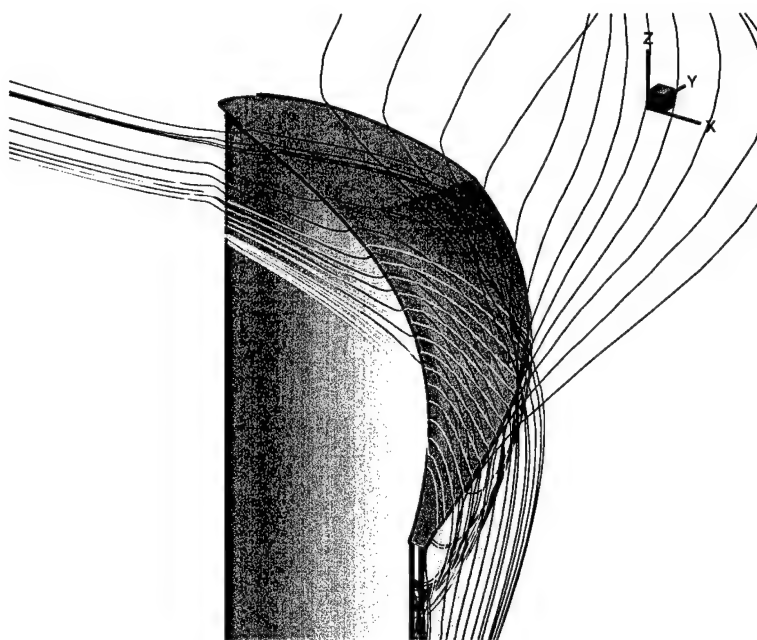


Figure 3.2: Leakage Flow and Vortex Comparison

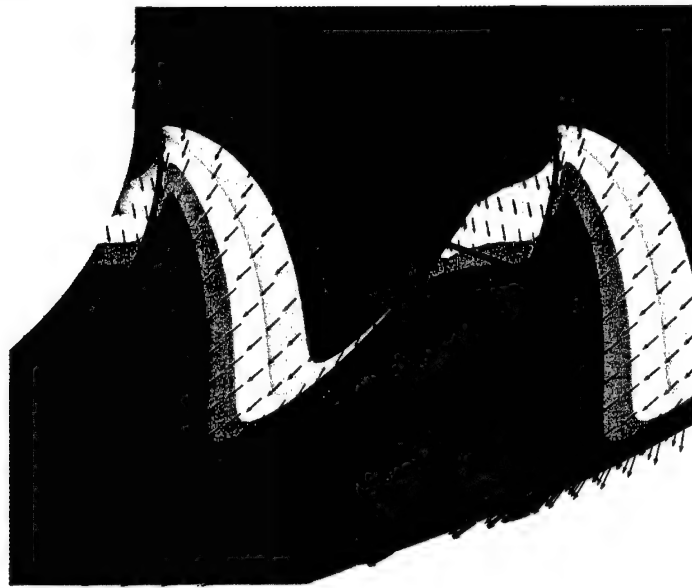
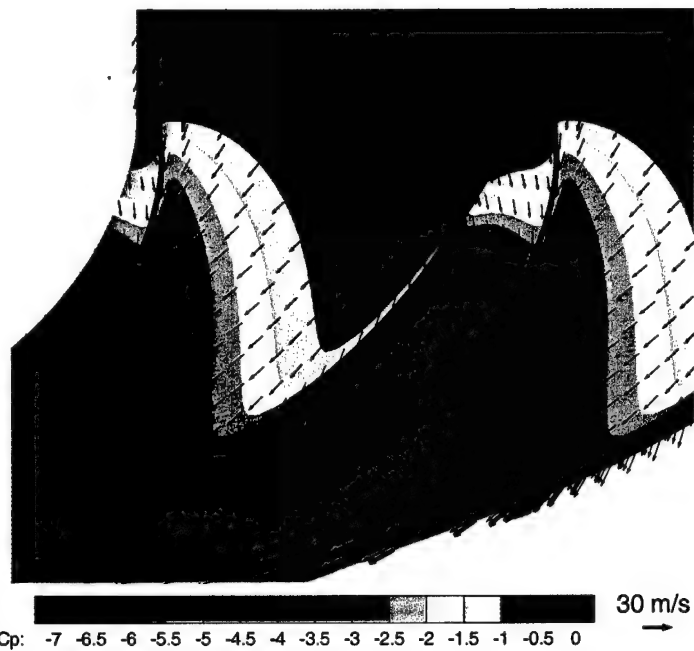
Part (a): Baseline Case**Part (b): Trailing Edge Chamfer Case**

Figure 3.3: Velocity and Pressure in the Blade-to-Blade Plane at 1.002% Span

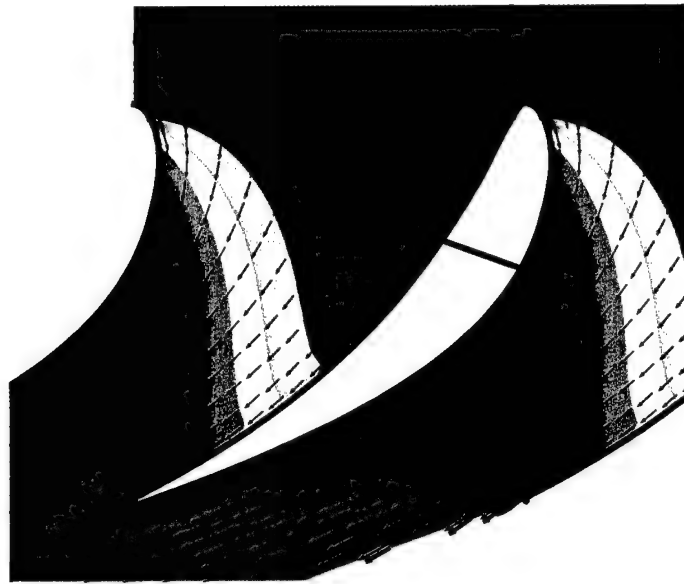
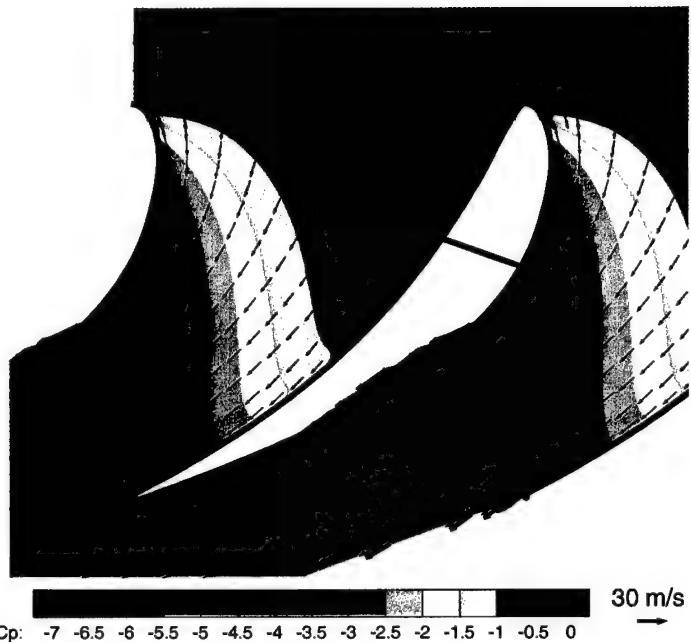
Part (a): Baseline Case**Part (b): Trailing Edge Chamfer Case**

Figure 3.4: Velocity and Pressure in the Blade-to-Blade Plane at 96% Span

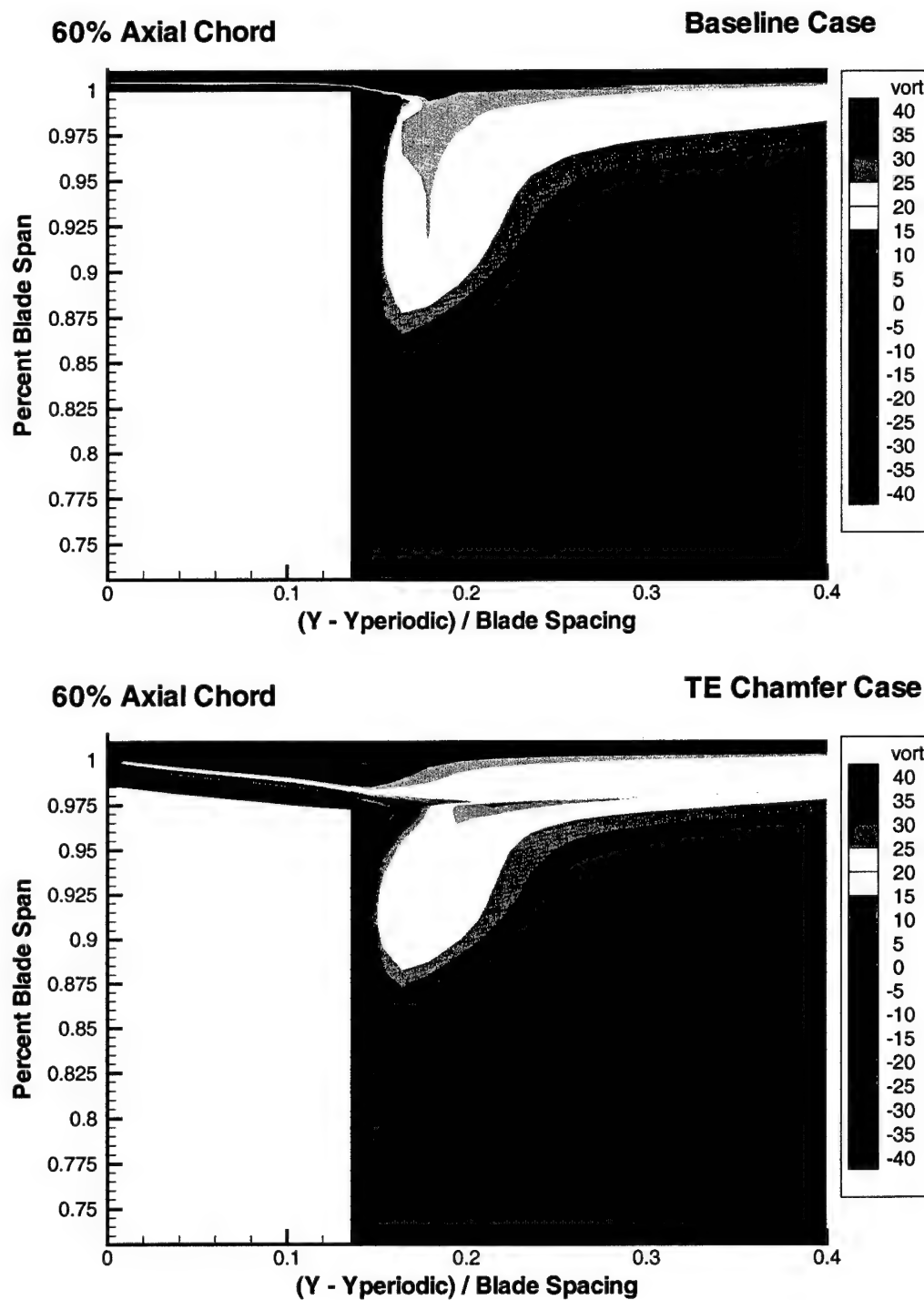


Figure 3.5: Non-Dimensional Streamwise Vorticity Contours at 60% Axial Chord

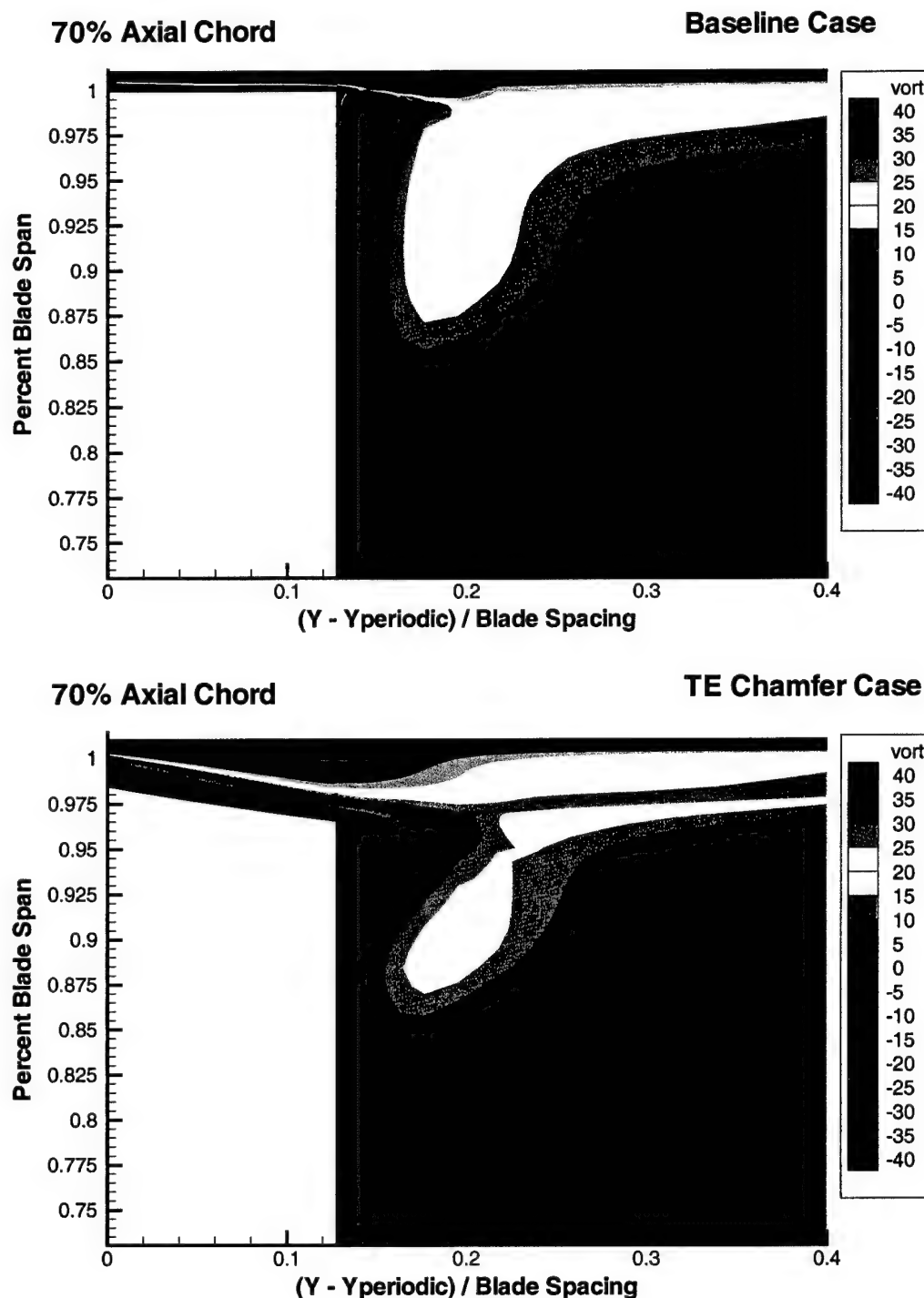


Figure 3.6: Non-Dimensional Streamwise Vorticity Contours at 70% Axial Chord

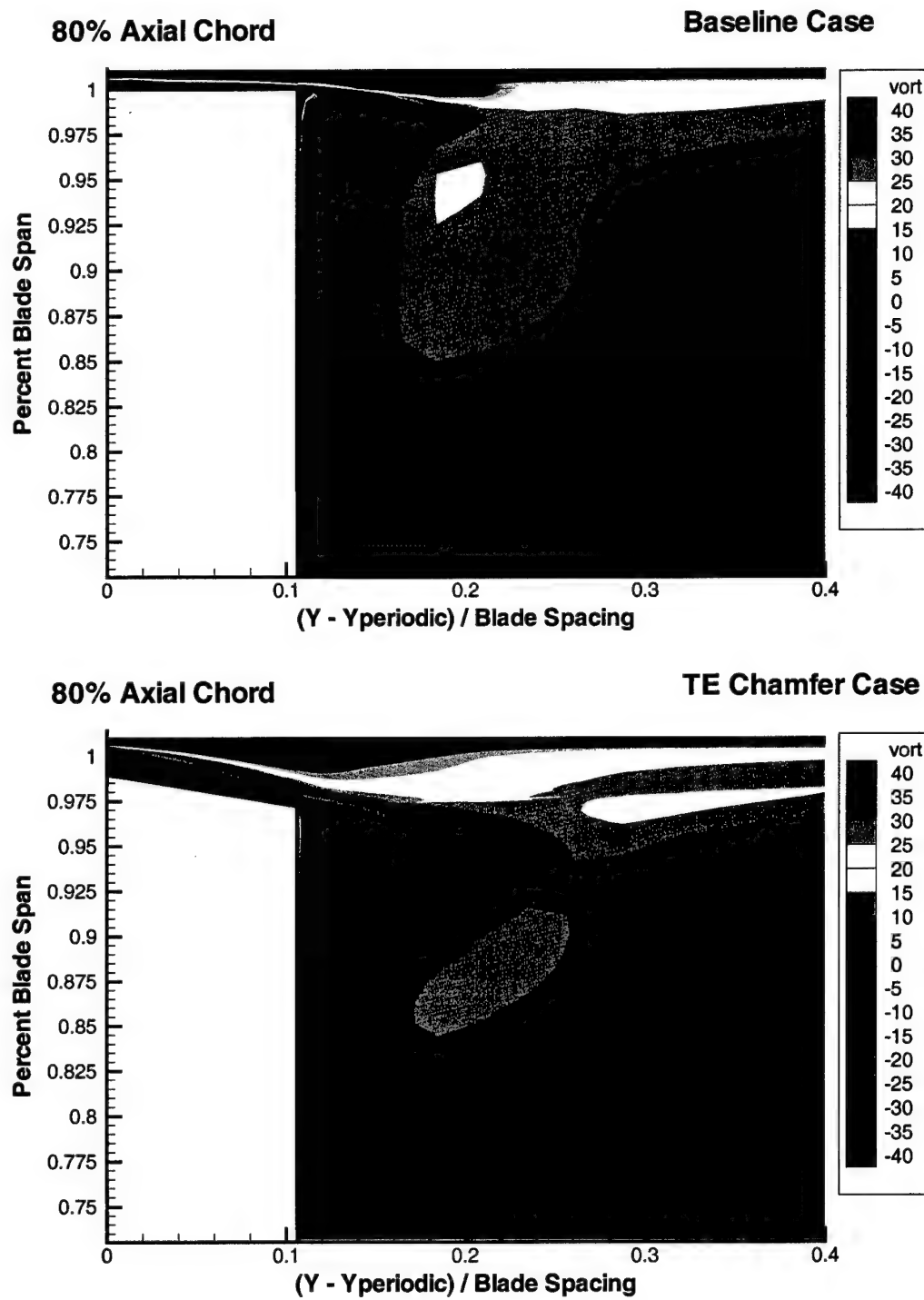


Figure 3.7: Non-Dimensional Streamwise Vorticity Contours at 80% Axial Chord

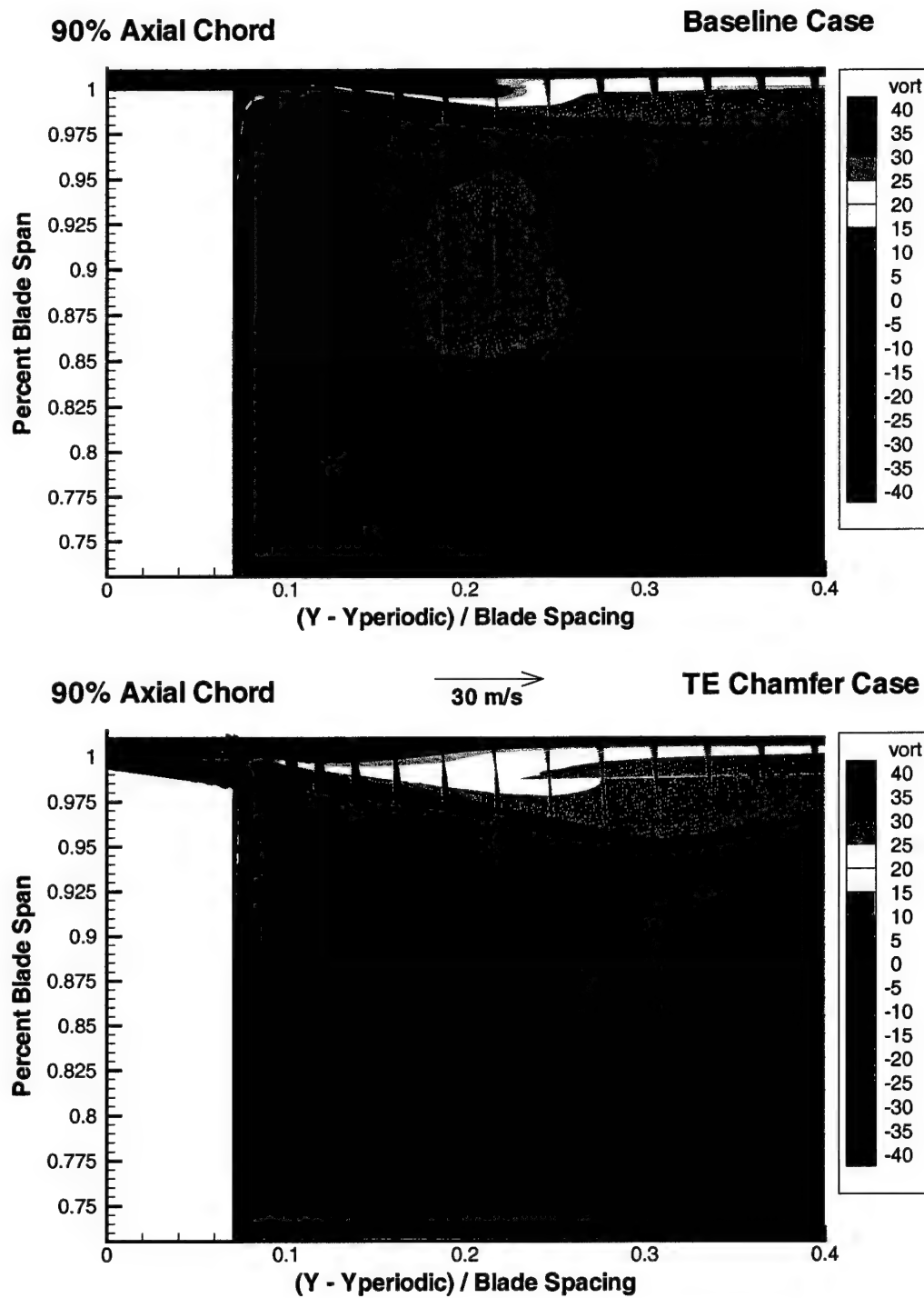


Figure 3.8: Non-Dimensional Streamwise Vorticity Contours at 90% Axial Chord

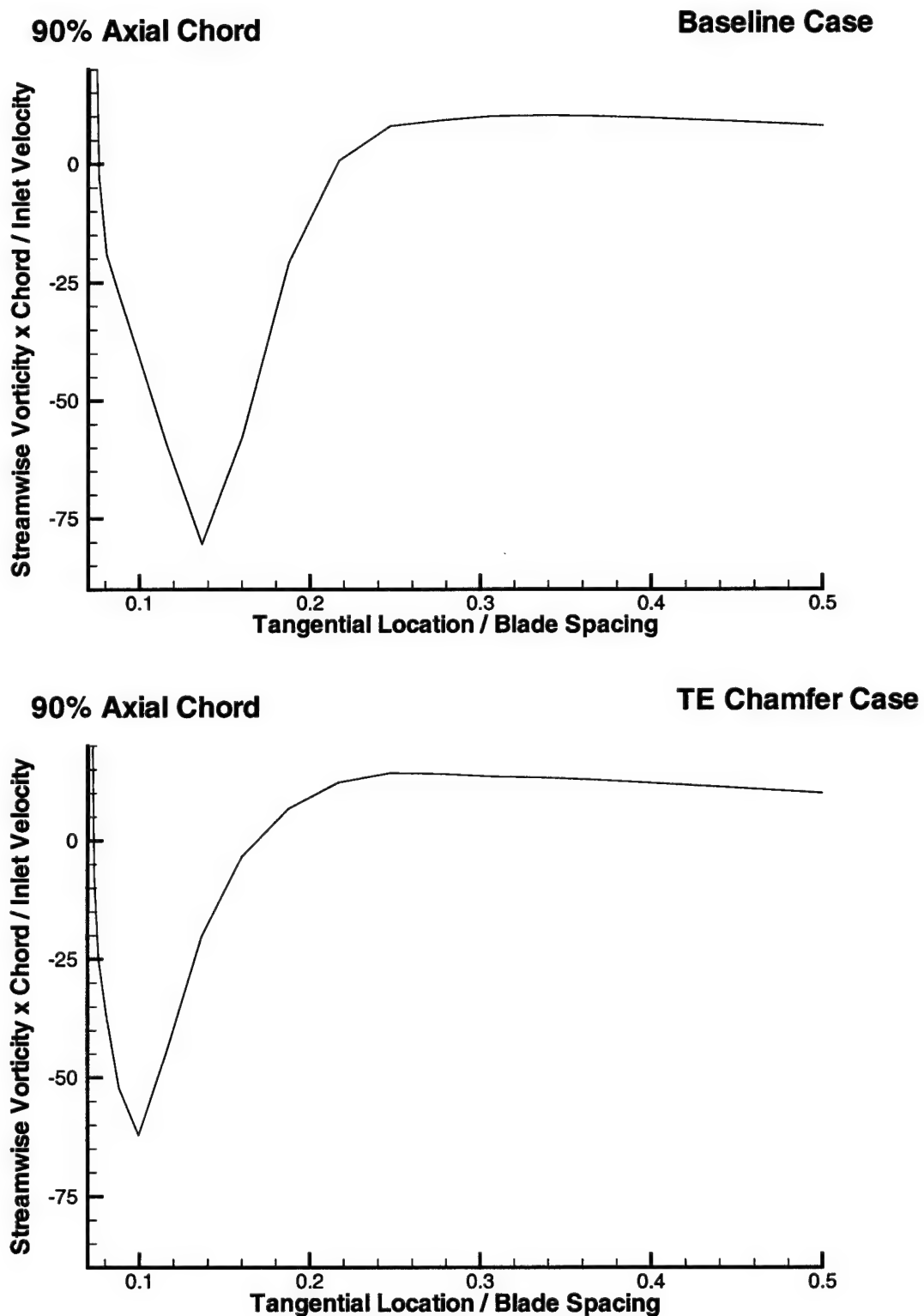


Figure 3.9: Streamwise Vorticity Inside the Leakage Vortex at 90% Axial Chord

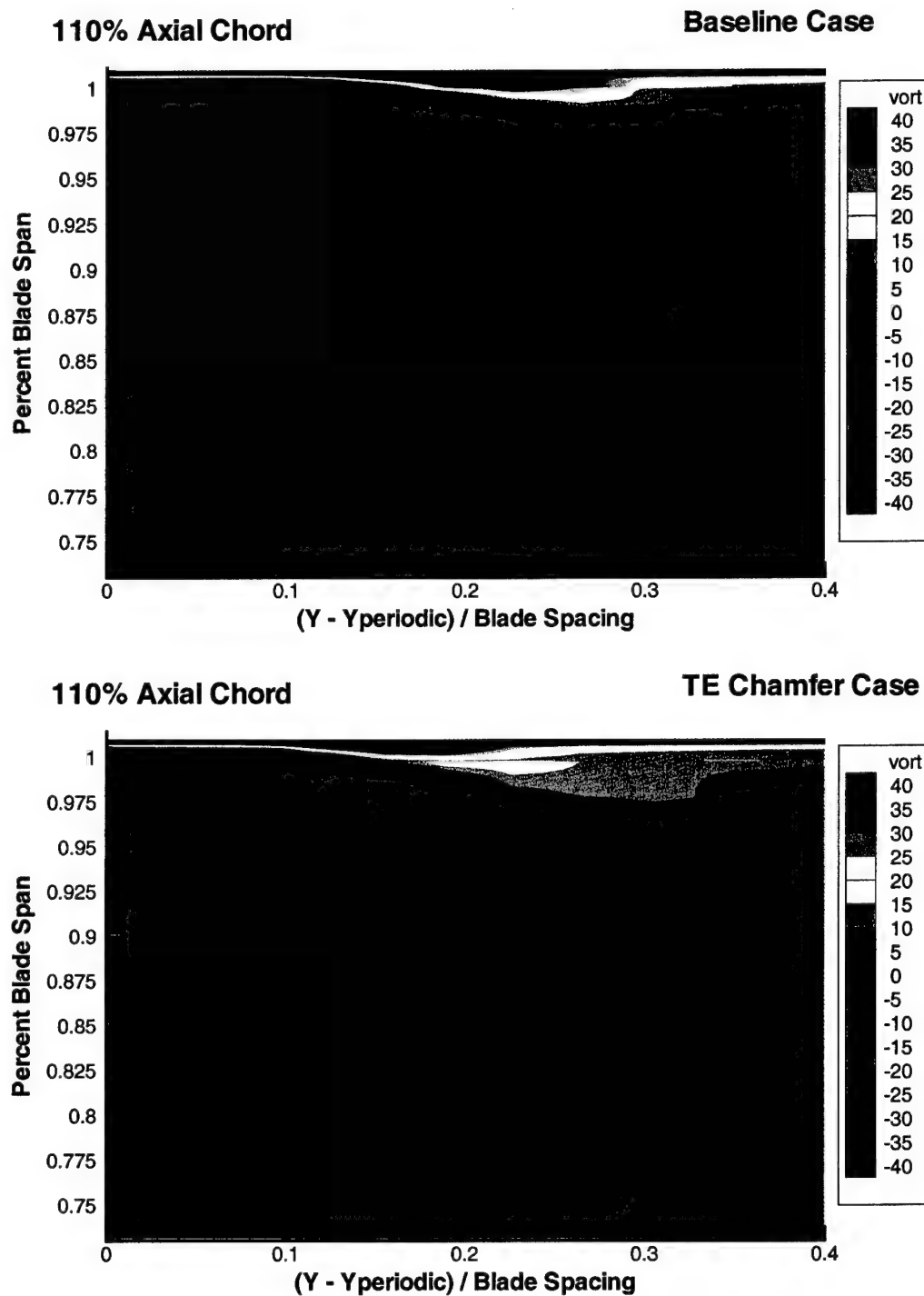


Figure 3.10: Non-Dimensional Streamwise Vorticity Contours at 110% Axial Chord

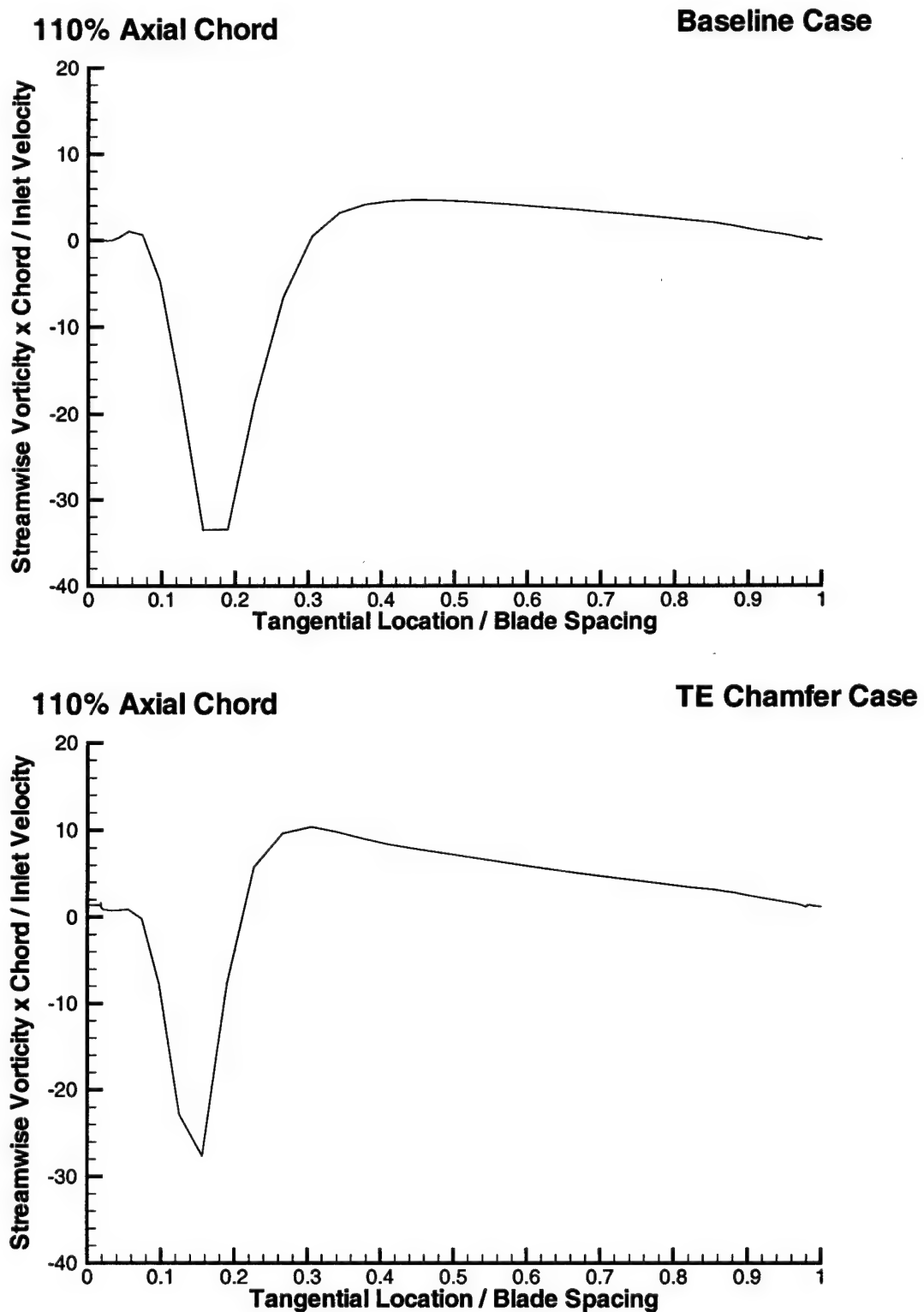


Figure 3.11: Streamwise Vorticity Inside the Leakage Vortex at 110% Axial Chord

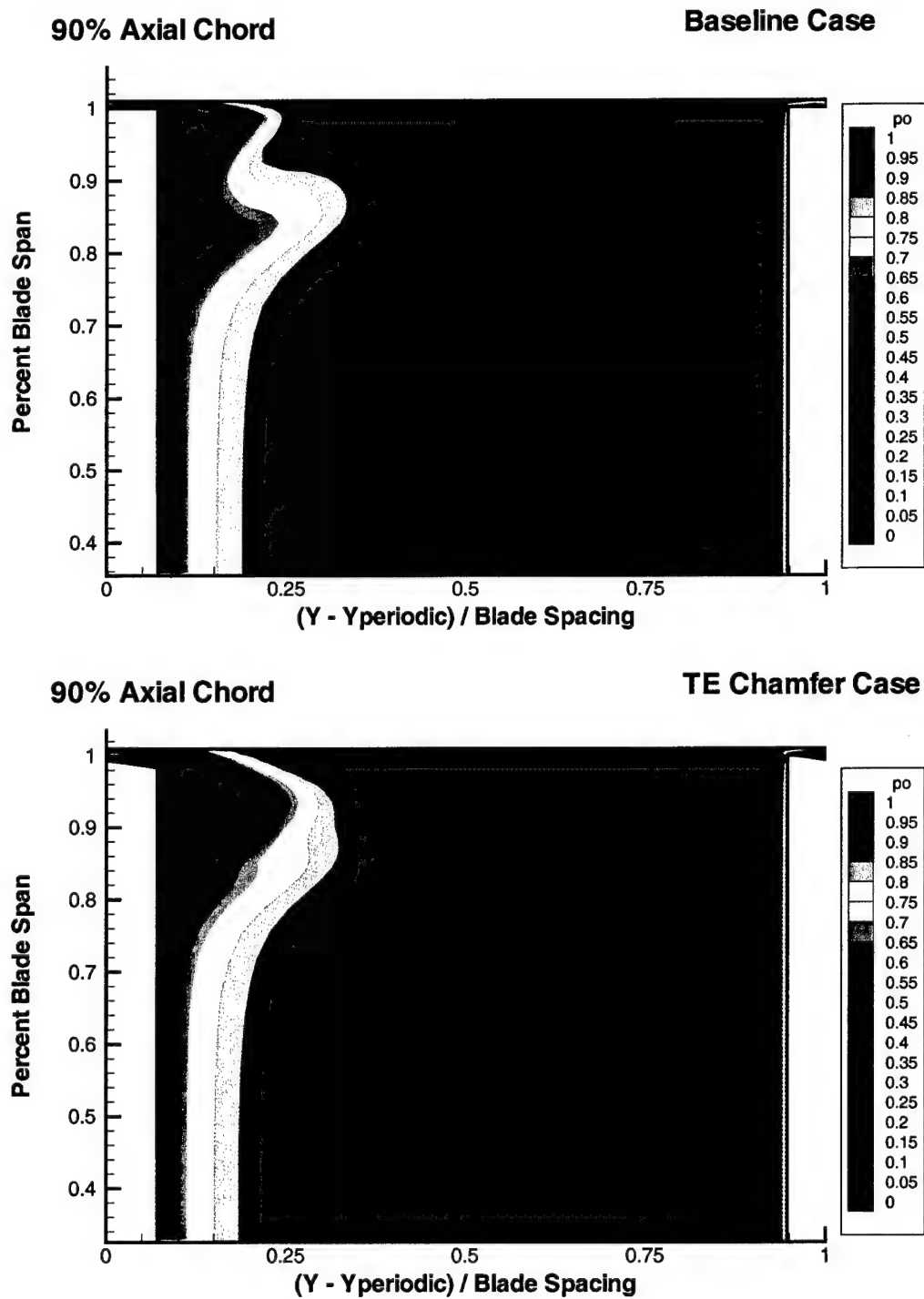


Figure 3.12: Total Pressure / Inlet Total Pressure at 90% Axial Chord

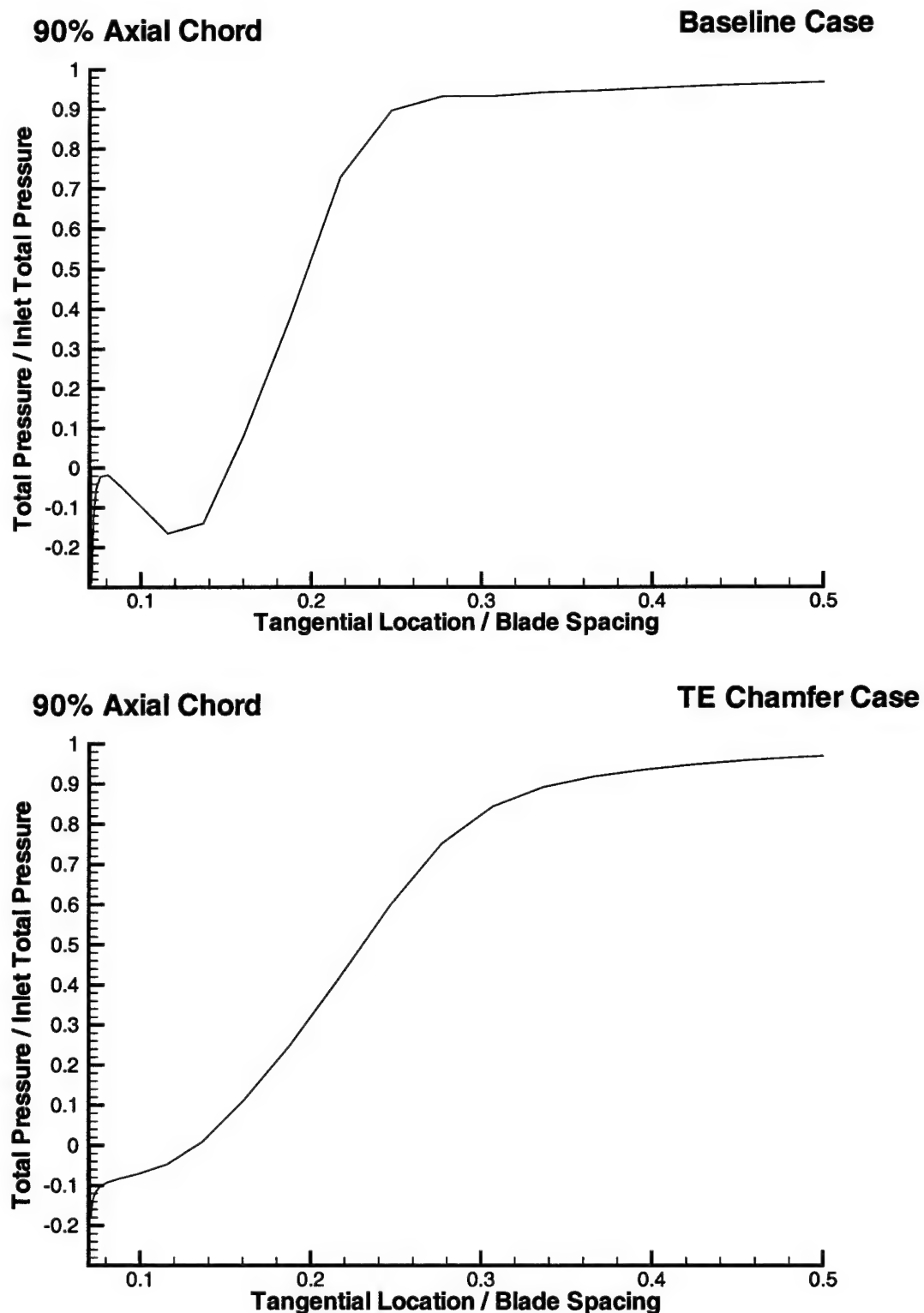


Figure 3.13: Total Pressure Inside the Leakage Vortex at 90% Axial Chord

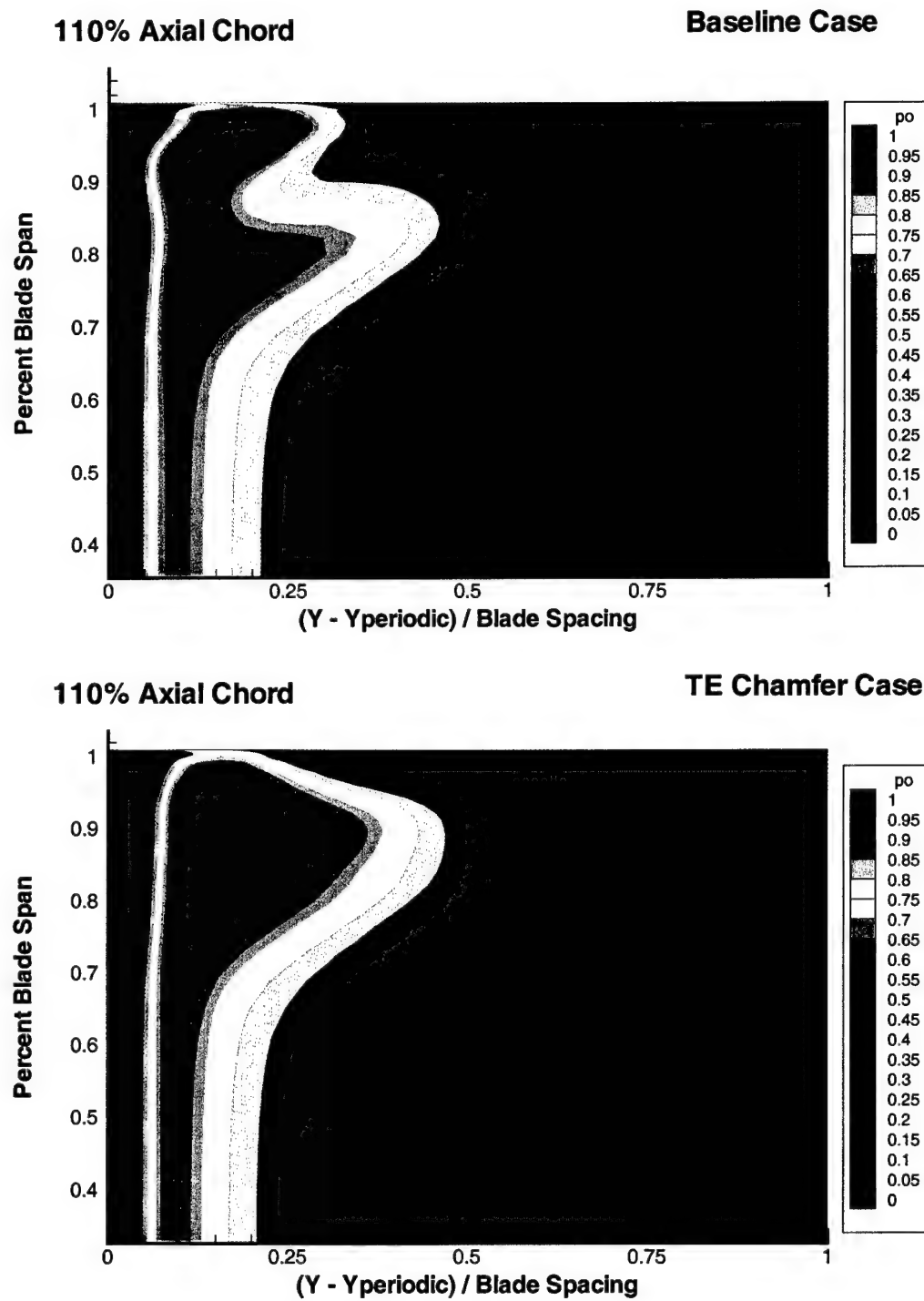


Figure 3.14: Total Pressure / Inlet Total Pressure at 110% Axial Chord

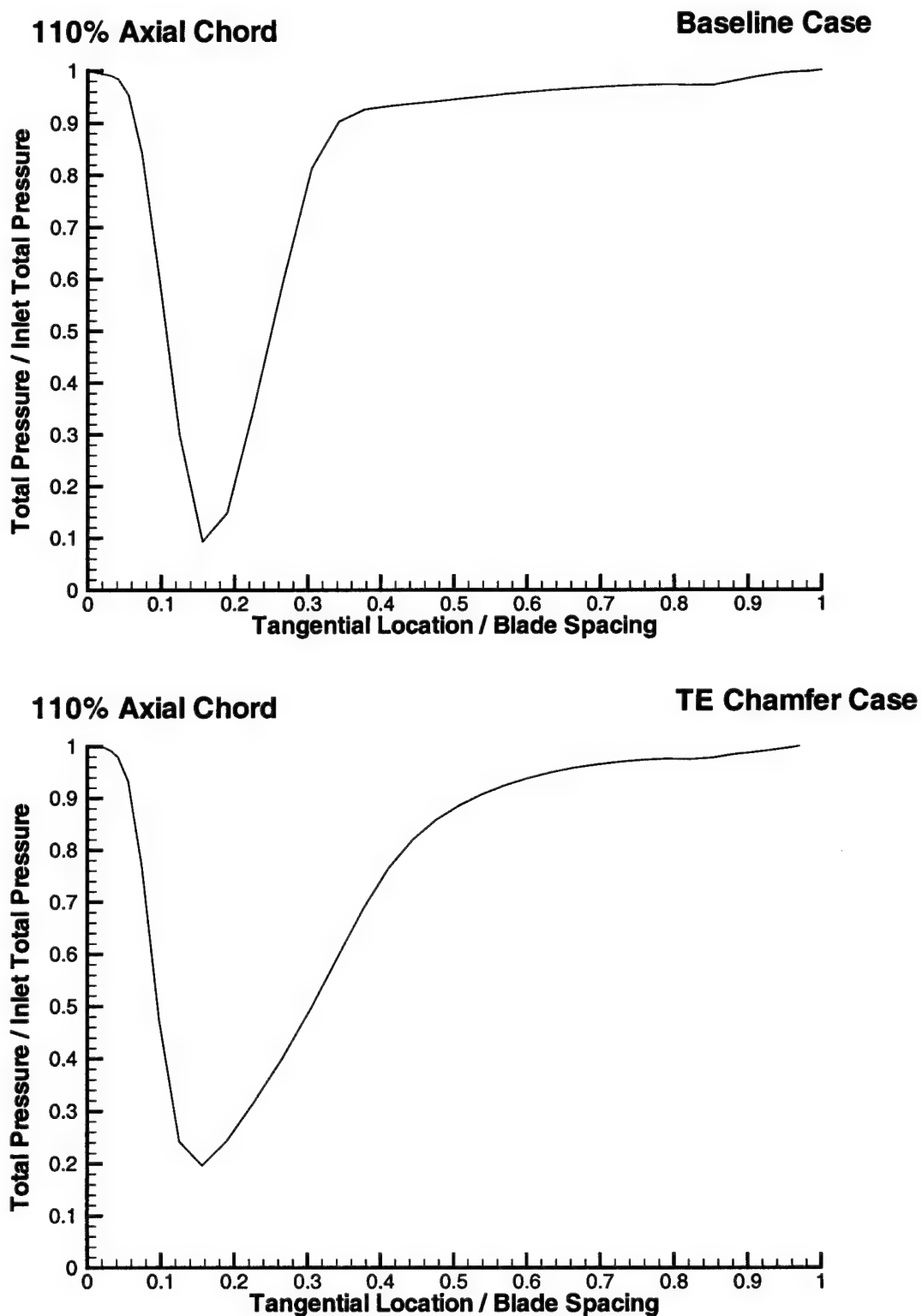


Figure 3.15: Total Pressure Inside the Leakage Vortex at 110% Axial Chord

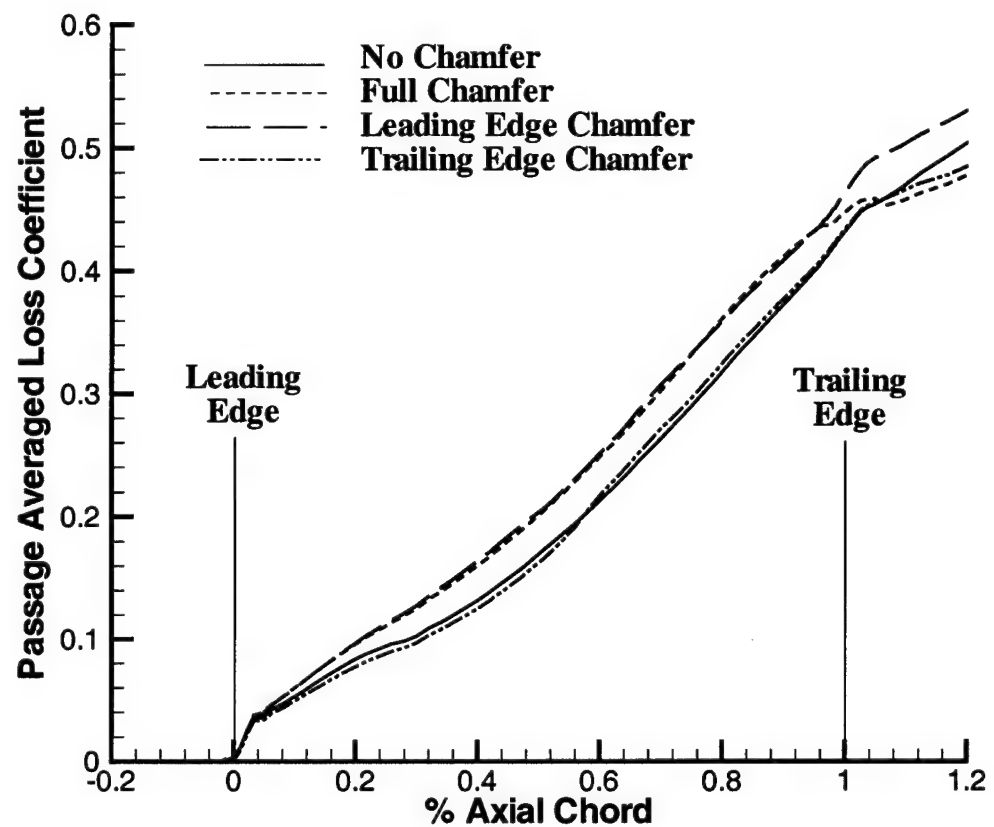
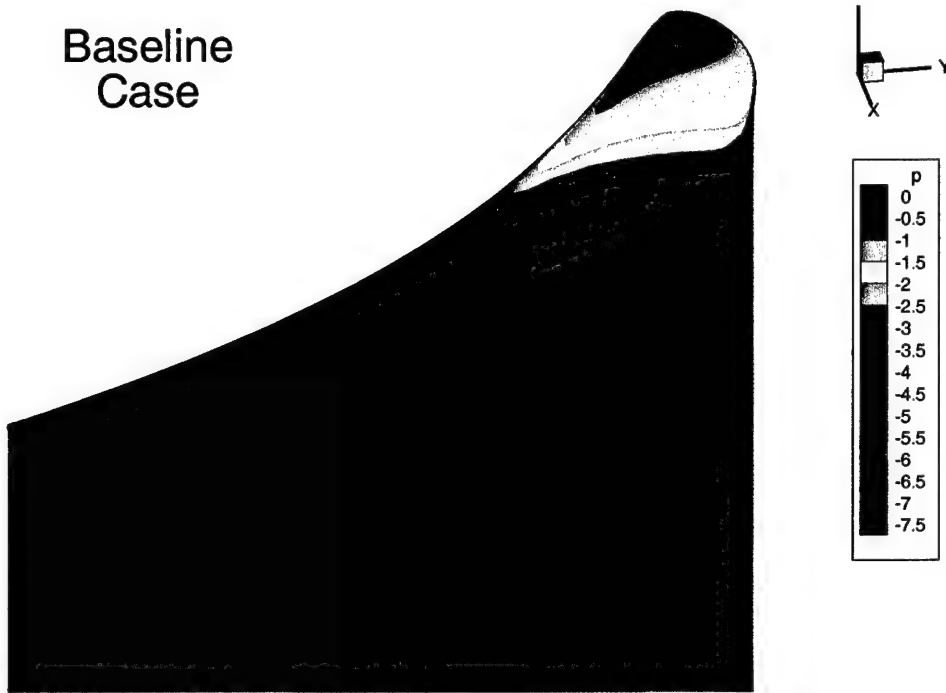


Figure 3.16: Passage-Average Loss Coefficient vs. Axial Location

Baseline Case



Trailing Edge Chamfer Case

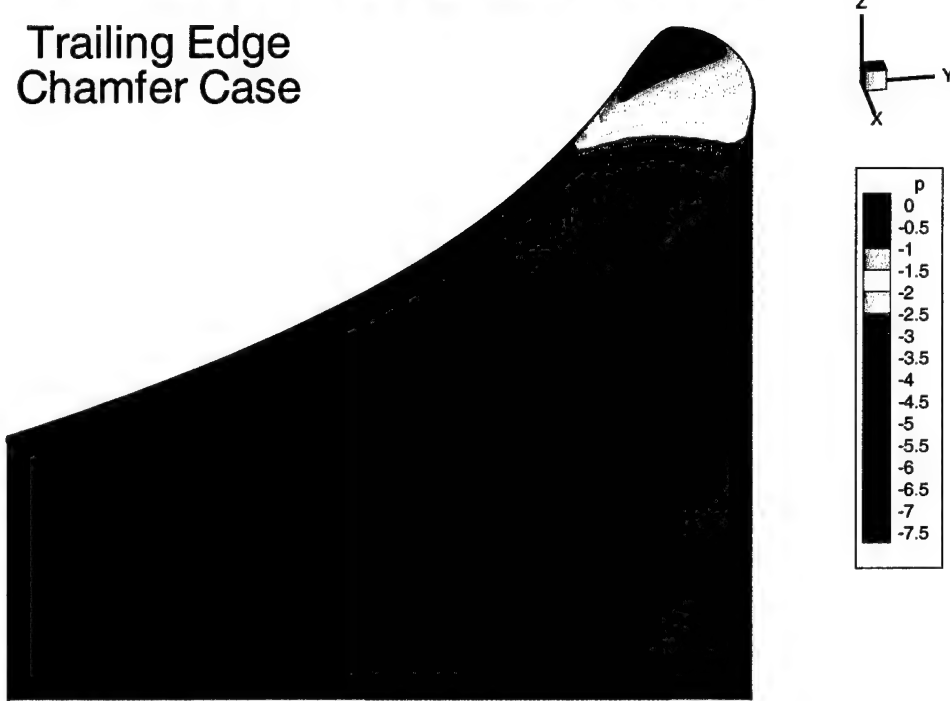


Figure 3.17: Static Pressure Coefficient (C_p) on the Blade

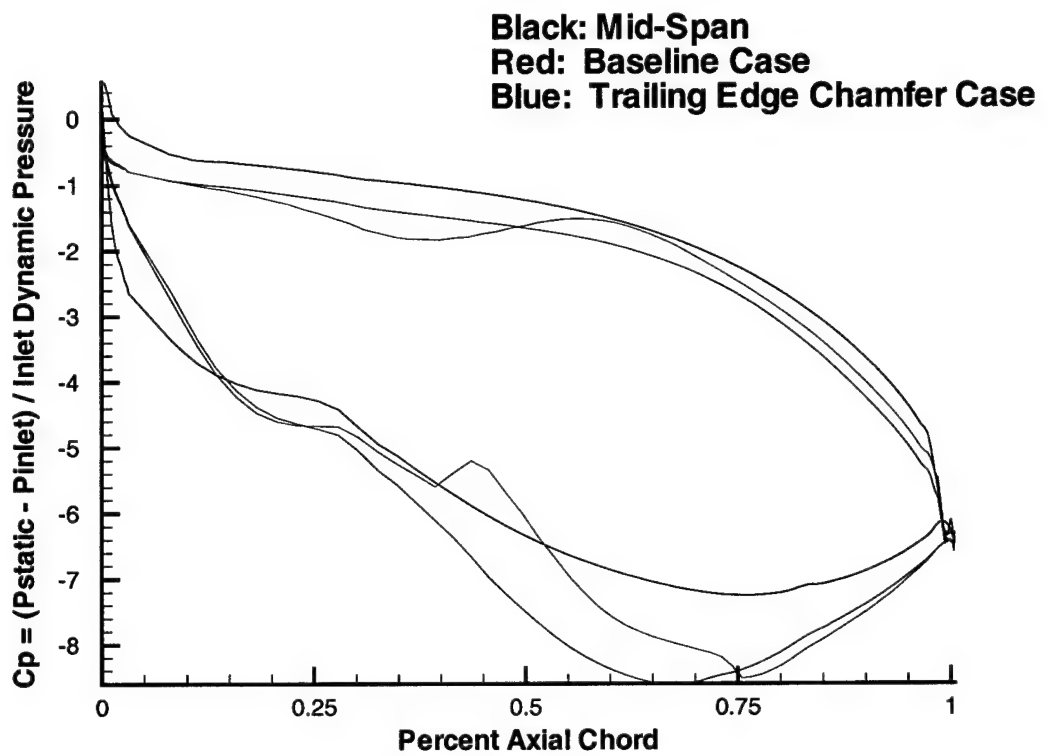


Figure 3.18: Static Pressure Coefficient (C_p) at the Blade Tip and Midspan

CHAPTER 4: SUMMARY AND CONCLUSIONS

Three different tip geometry modifications were applied to an axial flow turbine case. These modified blade tips were designed based on current understanding of the flow physics in axial flow turbines, with the intention of reducing the leakage flow and vortex. The three designs involved adding a chamfer to the leading edge region of the tip, the trailing edge region of the tip, and the entire tip region. The angle of the chamfer was 7.7 degrees from horizontal, and the gap height was kept uniform along the pressure side of the gap (1.0% blade span).

Along with a baseline, flat tipped case, the flow fields for the three modified blade tip designs were simulated using a pressure-correction type, 3D Navier-Stokes CFD solver with k-e turbulence modeling. The solution flow fields were then analyzed in detail.

Chamfering the leading edge of the blade tip led to a larger leakage vortex and increased losses. Chamfering the entire length of the blade tip also led to a larger leakage vortex, but showed potential for turning the leakage flow more toward the camber direction. Chamfering only the trailing edge region of the blade tip caused the leakage flow very near to the blade tip to turn toward the camber direction significantly. The turning of the leakage flow was found to be primarily due to the obstruction of the near-casing secondary flow inside the gap near the suction surface. The turned leakage flow was found to exit the gap at an angle less normal to the direction of the leakage vortex's rotation. The vorticity of the leakage flow near the blade tip was, therefore, less aligned with the rotation of the leakage vortex. The resulting leakage vortex for the trailing edge chamfer case was reduced in size and of different shape than the leakage vortex in the

baseline case. The smaller leakage vortex in the trailing edge chamfer case showed reduced losses downstream of the passage. The reduced size of the vortex would also lead to reduced unsteadiness and three-dimensionality downstream and, thus, improved performance in subsequent blade rows.

Chamfering the trailing edge of the blade tip has been shown to reduce the size of the leakage vortex in axial flow turbines. Future blade designs should take advantage of the leakage flow turning that is present in these cases. Future studies in this area should investigate the performance of trailing edge chamfered blade tips experimentally to verify their improved performance. In addition, the chamfer angle of 7.7 degrees was chosen somewhat arbitrarily, and additional studies should further investigate how the choice of chamfer angle affects performance. Finally, the addition of a small fence along the suction side of the blade tip's chamfered region may allow for the turning of the leakage flow while prohibiting the vortex-causing near-tip leakage flow from exiting the gap. The latter two recommendations for future research would lend themselves well to CFD analysis.

BIBLIOGRAPHY

[1] Dietrichs, H.-J., Malzacher, F., & Broichhausen, K., 1991, "Aerodynamic Development of a HP-Turbine for Advanced Turboshaft Engines," Proceedings, X ISABE, Vol.II, 1991, pp.1269-1275.

[2] Lakshminarayana, B. and Horlock, J., 1963, "Secondary and Leakage Flow in Turbomachines," Int. Journal of Mechanical Sciences, Vol. 5, pp 287-307.

[3] Wadia, A.R. and Booth, T.C., 1972, "Rotor Tip Leakage Flow: Part 2 Design optimization through Viscous Analysis and Experiment," ASME paper 81-GT-72.

[4] Yaras, M.I. and Sjolander, S.A., 1991, "Measurement of the Effects of Winglets on Tip Leakage Losses in a Linear Turbine Cascade," ISABE Conference, AIAA paper 91-7011.

[5] Bindon, J.P. and Morphis, G., 1990, "The Development of Axial Turbine Leakage Loss for Two Profiled Tip Geometries using Linear Cascade Data," ASME paper 90-GT-152.

[6] Chen, G.T., Dawes, W.N., and Hodson, H.P., 1993, "A Numerical and Experimental Investigation of Turbine Tip Gap Flow," AIAA paper 93-2253.

[7] Mohan, K. and Guruprasad, S.A., 1994, "Effect of Axially Non-Uniformed Rotor Tip Clearance on the Performance of a High Speed Axial Flow Compressor Stage," ASME paper 94-GT-479.

[8] Staubach, J.B., Sharma, O.P., Stetson, G.M., 1996, "Reduction of Tip Clearance Losses through 3D Air Foil Designs," ASME/IGTI Conference, Singapore, China.

[9] Sjolander, S.A., 1997, "Secondary and Tip-Clearance Flows in Axial Turbines: Physics of Tip-Clearance Flows - I", von Karman Institute for Fluid Dynamics, Lecture Series 1997-01, 1997.

[10] Tallman, J. and Lakshminarayana, B., 2000, "Numerical Simulation of Tip Clearance Flows in Axial Flow Turbines, with Emphasis on Flow Physics Part 1: Effect of Tip Clearance Height," ASME paper 2000-GT-0514.

[11] Tallman, J. and Lakshminarayana, B., 2000, "Numerical Simulation of Tip Clearance Flows in Axial Flow Turbines, with Emphasis on Flow Physics Part 2: Effect of Casing Relative Motion," ASME paper 2000-GT-0516.

[12] Bindon, J.P., 1991, Private Communication.

[13] Basson, A.H., & Lakshminarayana, B., 1995, "Numerical Simulation of Tip Clearance Effects in Turbomachinery," ASME J. Turbomachinery, Vol. 109, No.4, October 1995, pp. 545-549.

[14] Basson, A.H., 1992, "Numerical Simulation of Steady Three-Dimensional Flows in Axial Flow Turbomachinery," Ph.D. Thesis, The Pennsylvania State University.

[15] Patankar, S.V., 1980, Numerical Heat Transfer and Fluid Flow, Hemisphere Publishing Corp., New York.

[16] Engebretsen, E., 1997, "Development of a Multiblock Scheme for the Computation of Incompressible Flows and the Computation of Cascade Tip Clearance Flows," MS Thesis, The Pennsylvania State University